Bloch oscillations and Wannier Stark Ladder study in Semiconductor Superlattice

Fanqi Meng

Fanqi Meng. Bloch oscillations and Wannier Stark Ladder study in Semiconductor Superlattice. Other [cond-mat.other]. Université Paris Sud - Paris XI, 2012. English. NNT : 2012PA112418 . tel-00795646

HAL Id: tel-00795646
https://theses.hal.science/tel-00795646
Submitted on 28 Feb 2013

UNIVERSITE PARIS-SUD XI
ÉCOLE DOCTORALE : STITS

INSTITUT D'ELECTRONIQUE FONDAMENTALE
(IEF)
DISCIPLINE PHYSIQUE

THÈSE DE DOCTORAT

Bloch oscillations and Wannier Stark Ladder study in Semiconductor Superlattices

soutenue le 20/12/2112

par

Fanqi MENG

Directeur de thèse :	**Juliette MANGENEY**	*Chargé de Recherches(HDR),IEF – Univ. Paris Sud*

<u>Composition du jury</u> :

Président du jury :	*François JULIEN*	*Directeur de Recherches(HDR), IEF – Univ. Paris Sud*
Rapporteurs :	*Olivier GAUTHIER-LAFAYE*	*Chargé de Recherches(HDR), LAAS- Univ. Paul Sabatier*
	Dominique COQUILLAT	*Directeur de Recherches(HDR), L2C –Univ. Montpellier 2*
Examinateurs :	*Robson FERREIRA*	*Directeur de Recherches(HDR), LPA – ENS de Paris*

Content

Acknowledgments

Foremost, I would like to express my sincere gratitude to my supervisor Juliette Mangeney for giving me the opportunity to work on this challenging project and advising me all along. Your valuable guidance, continuous support, encouragement and patient helped me during all three years. Your rigorous scientific attitude always benefits my research life.

Within the group OPTOTERA, I am grateful to Prof. Paul Crozat, who has enormous knowledge of electric devices and always ready to help. I grateful to Gacemi Djamal Eddine and Mathieu Martin, who helped me a lot when I first come to France, I wish all of you good luck. I also thank Thibault Laurent, who spent one year with us as a Postdoc. Discussing with you always interested me and enhanced my understanding to France!

I am indebted to Raffaele Colombelli, who provided no end of support to my project. From structure design, to experimental set-up, to technique work in cleanroom, and to data analysis, you are always there to help. I also would like to thank François Julien, who also served as examiner of my manuscript. Every time we have problems, Francoise always gave very valuable insight in promoting our progress. Many thanks to David Fowler and Gangyi Xu, much of my early training in this field came from David as well as Gangyi. Also thanks all the technicians in cleanroon, especially Jean-René Coudevylle and Nathalie Isac, who were always ready to help me for my complex processing procedure. I would also like to thank other members in IEF and CTU, Guy Fishman, David Bouville, Maria Tchernycheva, Eric Cassan, Sakr Salam, Lorenzo Rigutti, Philippe Boucaud…

I am also indebted to Jérôme Tignon and Sukhdeep Dhillon in LPA ENS, where I carried out the gain measurement using THz TDS. They are always welcome to our experimental requirement. And it is always a pleasure to discussing with the all the people there: Jean Maysonnave, Joshua Freeman, Simon Maero, François-Régis Jasnot.

I also want to express my thanks to Jean-Christophe Harmand in LPN, Edmund Linfield in Leeds and Kazuhiko Hirakawa in Tokyo University. They provided quality samples which ensured the success of my measurement,

Also I would like to express my gratitude to the defense committee: Olivier Gauthier-Lafaye, Dominique Coquillat, François Julien, Robson Ferreira, for reading and evaluate my manuscript.

I feel grateful for Lei Cao, Na Lei, Zhuang Zhao, Jinchuan Ju, Weiwei Lin, Weisheng Zhao, Chenxing Deng, Ning Xie, for all the happy times I shared with you here.

More importantly, I want to thank my family. My fiancé Yaling Liu always encourage and support me for the past years, I feel very lucky and happy to have met you. Thanks my parents and her parents, my grandparents, as well as my brothers and sisters. I cannot finish this thesis without all your support.

Finally I would like to thank the CSC for financing support.

Abstract

Terahertz (THz) electromagnetic field, which lies in the frequency gap between the infrared and microwave, roughly between 1 THz to 10 THz, is highly desirable for both fundamental research and application. Yet tuneable compact THz sources are still not available. On the other hand, ever since first proposed in 1970, semiconductor superlattice provides new playground for various new technique and devices of tremendous research and application interest. In this thesis, an innovative theme, relying on Bloch oscillations in a dc biased semiconductor superlattice, is explored to realize tunable compact THz source *THz Bloch oscillator*. For doped superlattice Bloch oscillator, we designed quantum cascade super-superlattice structure to realize Bloch oscillations whilst prohibit electrical domain formation. The designed structures were processed into various waveguide and grating devices for electroluminescence detection using Fourier transform infrared spectroscopy (FTIR). The Bloch gain of semi-insulating surface plasmon waveguide device was also measured using THz time domain spectroscopy. Even though the electroluminescence and gain at THz regime were observed, no direct evidence of Bloch emission was confirmed. For undoped superlattice, the THz emission from Bloch oscillations was observed by time domain spectroscopy. At last, the photocurrent corresponding to heavy hole and Wannier Stark Ladder (WSL) states transitions in undoped superlattice was studied. Under CW laser pumping, the photocurrent as function of the applied voltage showed multiple WSL peaks, which indicated laser induced and controllable negative differential conductance (NDC). With increasing pumping power, the nonlinear NDC regime and bistable states were investigated as well.

Key words: terahertz, Bloch oscillations, Wannier Stark Ladder, photocurrent, superlattice

List of symbols

Symbol	Explanation	Symbol	Explanation
a	quantum well width	σ	conductivity
b	quantum barrier width	$\hbar$	reduced Planck constant
c	light velocity in vacuum	k_B	Boltzmann constant
d	superlattice period	λ	wavelength
D	sample thickness	v_r	electron group velocity
e	charge of an electron	v_d	electron drift velocity
F	electric field	$\mathrm{v_{max}}$	electron peak velocity
$\mathrm{F_c}$	critical electric field	ω_{BO}	Bloch oscillation frequency
H	electron Hamiltonian	ω	angular frequency
$\vec{k}$	electron wave vector	t	time
L	superlattice thickness	τ	scattering time
ℓ	Bloch oscillation amplitude	α	absorption/loss
m^*	electron effective mass	γ	gain
n_r	refractive index	j	current density
n_d	carrier density	τ_{diel}	dielectric relaxation time
n	quantum well number	Δ	width of the energy band
T	temperature	ε	relativity permittivity
V	voltage	ε_0	vacuum permittivity
W	transition possibility	Ψ	electron wave function
f	carrier distribution function	Θ	electron wave packet
J_n	Bessel function of first kind	I_n	Bessel function for complex argument

List of abbreviation

Abbreviation	**Explanation**
THz	terahertz
NDC	negative differential conductivity
FTIR	Fourier transform infrared spectroscopy
WSL	Wannier Stark Ladder
QCL	quantum cascade laser
TDS	time domain spectroscopy
SL	superlattice
MBE	molecular beam epitaxy
TM	transverse magnetic
TE	transverse electric
LO	longitudinal optical
LA	longitudinal acoustic

1 Introduction

As one of the most underused electromagnetic field regions, terahertz (THz) radiation is loosely defined from 0.1 THz to 10 THz, bridging the electromagnetic gap between microwave and infrared portion of the electromagnetic spectrum. THz rays show specific properties: they are low energetic, non-ionizing, very poorly absorbed by the atmosphere for some wavelengths and a lot for others. Until now, THz radiation was relatively little studied, and their "general public" applications are practically nonexistent. This fact is due to the failure of the use of traditional electronic or optical methods for the development of emitters and detectors in the THz frequency range. However, THz radiation has enormous promising applications in various fields of science and technology. To name a few, THz radiation can be applied in imaging to recognize and detect materials in industrial, medical and security, since in contrast to visible or infrared light, THz radiation can penetrate materials such as woods, plastics cloth, or paper products. THz radiation can also resolve chemical reactions, evaluate pollution contaminants, as well as detect gas and molecules, as the THz photon energies are resonant with rotational and vibrational modes of many molecules, especially organic molecule. Besides, THz radiation also has advantages for wideband telecommunication wireless network applications. Indeed, comparing with microwave wireless communication, the higher carrier frequency in the THz range would enable to carry more information. Considering all these interesting features for applications, powerful THz emitters, sensitive detectors as well as efficient THz instrumentation are widely desired. This context has motivated many advanced researches to push forward the state of the art of THz technology. The research works have been focused on the improvement of the operation frequency of electronic devices, on the extension to higher operation wavelength of photonic devices and on ultrafast opto-electronic devices since they show promising characteristics for THz generation and detection. At least, various investigations have been devoted to support the emergence of new concepts and new materials for THz generation and detection.

Considering electronic devices, like traditional Gunn diodes and resonant tunneling diodes, they have advantages of room temperature operation and easy operation; however the characteristic electron transit time in Gunn diodes and the tunneling time in tunneling diodes limit the fundamental oscillation frequency to several hundreds of GHz. Multiplication techniques must thus be used to extend to the operation frequency to the THz range reducing significantly the output powers of these electronic devices. With delicate material selection and structure design, Gunn diodes and resonant tunneling diodes at present can deliver 0.1 μW output power up to 1.2 THz at room temperature [1, 2].

Considering optical devices, traditional semiconductor laser based on interband transitions can't be extended to the THz range since no bulk semiconductor has band gap energy sufficiently low. One of the most powerful achievements is the quantum cascade laser, where THz generation comes from intersubband transitions in the tailored conduction band obtained by the growth of repeated stack of semiconductor multiple quantum well heterostructures. However, the main problem for quantum cascade laser is the operating temperature lying on cryogenic temperature. Until now, the maximum operating temperature is 189 K at 3.9 THz and reaches very recently 200 K [3, 4] for 3.22 THz. Moreover, the tunability of quantum cascade laser is limited[5].

Optoelectronics THz sources deliver THz pulses using essentially photoconductive antennas illuminated by femto-second optical pulses or optical rectification or difference frequency generation in nonlinear crystals. Such THz optoelectronic sources are used in advanced instrumentation as THz time domain spectroscopy system and THz imaging. The THz pulse intensity can reach up to 15 TW/cm^2 (the corresponding electric field amplitude is 108 MV/cm)[6]. Continuous THz emission is also provided using optoelectronic sources such as photomixers or uni-travelling photodiodes, which ensures broadband tunability. THz output power up to 24 μW was obtained at 1 THz using integrated resonant antenna[7]. THz optotelectronic sources have the main advantage to operate at room temperature.

In this context, to support the dissemination of modern THz systems, a current challenge is to develop compact, tunable and powerful THz sources operating at room temperature. Semiconductor superlattices under dc applied electric field attract considerable interest since the Bloch oscillations of electrons in such materials can provide dispersive gain and emission of THz radiation. The THz frequency of the emission is easily tunable by changing the dc applied electric field. Moreover, previous theoretical and experimental works have demonstrated the existence of Bloch oscillations and of a dispersive Bloch gain at room temperature in semiconductor superlattices.

This thesis aims to study the potential of dc biased semiconductor superlattices for THz emission relying on Bloch oscillations of electrons. During my thesis, I have made use of advanced design, processing and experiments to investigate Bloch oscillations of electrons and the associated Bloch dispersive gain in semiconductor superlattices.

Historically, F. Bloch [8] proposed the so-called Bloch waves to describe the electron wavefuntions in the periodic structure of semiconductors in 1928. Later in 1934, based on the Bloch theorem, C. Zener [9] predicted that an electron in a semiconductor under static electric field perform periodic oscillations and emit electromagnetic waves. The electron oscillation period is inversely proportional to the dc applied electric field and to the periodicity of the lattice in the field direction. Based on this prediction, tunable oscillators relying on Bloch oscillations should be achievable. While so far, Bloch oscillations could not be observed in bulk crystals, because the coherent electron motion is destroyed by scattering and tunneling processes before the electron can fulfill a complete Bloch cycle. For instance, the moderate electric field of 40kV/cm applied on bulk GaAs at room temperature gives the Bloch oscillation time period of 1.85ps, which is far more than the scattering time of 0.24ps[10].

The breakthrough came when Esaki and Tsu proposed semiconductor artificial periodic structures, *superlattices*, where two semiconductors with different band gap energy are periodically arranged in the growth direction. By the alternative growth of the semiconductor layers with small and large bandgap, a “lattice” with much larger period and therefore much smaller miniband can be designed. Thus, the electric field needed for electrons to perform one cycle of oscillations in the miniband is greatly reduced. More precisely, with a period of 10 nm, the applied electric field requires to produce Bloch oscillations at 2.5 THz is 10 kV/cm, an easily achievable value. The development of THz emitters based on Bloch oscillations becomes possible.

In 1960, Wannier [11] theoretically proved that the eigenstates of an electron in a periodic potential with an applied static electric field can be described by equally spaced discrete energy levels, which were latterly named Wannier Stark Ladders (WSL). The existence of the WSL was then verified by Mendez *et al.* [12] in 1988 by means of photoluminescence and photocurrent spectroscopy. Indeed, WSL states are actually the quantum counterpart in energy domain of Bloch oscillations in the time domain. The concept of WSL states provides a clear picture to understand and design Bloch oscillations based on band energy engineering.

According to the way the electrons are injected in the superlattice, two different devices are developed: 1/ devices based on undoped semiconductor superlattices photoexcited by femtosecond optical pulses to create electron-hole pairs in the superlattice; 2/devices based on doped semiconductor superlattices, where electrons are provided by doping impurity. Despite both of these devices rely on Bloch oscillations, the quantum mechanics that describing the origin of these effects are different since electrons in doped semiconductor superlattices have no phase relation (only the transport is coherent) while the electrons generated by femto-second optical pulses are coherent with a fixed phase relation. The detailed description of this can be found in the chapter 1.

For doped superlattice devices, research on dispersive gain associated to Bloch oscillations has long been carried out since Esaki and Tsu's groundbreaking paper in 1970[13]. In 1971, Ktitorov *et al.* [14] calculated the complex conductivity in doped superlattices with single scattering time using Boltzmann transport theory and they predicted that the real part of the conductivity is negative for frequency lower than the Bloch oscillation frequency, while remains positive for higher frequency. This prediction addressed at the first time the dispersive Bloch gain, through quasiclassical point of view. More recently, the quantum mechanical description of the dispersive gain was developed by Willenberg *et al.* [15]. The authors employed density matrix formalism to calculate the electron intersubband transition between adjacent Wannier Stark Ladder states, and obtained the dispersive gain by including inelastic scattering into the transition process; the scattering contributes to the momentum change in the electron transition and induces a local population inversion. Moreover, Tarakanov *et al.* [16] calculated this second order transition by involving acoustic phonon scattering.

Despite theoretical prediction, to date, electromagnetic emission or amplification has never been obtained in doped semiconductor superlattice devices exploiting dispersive Bloch gain. The main obstacle is that electron Bloch oscillations are associated to dc negative differential conductivity in usual doped superlattice devices, which leads to the formation of high field electric domains. Such high-field domains induce nonuniform electric field distribution in the superlattice leading to instabilities, which prevents the operation of doped superlattice devices relying on Bloch oscillations. Several suggestions have been proposed by Romanov [17] and Kroemer [18], Ryndik [19], and Allen's group [20] to realize operational conditions. These approaches, which have not yet lead to the observation of Bloch gain, are nevertheless stepping stones towards the realization of Bloch oscillator based on doped semiconductor superlattice.

For undoped superlattice devices, femto-second optical pulses are used to create coherent electron wave packets, which can perform several cycles of oscillations within their dephasing time. Compared to doped superlattice devices, the ensemble electrons are created with a coherent phase relation. Holes are also created simultaneously with electrons, and the electron-hole Coulomb interactions induce excitonic modifications of the Bloch oscillation characteristics. The Bloch oscillations in optically excited undoped superlattices originate from the quantum beats of adjacent Wannier Stark states excited via the same ground state[21]. Roskos et al.[22] first measured the THz emission from wave packet oscillations of two subbands in double quantum wells, using THz time domain spectroscopy. Shortly after, Waschke et al. [23] succeeded in measuring the THz emission from the Bloch oscillations in semiconductor superlattice using the same detection technique; this works directly verified for the first time the existence of emission due to Bloch oscillations. Moreover, Lyssenko et al.[24] have measured the absolute spatial displacement of Bloch oscillating electrons using four-wave-mixing technique. The change of Bloch oscillations to breath mode, where Bloch oscillations amplitude is zero, obtained through manipulating the exciting wave packet, has also been successively achieved by Sudzius et al.[25] and Fenciulli et al.[26]. Shimada et al.[27] Sekine et al[28] have demonstrated that the Bloch oscillations Bloch gain by indirect calculating the small signal conductance of the time domain signal.

In summary, the THz emission due to Bloch oscillations in undoped superlattice devices excited by the femto-second optical pulses has been demonstrated, while the THz emission relying on the dispersive Bloch gain in doped superlattice devices has not yet been observed. Moreover, no experimental study was devoted to the optical excitation of undoped superlattice devices using two monochromatic lasers. These guidelines are that this thesis initially launched. During my thesis, I investigate the Bloch oscillations in doped and undoped GaAs/AlGaAs superlattices with both the aim to improve physical knowledge related to Bloch oscillations but also to develop powerful THz sources and amplifiers.

- First, doped superlattice devices were designed, fabricated and characterized to provide continuous THz emission due to electron Bloch oscillations.
- Secondly, THz emission from Bloch oscillations in undoped superlattice devices excited by femto-second optical pulses was investigated through the development of a THz time domain emission spectroscopy set-up.
- Thirdly, photocurrent-voltage characteristics in undoped semiconductor superlattice

devices excited by monochromatic laser light were investigated, showing laser-induced and-controlled of a differential negative conductance based on field-dependent absorption of negative index Wannier Stark transitions. We studied also the nonlinear regime of this differential negative conductance and highlighted bistable behaviors.

2 Bloch Oscillations in semiconductor superlattice

2.1 General description of Bloch oscillation

Electron transport in semiconductor exhibits vital importance in many electronic and optoelectronic application. In general, the transport of electrons in semiconductors under an applied electric field can be described by the Drude model[29], where the electron is regarded as free-like electron and it is assumed to travel ballistically before it is scattered. However, the electron can be regarded as the free-like electron only when the electron lies in the bottom of the conduction band. Indeed, this is justified when the applied electric field is low that the ballistic acceleration within the mean free time cannot support the electron reaching the higher, non parabolic, portion of the conduction band. When the electric field becomes high enough that the electron can be accelerated to the higher part of the conduction band within the scattering time, then new phenomena appears.

Let's assume the scattering time is long that the electron can reach the higher portion of the conduction band with the electric field under investigation. According to the Bloch's acceleration theorem, the quasi-momentum vector $\vec{k}$ of an electron in the semiconductor under an electric field F can be written as

$$\hbar \frac{dk}{dt} = eF \tag{2.1}$$

where $\hbar$ is the Planck constant divided by 2π, e is the electron charge unit. With a constant electric field, the electron vector $\vec{k}$ will thus linearly increase with time. In semiconductor, using the tight binding method as described in[30], the energy dispersion relation is given by :

$$E(k) = \frac{\Delta}{2} - \frac{\Delta}{2}\cos(kd) \tag{2.2}$$

with Δ is the width of the band (bandwidth) and d is the lattice constant of the structure. The electron vector is extended in the whole reciprocal space, while the energy values are periodic. For electron motion in the semiconductor, the electron energy gained from the electric field follows the energy dispersion relation, and the electron group velocity is expressed as:

$$v_r = \frac{1}{\hbar}\frac{\partial E}{\partial k} \qquad 2.3$$

Using energy dispersion relation equation 2.2, we get:

$$v_r = \frac{d\Delta}{2\hbar}\sin(kd) \qquad 2.4$$

As the $\vec{k}$ vector is increasing linearly with time, the electron velocity oscillates sinusoidally with time, which in turn indicates the periodic motion of electrons in the real space with time. The real space position of electrons is:

$$z = z_0 + \frac{\Delta}{2eF}\cos(\frac{edF}{\hbar}t) \qquad 2.5$$

This periodic motion of electrons under an electric field is called the Bloch oscillations, and the oscillation frequency is characterized by:

$$\omega_{BO} = \frac{edF}{\hbar} \qquad 2.6$$

which is formally termed as Bloch frequency. The Bloch frequency depends linearly on the applied electric field and the lattice constant. The Bloch oscillation amplitude is directly proportional to the bandwidth Δ, but inversely proportional to the applied electric field.

As an unique electron transport dynamic in semiconductor, Bloch oscillations are interesting not only for fundamental physical research, but also for practical applications. Indeed, Bloch oscillations can serve as electromagnetic field source, with the radiation frequency easily being tuned just by changing the applied electric field. However, no actual experimental evidence has been reported of the existence of Bloch oscillations in bulk semiconductor since the prediction of Bloch oscillations in 1934. The reason lies that, under acceptable applied electric field, the electron scattering event prevents the electron from reaching the upper part of the conduction band, and thus prevent the electron oscillation. For example in bulk GaAs, the bulk semiconductor lattice period is 0.56 nm, and if we suppose a moderate electric field of 40 kV/cm, the time that electron performs one single oscillation in the first Brillouin zone is calculated as 1.85 ps. This is far longer than the scattering time at room temperature, which is 0.24 ps [10]. The electrons are thus scattered far before they can fulfill the oscillation.

The emerging of semiconductor superlattice has nicely resolved the problem in bulk semiconductor. The superlattice is the artificial semiconductor structure formed periodically arrangement of two semiconductors with different band gap energy in the growth direction. The artificial superlattice period is about ten times larger than the bulk lattice, which makes the time that needed to fulfill one cycle oscillation ten times shorter than in the bulk material. Moreover, as the electrons have one dimensional confinement in the growth direction, the scattering times is much longer as well, and up to few picoseconds[31] has been reported. Both of these properties make the observation of Bloch oscillations possible in semiconductor superlattices. In the following section, I will introduce the electron states in semiconductor superlattices, and then the semiclassical and the quantum description of Bloch oscillations in superlattice.

2.2 Electronic states in superlattice under electric field

Superlattice is an artificial structure that is realized by the periodically growth of two semiconductor layers with different band gaps, forming one dimensional electron confinement in the growth direction. The confinement of the electron motion leads to the quantization of electron energy in the growth direction. Whereas in the direction parallel to grown layers, electrons transport as they are in bulk semiconductor. Making used of the difference of the electron transport in the growth direction and the plane layer direction, the theoretical description of the electron eigenfunction can be simplified. Similar to the bulk semiconductor, the envelope function approximation is employed for theoretical description of the electron states in semiconductor superlattice. The three dimensional electron wavefuntion can be divided into two parts as mentioned previously: the x, y direction, where the electrons move freely as Bloch wave, and the z direction, where the electron is quantized in their motion. Thus, the wavefuntion of electron is given by

$$\Psi(r_{\parallel}, z) = \frac{1}{\sqrt{V}} e^{ik_{\parallel}r_{\parallel}} u_{\parallel}(r_{\parallel}) \chi_z(z) \qquad 2.7$$

where k is the momentum wave vector, V is the normalized volume, $u_{\parallel}$ is the Bloch wave in parallel layer direction, and $\chi_z(z)$ represents the envelope function in the z direction. Since only the electron transport in the z direction will be discussed in this thesis, only the z dependent terms is interested. To obtain the eigenfunction and eigenenergy of the electron transport in z direction, the Schrodinger function must be solved. The z direction Hamiltonian for electrons in the superlattice under electric field can be written as

$$H = -\frac{\hbar^2}{2m^*(z)}\frac{\partial^2}{\partial z^2} + U(z) + eFz \qquad 2.8$$

where $U(z) = U(z+R)$ describes the periodic potential of superlattice, $m^*(z)$ is the effective mass of electron in z direction, and eFz is the energy term that is induced by the applied electric field. The eigenfunction and eigenenergy can be obtained by solving Schrodinger equation for the z direction:

$$\left\{-\frac{\hbar^2}{2m^*(z)}\frac{\partial^2}{\partial z^2} + U(z) + eFz\right\}\Phi(z) = E\Phi(z) \qquad 2.9$$

To solve this, one can make use of tight binding method of first-neighbor approximation, where the envelope function is found as the combination of various single well functions with the weight factor given by the Bessel function of first order. The eigenfunction is then expressed as:

$$\Phi_m(z) = \sum_n J_{n-m}(\frac{\ell}{d}) f_e(z - nd) \qquad 2.10$$

In which ℓ is the oscillation amplitude, and is equal to $\triangle/eF$, where $\triangle$ represents the coupling intensity between adjacent wells. Assuming that the electric field is high enough tha t$\triangle \ll eFd$, the Bessel function will become:

$$J_{n-m}(\frac{\triangle}{edF}) \approx \frac{1}{(n-m)!}(\frac{\triangle}{2edF})^{|n-m|} \qquad 2.11$$

and

$$\begin{aligned} J_{n-m} &\to 1, n = m \\ J_{n-m} &\to 0, n \neq m \end{aligned} \qquad 2.12$$

It can be seen that under high field assumption the electron wave functions are localized in single wells, forming what we call the Wannier Stark Localization. The resulting eigenenergies are discrete energy levels with equal spaced, what is well known as Wannier Stark Ladder (WSL),

$$E_n = E_0 + nedF \qquad 2.13$$

where E_o is the energy between the valance band and the conduction band in the same layer and n corresponds to the well number starting from the center. The energy between adjacent wells is equal to the Bloch energy edF. The Bloch oscillation is regarded as the oscillation of electron wave packets between adjacent WSLs. Apparently, no Bloch transition is possible under high electric field as the oscillator strength between WSLs is extremely small due to the strong localization of the electron wave function in the single quantum well. While for moderate electric field, electron wave functions expands into neighboring wells, as can be seen in Figure 2.1. The expanding wavefunction enable certain tunneling or transition possibilities between adjacent Wannier states, which in turn enables electron oscillations. Apparently the oscillate strength is reduced with the increase of the applied electric field because of the electron wavefunction localization.

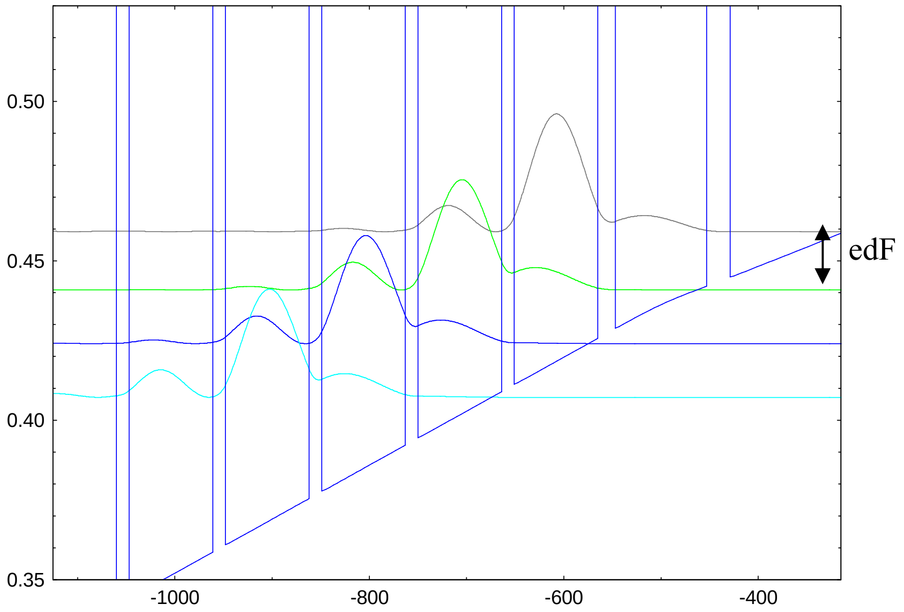

Figure 2.1: Wannier Stark Ladder in conduction band of semiconductor superlattice under bias

2.3 Quantum description Bloch oscillation in semiconductor superlattice

In Wannier Stark Ladder picture, Bloch oscillations result from the oscillation of the wave packets between WSL states. In order to well discribe the Bloch oscillations, the initial electron wave packets can be established by the linear combination of adjacent Wannier Stark states. Manipulation of the initial combination of the wave packets permits the possibility of exploration of the oscillation dynamics. Taking the eigenfunctions of WSL eigenstates given by equation 2.10 and the combination amplitude C_m, the electron wave packets are initialed as[32, 33]:

$$\Theta(z,t)=\sum_m C_m e^{-im\omega t}\sum_n J_{n-m}(\frac{\ell}{d})f_e(z-nd) \qquad 2.14$$

The weight amplitude C_m represents the m^{th} well composition of the wave packets. One can calculate the expectation value of the wave packets center of mass through

$$\left\langle \Theta \middle| z \middle| \Theta \right\rangle = d\sum_m C_m^2 m + \cos(\omega\, t)\ell \sum_m C_{m-1}C_m \qquad 2.15$$

The calculated center of mass of the wave packet consists of two terms: the first term indicates the permanent displacement relative to the center quantum well, it gives the permanent value. In case of optical selective excitation, this value indicate the permanent polarization to the ground hole state. The second term shows oscillation with time of the wave packet, where the frequency of the oscillation is the Bloch frequency and the amplitude of the oscillation is given by

$$A_z = \ell \left| \sum C_{m-1}C_m \right| \qquad 2.16$$

The oscillation of wave packet, terms as Bloch oscillation, originates from the quantum beat of the WSL states, and the oscillating amplitude is composed of the multiplication of the amplitude of neighboring Wannier Stark states, which means that only when at least two Wannier Stark states are excited, the oscillating amplitude is not zero. In particular, it is also possible that, even more than two states are excited, the oscillation amplitude A_z can be very small under the condition of $\left| \sum C_{m-1}C_m \right| \ll 1$. This is called breathing mode, and can be realized by choosing the initial composition symmetric to the center well[21, 34]. The breathing mode has been verified experimentally [24, 25].

When semiconductor superlattice is excited by femto-second optical pulse which preserves broad spectrum, at least two WSL states are excited simultaneously, thus the initial electron wave packet is established. Supposing the optical pulse is seen as transform limited Gaussian beam, the electric field of the optical pulse is written:

$$E(t) = E\, e^{-\Omega_L{}^2 t^2/2} e^{-i\varpi t} + c.c. \qquad 2.17$$

where the Ω_L is the optical pulse spectrum width and the ϖ is the optical center frequency. The optical spectrum width can be large enough to have more than two states excited and the central wavelength can be adjusted to decide the initial wave packets composition as

$$C_m \propto \frac{O_m}{\Omega_L} e^{-(E_m - \hbar\varpi)^2/2(\hbar\Omega_L)^2} \qquad 2.18$$

The exponent part describes the spectral weight of the optical pulses at the Stark Ladder position E_m, and the term O_m indicates the overlap integral between the hole wave function located at z=0 and the electron Stark states at nd.

Without considering excitonic effect, Figure 2.2 shows the calculated oscillation amplitude of the wave packets as function of the central wavelength of the optical pulses and spectrum width. In the simulation, $\frac{\ell}{d} = 4.52$ and the central wavelength of the optical pulses is represented by $\varpi_c = \varpi - E_0/\hbar$. It can be seen from the figure that if the central frequency of the optical pulses goes far from the center of the Wannier Stark Ladder, there is a maximum. When the excitation is located at the center of the Wannier Stark Ladder, there exists the minimum, which corresponds the breathing mode mentioned previously. A strong reduction of the oscillation amplitude is also observed when $\Omega_L/\omega < 0.5$, this can be explained by the fact that he spectral width of the optical pulses becomes too small to form a wave packet. The comb-like structure is caused by the fact that a smaller spectral width can still generate a wave packet if the optical pulse wavelength is adjusted in the center between two Wannier Stark Ladder states.

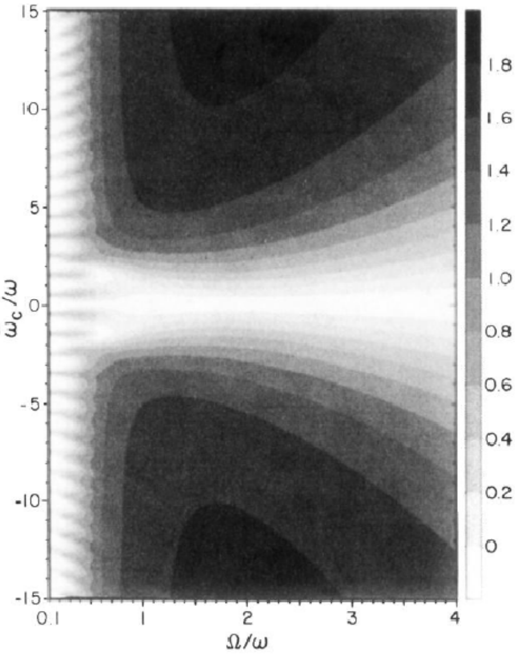

Figure 2.2: Theoretical calculation of the oscillation amplitude of the wave packet when excited by optical pulses given by Reference[32]. The amplitude is shown in gray scale.

When exciton effect is considered, as will be illustrated in section 4.1, the energy spacing between Wannier Stark Ladder states is modified. Because of the asymmetric exciton energy, the energy spacing becomes asymmetric for positive and negative WSL states, such that the breathing mode becomes less obvious. However when exciting the WSL close to its center, a minimum of the oscillation amplitude is still predicted[32].

2.4 Dispersive gain in semiconductor superlattice

2.4.1 Negative differential conductivity (NDC)

When electrons are performing Bloch oscillations, they are actually "oscillating" inside the superlattice instead of "transporting". As given by the equation 2.3 in which infinite scattering time is assumed, the ideal velocity of one electron under electric field in superlattice is sinusoidal. So these electrons contribute to the AC conductance but not DC conductance. To describe the DC conductance of superlattices under this situation, several models have been developed. Esaki and Tsu proposed a model in their breakthrough article to describe the electron transport when Bloch oscillations happen. In their model, the average drift velocity of electrons is calculated using a simplified path integration method under the assumption of a single scattering time. They regarded the average drift velocity to decay exponentially with the scattering time τ [8], and the drift velocity goes:

$$v_d = \int_0^\infty \exp(-t/\tau) dv_r \qquad 2.19$$

Using the dispersion relation given in equation 2.1, solving the equation 2.19, one obtained the drift velocity :

$$v_d(F) = v_{\max} \frac{2eFd\hbar/\tau}{(eFd)^2 + (\hbar/\tau)^2} \qquad 2.20$$

where $v_{\max}$ is constant and independent of the applied electric field. Assuming fixed scattering time, and taking zero electron wave vector and zero velocity as the initial condition, Figure 2.3 depicts the drift velocity as a function of electric field:

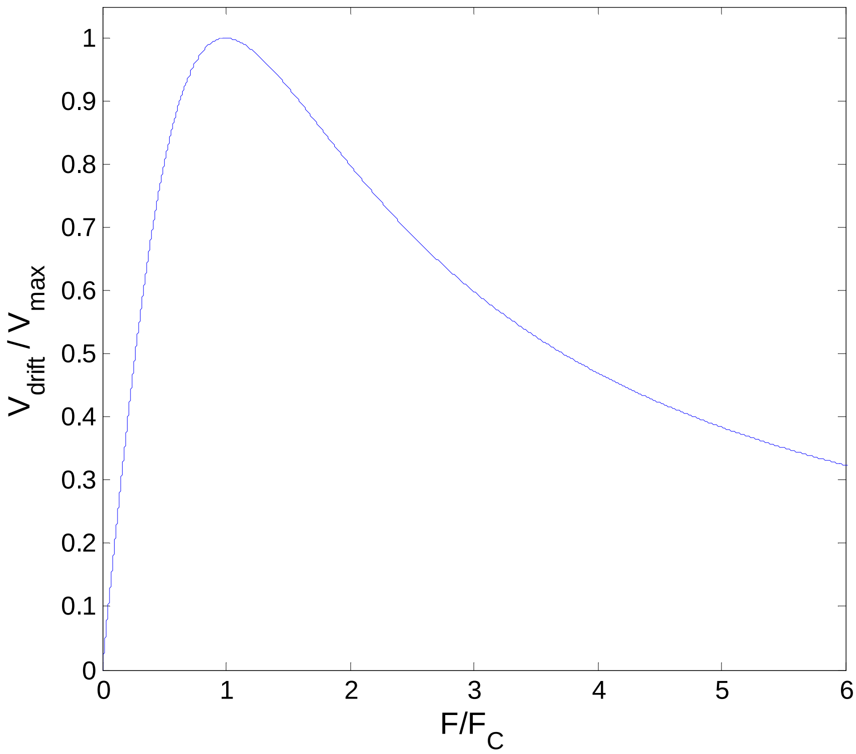

Figure 2.3: Drift velocity as a function of electric field. The electric field is normalized by the critical electric field and the drift velocity is normalized by v_{max}.

As can be seen in the figure, the drift velocity first linearly increases at low electric field, it reaches a maximum at $eF_cd = \frac{\hbar}{\tau}$, where F_c is called the critical electric field, and then the velocity decreases, showing negative differential velocity. The Esaki-Tsu model for the drift velocity of electrons can also be written in the form of critical electric field as $v_d(F) = v_{\max} \dfrac{2F/F_c}{1+(F/F_c)^2}$. As the current density is proportional to the electron velocity, the negative differential velocity also indicates negative differential conductivity. The differential conductance in superlattice is calculated as shown in Figure 2.4. With increasing the applied electric field, the differential conductance decreases and it turns to negative above the critical electric field, showing negative differential conductance (NDC).

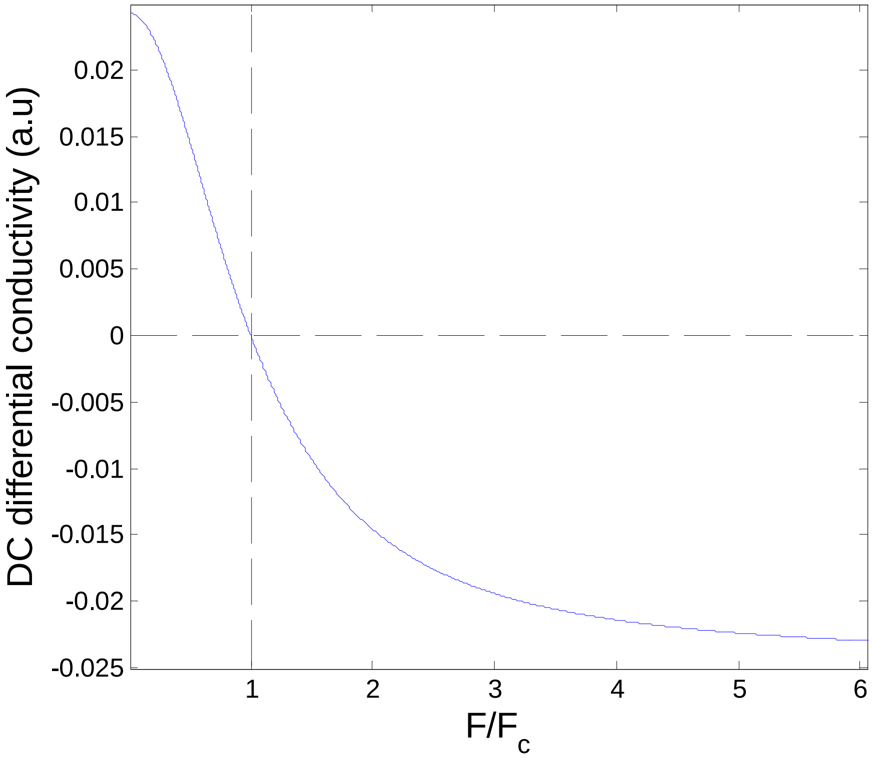

Figure 2.4: Superlattice differential conductance as a function of the applied electric field. The electric field is normalized by the critical electric field.

Further improvement of Esaki-Tsu model has been made to account for the thermally broadened distribution of electrons in k space at finite temperatures[35]. Using a simplified solution to the Boltzmann equation, the form of $v_d(F)$ remains the same, but a temperature dependent coefficient is included:

$$v_d(F) = v_{\max} \frac{I_1(\Delta/(2k_BT))}{I_0(\Delta/(2k_BT))} (\frac{\tau_e}{\tau_e+\tau_i}) \frac{F/F_c}{1+(F/F_c)^2} \qquad 2.21$$

where I_0 and I_1 are the Bessel functions for complex argument of the first and zero order. The temperature dependent coefficient is equal to 1 when $k_BT \ll \Delta/2$ and decrease asymptotically as $1/T$ when T increases.

NDC is well-known in physics, it was observed in other structures, such as Gunn diodes and resonant tunneling diodes. In GaAs Gunn diode, when the electrons in the Γ valley of conduction band gain sufficient energy from electric field, they can be scattered to the L satellite valley of conduction band, which lies higher than the Γ valley while preserving higher electron effective mass. As a result, the electrons mobility in the L satellite valley is reduced. When more and more electrons are scattered to the L satellite valley with increasing electric field, the average electron velocity decreases and then NDC appears. In the NDC region, small spike or fluctuations of electrons can be amplified, which induces space charge accumulation, which finial develops into electric field domain. Making use of the domain transport in semiconductors, Gunn diode are developed as high frequency oscillators which operate with frequency in the sub-THz and microwave range, providing a useful microwave source for applications. In case of the NDC in semiconductor superlattices, sub-THz emission resulting from the domain transport was also reported [36-38]. However, the emission frequency is limited to 150 GHz with 0.1mW output power; these performances are not comparable to the performances of traditional Gunn diode or resonant tunneling diode for practical application. Moreover, electrical domain development and transporting induce unstable nonuniform electric field distribution, which in turn prevents the operation of the Bloch oscillations, thus suppressing domain formation is a prerequisite to observe Bloch oscillations.

2.4.2 Dispersive Bloch gain

In the previous section, the DC conductivity of the superlattice is calculated with the Esaki-Tsu model, which shows negative differential conductivity at electric field higher than the critical electric field. The AC conductivity represents the electromagnetic gain and absorption characteristic. To calculate the high frequency AC conductivity, Ktitorov and co-authors[14] proposed a method by solving Boltzmann transport equation in the relaxation time approximation.

Firstly, the DC conductivity is calculated using Boltzmann transport equation. In one dimensional semiconductor superlattice, distribution function $f(k)$ describes the occupied probability at the position k. Under the static electric field F, the temporal evolution of the distribution function follows the Boltzmann equation:

$$\frac{\partial f_s}{\partial t}+\frac{eF}{\hbar}\frac{\partial f_a}{\partial k}=-\frac{f_s-f_0}{\tau} \qquad 2.22$$

$$\frac{\partial f_a}{\partial t} + \frac{eF}{\hbar}\frac{\partial f_s}{\partial k} = -\frac{f_a}{\tau} \qquad 2.23$$

In these two equations, f_s and f_a are the symmetric and antisymmetric parts of the distribution function, which are given by:

$$f_s = \frac{f(k) + f(-k)}{2},\ f_a = \frac{f(k) - f(-k)}{2} \qquad 2.24$$

f_0 represents the equilibrium distribution, and τ is the scattering relaxation time. Here the momentum and energy relaxation times are taken as the same, which are regarded as independent of k. Taking into account of the periodic boundary condition of the superlattice, as well as the dispersion relation of equation 2.2, one obtains the current density as function of the electric field:

$$j_0 = \frac{\sigma F\hbar \big/ \tau^2}{\hbar^2 \big/ \tau^2 + (edF)^2} = \sigma_0 F \qquad 2.25$$

Here, σ_0 is the DC conductivity that is obtained from Boltzmann equation, and σ in the equation is a constant. Comparing with Esaki-Tsu model, one finds they share the same negative differential conductivity and critical electric field. Both models well describe the superlattice DC conductivity.

Then to get the small signal high frequency AC conductivity, one takes the high frequency AC electric field as the perturbation. In this way, adding the frequency dependent electric field and distribution function perturbation

$$F_1(t) = F_1(\omega)e^{-i\omega t},\ f_1 = f_1(\omega)e^{-i\omega t} \qquad 2.26$$

into the equation 2.22 and 2.23, under the same periodic boundary condition, the high frequency conductivity can be calculated as[14]

$$\sigma(\omega) = \sigma_0 \frac{1 - (\frac{edF}{\hbar})^2\tau^2 - i\omega\tau}{((\frac{edF}{\hbar})^2 - \omega^2)\tau^2 + 1 - 2i\omega\tau} \qquad 2.27$$

In order to get intuitive view of the Bloch gain, only the real part of the conductivity is considered. The real part of the high frequency conductivity relative to the DC conductive as function of frequency is plotted in Figure 2.5.

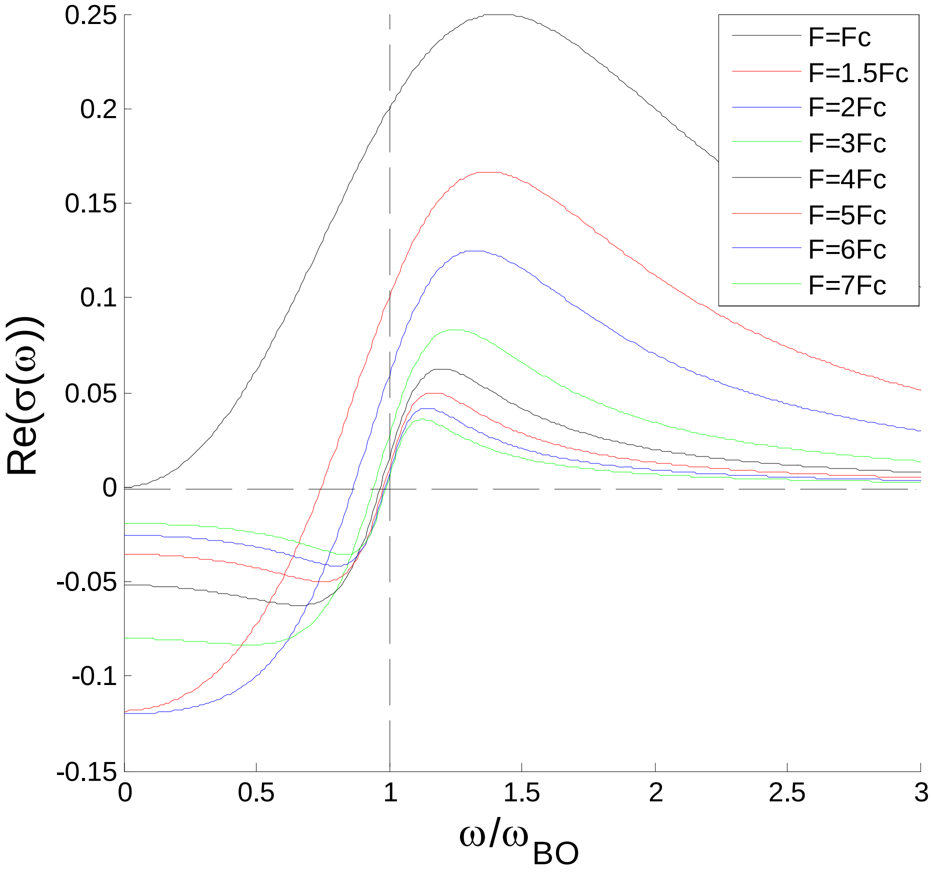

Figure 2.5: Real part of the high frequency conductivity as a function of the frequency for different applied electric field. The frequency is normalized to the Bloch frequency.

From the Figure 2.5, we can see that, when the applied electric field is higher than the critical electric field of NDC, the real part of the conductivity becomes negative at frequency below the Bloch resonance frequency. With increasing frequency from zero, the AC conductivity becomes more negative until a minimum peak is reached ; the frequency of this minimum peak is determined by the applied electric field:

$$\omega = \omega_{BO} \cdot (1 - \frac{1}{F/F_c}) \qquad 2.28$$

This frequency of the minimum peak moves towards the Bloch oscillation frequency as the applied electric increases. The peak value decreases with the increase of the applied electric field because of the reducing of DC conductivity with increasing applied electric field. The crossover between negative conductivity to positive conductivity occurs at the frequency given by :

$$\omega = \omega_{BO} \cdot (1 - \frac{1}{(F/F_c)^2}) \qquad 2.29$$

With large applied electric field, this crossover lies just below the Bloch frequency. For frequency higher than the Bloch frequency, the conductivity preserves positive. The positive conductivity goes to a maximum peak and then decrease. The positive conductivity peaks move towards the Bloch resonance with increasing applied electric field. As the gain is proportional to the real part of the differential conductivity through:

$$\alpha(\omega) = \frac{\mathrm{Re}(\sigma(\omega))}{nc} \qquad 2.30$$

where n is the refractive index of the semiconductor, the negative conductivity indicates gain and the positive conductivity indicates loss. Thus it is important to note that there exists dispersive gain profile in semiconductor superlattice, where there is gain for photon energy smaller than Bloch energy but absorption for higher photon energy.

2.5 Second order transition gain--Bloch gain

In the previous part, the Bloch dispersive gain has been obtained through the semi-classical Boltzmann equation. In this part, the dispersive gain will be described by the quantum electron transition from intersubband, taking the method used in Reference[16].

In semiconductor superlattice under an applied electric field along the growth direction, the conduction band electron states evolve from miniband to WSL scheme, forming equal spaced energy levels, and because of the translational symmetric of the WSL, the WSL preserve the same electron population. While in the plane layer perpendicular with the growth direction, the electron is still free to move, where their dispersion relation is two dimensional parabolic like, as indicated in Figure 2.6, and the electron occupation states share the same thermal distribution. Consequently for electron transition with the same momentum, the initial states and final states preserve the same population, and thus neither gain nor loss exist, only spontaneous emission can occur. Whereas, if the scattering event is included in the electron transition, the electron's initial and final states will not have the same momentum, which indicate different electron population, thus gain or absorption exists for such second order transition.

Let's consider two adjacent quantum wells. We assume parabolic dispersion relation parallel to the layer direction with effective mass approximation:

$$E_{nk} = E_n + \frac{\hbar^2 k^2}{2m^*} \qquad 2.31$$

where E_n denotes the lower subband edge. In stationary states, according to carrier thermal distribution, the carrier density is reduced exponentially as the energy increases, as indicated in the shadow area of Figure 2.6.

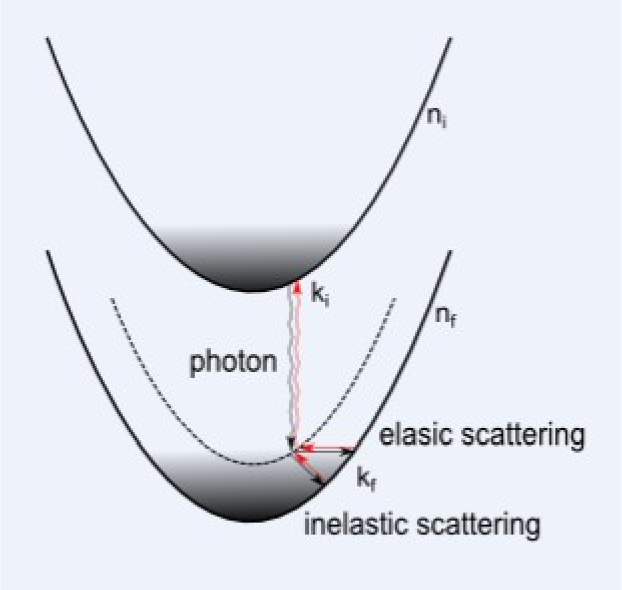

Figure 2.6: Electron transition with scattering involved

An electron transits between the intersubband n_i to n_f by emitting or absorbing one photon. For direct transition, where the momentum conservation guarantees the same k vector, namely $k_i = k_f$, the electron population of the initial state $f_{n_i}(k_i)$ equals the final state $f_{n_f}(k_f)$, there is no gain or loss for this transition. If the scattering is involved in the transition, as indicated the transition in Figure 2.6, either elastic scattering or inelastic scattering will mediate the changes of k vector. In the case of Figure 2.6, $k_i < k_f$, as a consequence the electron population of the initial state $f_{n_i}(k_i)$ is higher than the population of the final state $f_{n_f}(k_f)$, thus the population inversion is established. Following Reference [16], the treatment of the electron transition involving, for instance, one acoustic phonon is described as a second order radiative transition. Suppose H_{e-ph} and H_{e-r} are the electron phonon and electron photon interaction Hamiltonians respectively. The transition rate $W_{n_i k_i, n_f k_f}$ from the initial position $n_i k_i$ to the finial position $n_f k_f$, emitting one photon with energy $\hbar\omega$ and one acoustic phonon, is

$$W_{n_i k_i, n_f k_f} = \frac{2\pi}{\hbar}\sum_q \left| \frac{\langle n_i k_i | H_{e-r} | n_m k_m \rangle \langle n_m k_m | H_{e-ph} | n_f k_f \rangle}{E_{n_i}(k_i) - E_{n_m}(k_m) - \iota\gamma} \right| \times (N_q + \frac{1}{2} \pm \frac{1}{2})\delta[E_{n_i}(k_i) - E_{n_m}(k_m) - \hbar\omega \mp \hbar s|q|] \qquad 2.32$$

where $n_m k_m$ represent the mediate virtual state and wave factor, $\hbar s|q|$ is the acoustic phonon energy with the speed of sounds, and N_q is the number of phonons

$$N_q = \left[\exp(\frac{\hbar\omega_q}{k_B T}) - 1 \right]^{-1}$$

with the wave vector q at the temperature of T. And $\iota\gamma$ represents the energy level broadening because of varies scattering effect. Then the emission probability $R^e(\hbar\omega)$ and absorption probability $R^a(\hbar\omega)$ corresponding to the initial and final states can be written as

$$R^e(\hbar\omega) = \frac{2}{V}\sum_{n_i, k_i, n_f, k_f} W_{n_i k_i, n_f k_f} f_{n_i}(k_i)[1 - f_{n_f}(k_f)] \qquad 2.33$$

$$R^a(\hbar\omega) = \frac{2}{V}\sum_{n_i, k_i, n_f, k_f} W_{n_i k_i, n_f k_f} [1 - f_{n_i}(k_i)] f_{n_f}(k_f) \qquad 2.34$$

where V is the volume of the system. In order to evaluate the gain for the incident light, assuming the incident power is $I_0(\hbar\omega)$. The gain can be written as

$$G(\hbar\omega) = \frac{\hbar\omega[R^e(\hbar\omega) - R^a(\hbar\omega)]}{I_0(\hbar\omega)} \qquad 2.35$$

One can see that for direct transition, the initial state and finial state have the same electron population, thus the radiation possibility and absorption possibility is the same, the gain is zero. For indirect transition, the phonon changed the initial and final wave vector, which induced large radiation rate than absorption rate, hence gain exists. Tarakanov et al. [16] used deformational potential and piezoelectric coupling to calculate the electron-phonon interaction. By carrying out Monte Carlo simulations to get the electron distribution function with different wave vectors, they obtained the gain and absorption as the dashed line sketched in Figure 2.7. The figure shows gain at frequency lower than the Bloch frequency and loss for higher frequency, which indicates the same result with previously presented semi-classical description. The solid line in the figure is the measured gain and loss by Sekine et al.[28] using THz time domain spectroscopy.

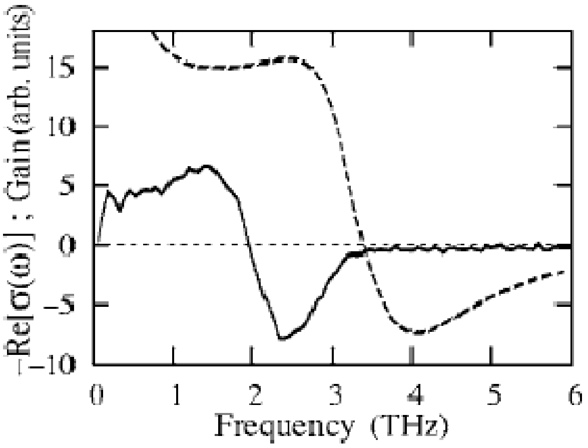

Figure 2.7: The gain and absorption calculated by Tarakanov[16](dashed line) and measured by Sekine[28] (solid curve) taken from Reference [16].

Alternatively to the acoustic phonon involved in the second-order transition, Willenberg and co-authors[15] calculated the gain by involving inelastic scattering, such as impurity scattering and interface scattering. They employed density matrix to calculate the indirect transition between two intersubbands, and the corresponding dispersive gain was also obtained. Moreover, they calculated the gain profile of quantum cascade laser, and they claimed that, in the gain profile of quantum cascade laser, Bloch type dispersive gain is included. In 2007, Terazzi and co-authors[39] verified experimentally the Bloch type dispersive gain in quantum cascade laser by gradually reducing the population inversion between the two intersubband states involved in the laser process, which motivate further research on Bloch gain[40, 41] and the work of this thesis.

3 Doped semiconductor superlattices for development of THz emitters

In the previous chapter, the general theory of the Bloch oscillations in semiconductor superlattices was presented. In this chapter, we explore the potential of doped semiconductor superlattices for the development of tunable THz amplifiers/oscillators relying on Bloch oscillations. We made use of advanced design and processing strategies to investigate dispersive Bloch gain in doped semiconductor superlattice devices. The devices were characterized by static electrical measurements, by electroluminescence measurements using Fourier Transform Infrared spectroscopy and absorption/gain measurements using THz time domain spectroscopy system.

3.1 Electrical domain suppression

In the last chapter, we discussed that electron Bloch oscillations induce negative differential conductivity (NDC) region in doped semiconductor superlattice. The most important tough problem for NDC region is the space charge instabilities that lead to electric field domains and current self-oscillations. The electric field domain formation results in non uniform electric field distribution inside the superlattice structure. The non uniform electric field destroys the high-frequency Bloch gain in superlattice. A critical challenge for the successful observation of THz Bloch gain is the suppression of electric field domains. To stabilize the electric domains, several suggestions in the design of the superlattice device have been proposed. We will briefly discuss S.J.Allen’s method and put forward our solution to this problem.

S.J.Allen’s group proposed an original scheme that consists in embedding short superlattices into heavy n-doped regions made of bulk semiconductor, forming what they called super-superlattice. The superlattice material is thus engineered as a stack of short superlattices interrupted by n-doped regions. The basic idea is based on the domain prohibition that implemented in Gunn diode. In Gunn diode that operates in the NDC region, if the thickness of the diode is thinner than certain critical length, the small space charge fluctuation will transport through the diode without amplification, and then during transporting through the heavy doped bulk semiconductor which preserve positive differential conductivity, the space charge fluctuation will be relief and electrical domain cannot be established. Let's consider the detail. The growth and collapse time of the electrical domain is determined by the dielectric relaxation time [42, 43],

$$\tau_{diel} = \frac{\varepsilon\varepsilon_0}{en_d \left| dv_d(F_0)/dF_0 \right|} \tag{3.1}$$

In the equation, the ε and ε_0 represent the relative and absolute permittivity of the well material, e is the element charge unit, and n_d is the doping density of the superlattice. The υ_d represents the electron velocity. If the electron velocity is determined by the Eski-Tsu model, as indicated in the equation 2.20, the dielectric scattering time is given by

$$\tau_{diel} = \frac{F_c}{2v_{\max}} \frac{(1+(F/F_c)^2)^2}{\left|1-(F/F_c)^2\right|} \tag{3.2}$$

The space-charge growth, given by $\exp\left(L/v_d(F)\,\tau_{diel}\right)$ where L is the length of the superlattice, is considered as large if this growth factor is greater than unity. This implies that $\tau_{diel} > L/v_d(F)$. This inequality description is frequently remarked as Kroemer's criterion for domain formation. As a result, the electrical domain cannot be established if $\tau_{diel} < L/v_d(F)$ is satisfied. Indeed, the amount of space charge that can be built up within the time of the electrons to transit across the superlattice is not enough to form strong space-charge instability. To determined the thickness of the short section of elementary superlattice and the doping density, the Kroemer's criterion can take the form of

$$n_d \times L < \frac{\varepsilon\varepsilon_0}{e} \frac{F(1+(F/F_c)^2)}{\left|1-(F/F_c)^2\right|} \tag{3.3}$$

Let's consider the widely used GaAs/AlGaAs material system. For the right part, the minimum value comes when the applied electric field satisfies: $F=2.058F_c$. If the left part keeps smaller than the minimum value of the right part, the Kroemer's equation can be satisfied for all the possible values. With this minimum value, considering the GaAs relative permittivity of 12.9, and substitute these values into the inequation 3.3, we get a range of superlattice length and doping density values as in inequation 3.4, which avoid domain formation with any applied electric field, irrespective NDC or not.

$$n_d \times L < 0.25 \times 10^8 F_c \tag{3.4}$$

In the criterion, the critical electric field takes the unit of kV/cm.

Taking the critical electrical field F_c of the value 6 kV/cm (corresponding to a typical scattering time of 690 fs in GaAs/AlGaAs material) , we have the critical condition

$$(n_d \times L)_c = 1.5 \times 10^{11} cm^{-2} \qquad 3.5$$

in which, the n_d is in cm^{-3}, and the L is in cm. Plotting this critical condition in Figure 3.1, the critical line divides the figure into 2 parts, and for the part under the line no domain could be established, whereas for the other part, domain exist. Considering the objective of developing THz emitters, higher is the doping level, higher is the electron density involved in the emission process and thus higher should be the THz output power delivered by the THz emitters. So special care must be taken for the combination of the superlattice length and the doping density. For the typical doping density of $1 \times 10^{16} cm^{-3}$, the length of the elementary superlattice should be in the scale of 100 nm.

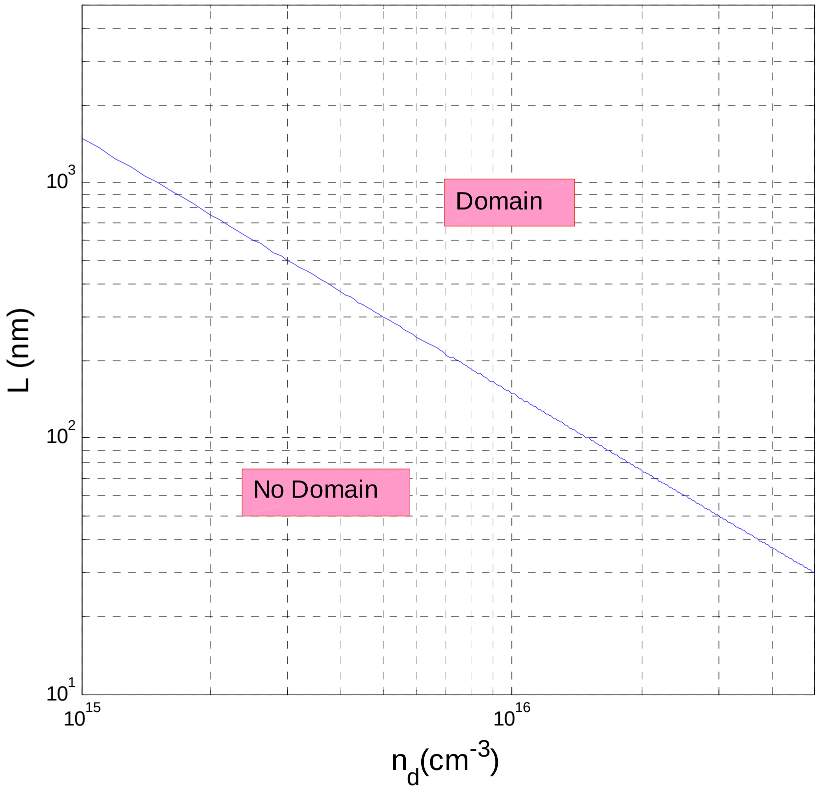

Figure 3.1:nL-diagram for the superlattice length and doping density, calculated from the Esaki–Tsu formula. Domain region represents the parameter range for which a space-charge fluctuation in the superlattice grows into a domain.

3.2 Structure design

3.2.1 Cascade super-superlattice

As doped semiconductor superlattice, we choose the benchmark system with well-established growth conditions: the GaAs/$Al_xGa_{1-x}As$ material system. Layer thickness and compositions are precisely controlled and heterointerfaces can be abrupt at the mono-atomic layer scale. The band gap of the ternary alloy $Al_xGa_{1-x}As$ is determined by the mole fraction x, following the empirical equation[44] at 0 K: $Eg(\Gamma=0)=1.519+1.25x[eV]$. The band gap of $Al_xGa_{1-x}As$ is higher than that of the GaAs, making it the barrier material. Moreover, the lattice distance of $Al_xGa_{1-x}As$ keeps nearly unchanged as the x changes, this unique properties avoid lattice mismatch between GaAs and ensuring the high quality heterointerfaces. For $x<0.4$, the $Al_xGa_{1-x}As$ is direct semiconductor.

To set the width of the quantum wells and of the barriers in the superlattice, there are two criterions: the first minband should be large enough to ensure a delocalization of the electron wavefunctions at intermediate applied electric field when the WSL exists, and the first minigap should be large to limit Zener tunneling with the second miniband. Keeping these criterions in mind, we designed two series of superlattice as summarized in Table 3.1.

Parameters	Series 1	Series 2
a	6.8 nm	8.6 nm
b	3.3 nm	1.3 nm
d=a+b	10.1 nm	9.9 nm
x_{Al}	15%	33%
ΔE_c	134 meV	295 meV

Table 3.1: Parameters of the doped semiconductor superlattice samples, where a is the well width, b the barrier width and x_{Al} the Aluminium mode fraction. The conduction band energy offset ΔE_c.[45].

The band energy and the amplitude of the electron wavefunction are calculated using a software based on self consistent solution of Schrödinger equation and Poisson equation.

Figure 3.2 and Figure 3.3 show the conduction band profiles for the two series of samples. In series 1, the mole fraction of Al is x=0.15, the superlattice first miniband is 24 meV and the first minigap is 64 meV. For series 2, the mole fraction is x=0.33, the first miniband is 29 meV and the first minigap is 59 meV.

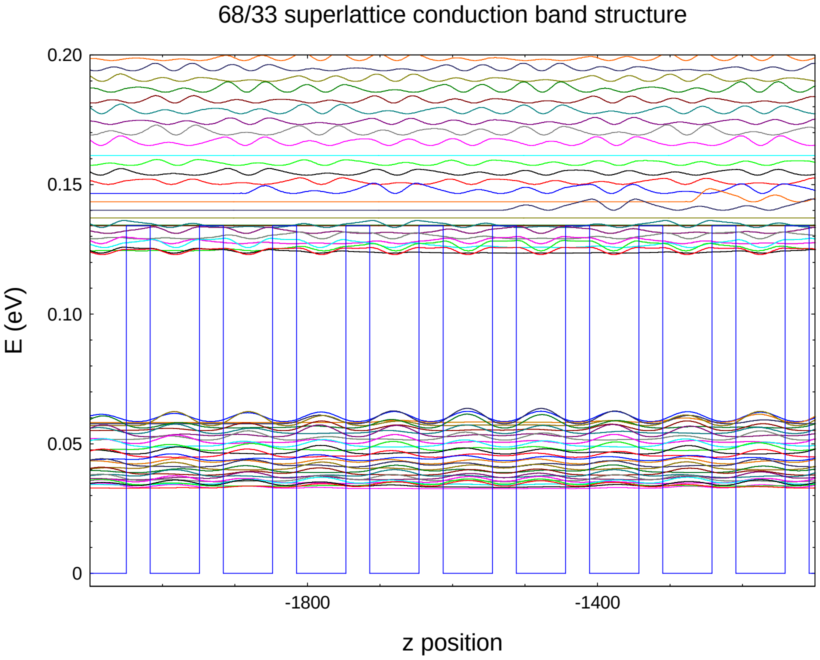

Figure 3.2: Self-consistent conduction band profiles of the superlattice region of samples from series 1. The mole fraction of Al is x=0.15, the superlattice first miniband is 24 meV and the first minigap is 64 meV.

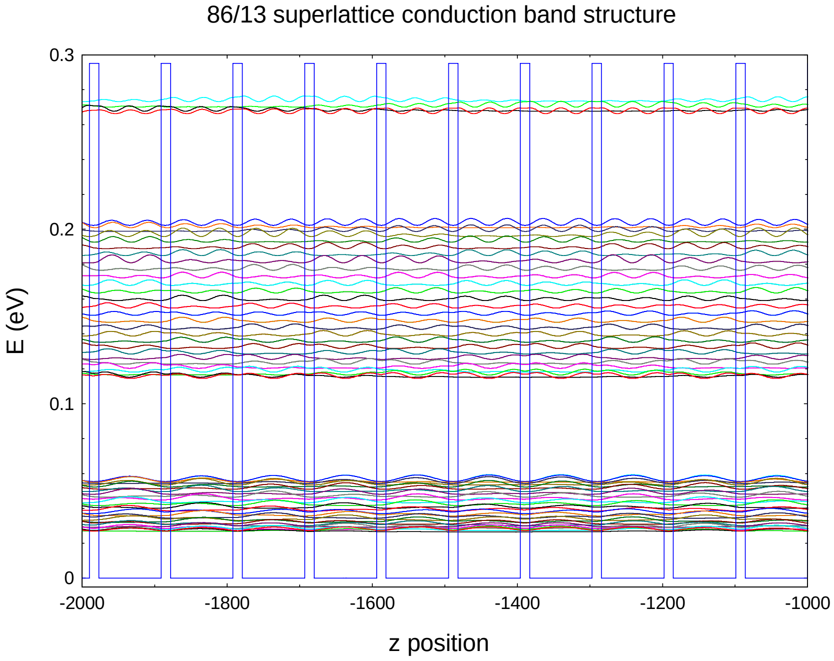

Figure 3.3: Self-consistent conduction band profiles of the superlattice region of samples from series 2. the mole fraction is x=0.33, the first miniband is 29 meV and the first minigap is 59 meV.

Noticing the superlattice period in the two series is around 10nm, the criterion for domain suppression requires the thin superlattice length of 100nm, so we would design thin superlattice module of no more than 9 periods of unit cells.

In Allen's scheme, the heavy doped bulk semiconductor was employed to facilitate the electron transport between thin superlattice modules and suppress domain. Noticing the conduction band energy levels of the bulk semiconductor are substantially lower than the energy levels of the quantum wells. The energy level mismatch induces low effective electron injection to the next neighboring superlattice module. Moreover, in super-superlattice scheme, the bulk semiconductor was heavily doped to have sufficient conductivity in order to eliminate space charge fluctuation formed in the superlattice region. In reference[20], where the author observed the first time the reduction of absorption with electric field, the total thickness of the heavy doped layers inside is about 3.4um in the whole structure, and the free electron absorption in these layers will block any observation of Bloch emission, that is why they can only observe reduction of absorption. Note that in terahertz cascade lasers (QCL), electron transport between active regions through so called injector, where electrons are fast mediated by phonon emission and/or resonant tunneling to next module. It is a good idea to borrow these injectors into super-superlattice structure, forming what we called cascade super-superlattice.

In quantum cascade laser, there are basically two different types of injectors being successfully demonstrated: chirped superlattice[46, 47] and resonant LO phonon injector[48].

The chirped superlattice injector is utilized in middle infrared and THz QCL with the active scheme of miniband transition[46] or band to continuum transition[49]. A typical structure is illustrated in Figure 3.4, which demonstrates the bound to continuum type injector in THz QCL by Scalari in 2003[49]. In this structure, the upper radiation states is marked as level 8, where the electron are injected from the upper miniband through fast resonant tunneling. The lower miniband is level 7, which located in the upper part the chirped superlattice. Within the superlattice, because of the close overlapping of the wavefunction, the electron can be fast relaxed to the bottom thanks to the fast LA phonon or other scattering process. In this way, the population inversion can be established between level 8 and 7. The chirped superlattice is efficient for transporting electrons; however the alignment of the chirped superlattice energy levels is sensitive to the applied electric field, which in turn influences the electron transport inside. This complexes the interpretation of the electron transport in the whole structure, which is not favored in our design.

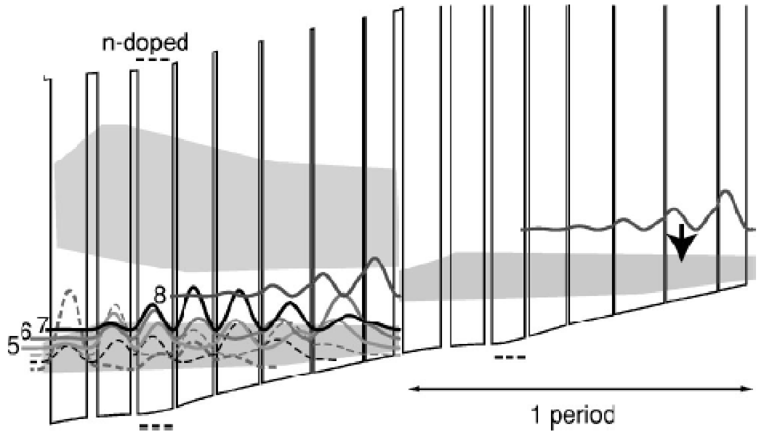

Figure 3.4: Example of the conduction band diagram of a bound to continuum THz QCL[49]

Resonant LO phonon injector was first used in the middle infrared QCL, where radiation came from diagonal or vertical transitions and the fast depopulation of the lower radiative state was realized by the efficient LO phonon emission resonant tunneling to the sublevels[50]. As the intersubband energy enters in terahertz range which is smaller than the

LO phonon energy, the problem of selective injecting electrons only to the upper radiative state while preserving sufficient oscillator strength of the radiative levels become more serious. Williams[48] improved the LO phonon injector design, and used four quantum well module. In his design, the intrawell LO phonon relaxation scheme was selected, which making the LO relaxation less sensitive to the working bias comparing with diagonal LO phonon relaxation. Seen in Figure 3.5, at working bias, the terahertz is emitted from the electron transition between level 5 and 4. The electrons in the level 4 and 3 can be fast transported through electron-electron scattering. Because of large overlap of wavefunction of 4, 3 and 2, 1, the level 4 are fast depopulated by emitting LO phonon, and the electron injection to the upper radiative state 1 or 5 are also guaranteed at the same time. As the depopulation is depending on the emission of LO phonon not on the distribution of electrons, this kind of design is thermal insensitive and can also prevent thermal back filling for higher temperature operation, which make it highly perspective in high temperature THz QCL.

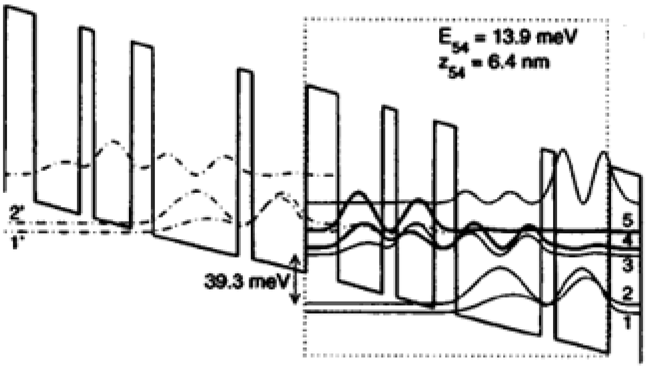

Figure 3.5: Example of the conduction band diagram of a resonant LO phonon injector QCL[48].

Making use of LO phonon injector and combining the thin superlattice mentioned above, we designed the cascade super-superlattice: the electrons will transport in the thin superlattice and perform Bloch oscillations, then they will be relaxed to the next thin superlattice module through the LO phonon injector (Figure 3.6). In the injector region, there are three or four quantum wells, in which one quantum well with wide width is responsible for the LO phonon relaxation, and the other two or three wells are designed for energy level alignment, from which the electrons are filled in.

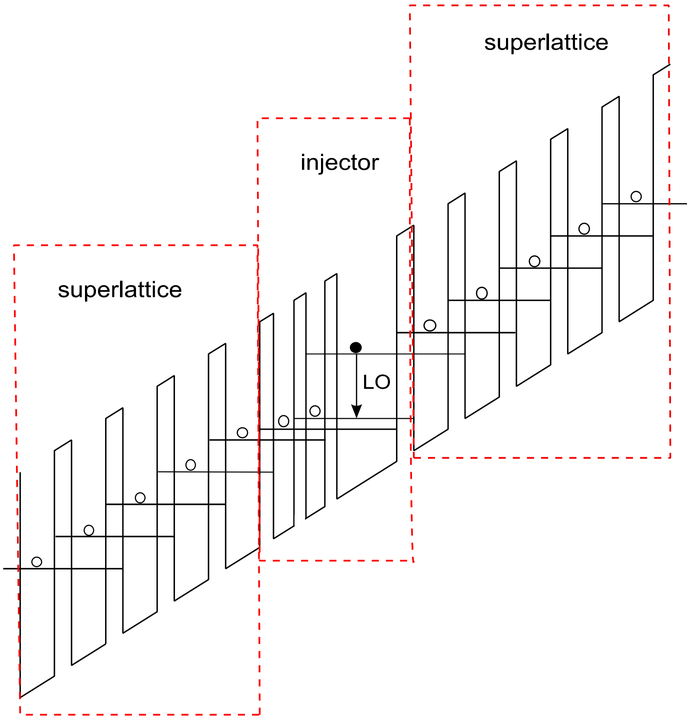

Figure 3.6: Schematic diagram of the LO phonon cascade structure.

Based on the two series of superlattice structures listed before, five samples are designed, as summarized in Table 3.2.

Table 3.2: Parameters of the doped cascade super-superlattice samples based on LO phonon injector.

	L358	**L414**	**L416**	**L527**	**L665**
Al %	15	15	15	33	33
SL unit cell number	9	9	9	9	5
Injector quantum wells number	4	4	4	3	3
Doping region in the injector	Wells Barriers	Wells Barriers	Wells Barriers	Wells Barriers	Barriers
SL doping	N	N	Y	N	N

In the sample L358, the barrier material is $Al_{0.15}Ga_{0.85}As$, there are 9 superlattice unit cells in the superlattice and 4 quantum wells in the injector. The quantum wells and barriers in the injector are Si doped with $1\times10^{16}cm^{-3}$.Thesuperlattice region is not doped. Comparing with L358, the doping density is increased to 4×10^{16}cm^{-3} for L414, and superlattice region and injector region are doped with 8×10^{15} cm^{-3} and 4×10^{16}cm^{-3} respectively for L416. The conduction band of L358 is shown in Figure 3.7, where the applied electric field is 11kV/cm.

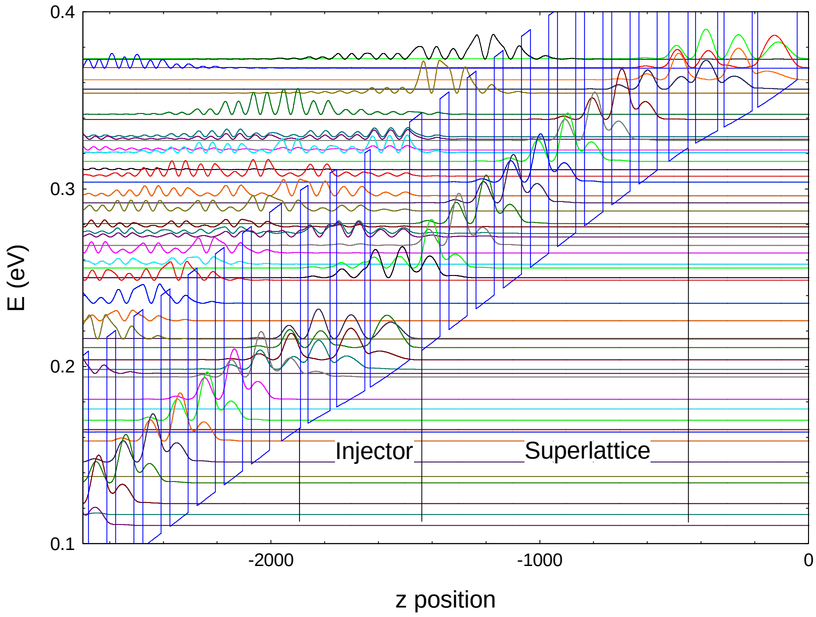

Figure 3.7: Self-consistent conduction band profiles for sample L358 under electric field of 11 kV/cm.

Sample L527 have 33% Al in the barrier to limit the thermal electron injection to the continuum band, and 3 quantum wells injector is designed to reduce terahertz re-absorption. The doping density in the injector is 1.5×10^{16}cm^{-3}, and no doping in superlattice region. For the sample L665, the superlattice period is 5, and only the barriers in the injector is doped to avoid impurity emission, the doping density is 7.5×10^{16}cm^{-3}. The doping sheet density in L527 and L665 are designed to have the same level with L358.

3.2.2 Waveguide and surface emission

To maximize our capability to observe the THz radiation emitted by these electrically biased doped superlattice devices, it is crucial to optimize the confinement of the THz radiation with the oscillating charges as well as the extraction efficiency of the THz radiation. The radiation emission resulting from the intersubband transitions between two WSLs of adjacent quantum wells is polarized in the transverse direction (TM) due to the intersubband selection rule. Namely the electric field is polarized perpendicular to the superlattice layers.

The dielectric mode confinement widely used in near-infrared and visible diode lasers to confine the radiation in the vertical (growth) direction, and obtained by the presence of cladding layers with lower index than the active layer, while it is not feasible at THz frequencies for two reasons. First, to be effective, the thickness of the cladding layers must be on the order of the wavelength of the radiation inside the semiconductor, which would be larger than 10 µm, a thickness unreasonable to grow by MBE. Second, loss due to free carrier absorption increases for frequencies above the plasma frequency, and as consequence the mode overlap with doped regions must be minimized. Furthermore, for GaAs/AlGaAs growth systems, the GaAs substrate has a higher refractive index than AlGaAs, and hence the substrate provides no natural mode confinement. In this context, the research community working on THz QCL has developed two types of waveguides for the confinement of the THz radiation: the semi-insulating-surface-plasmon waveguide and the metal-metal waveguide. These waveguides designed for TM polarized emission provide relatively high coupling factor with limited losses in the THz range. With such waveguides, the THz radiation is emitted only from the edges of the waveguides.

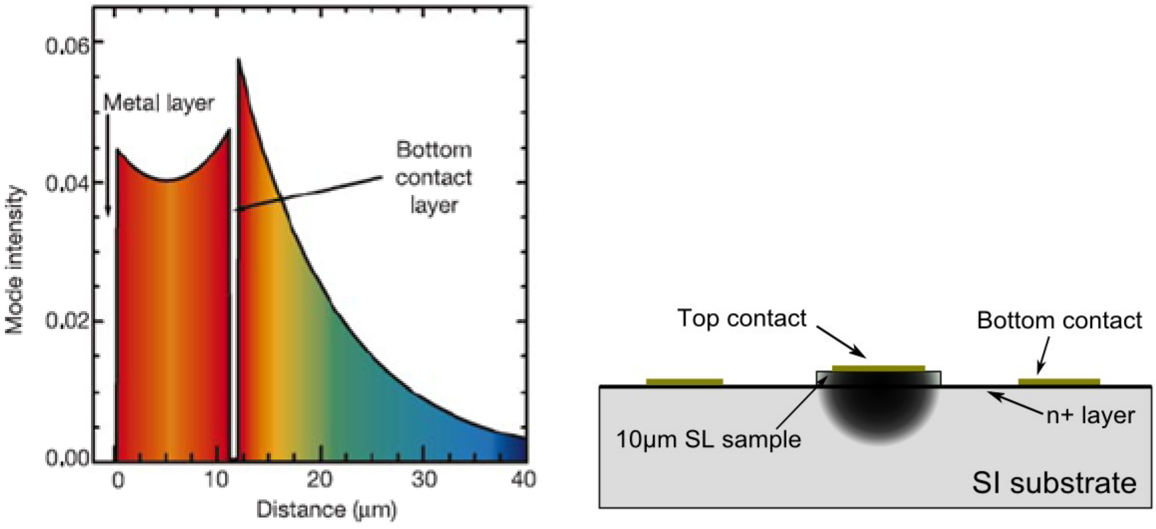

(a) (b)

Figure 3.8 Calculated semi-insulating surface plasmon waveguide mode profile (a) (taken from ref[46]) and the mode profil in the substrate for the cut-off profile (b).

The semi-insulating surface plasmon waveguide, first proposed by Ulrich*et al.*, was a key enabling component of the first terahertz QCL[46-48]. In this waveguide, the mode of the THz emission is bound to the upper metallic contact and a thin heavy doped contact layer grown directly beneath the active region and above the semi-insulating GaAs substrate. Because the doped layer is thinner than its own skin depth, the mode extends substantially into the substrate. The mode profile is shown in Figure 3.8. Since the mode overlap with the doped contact layer is small, the free carrier loss is minimized, for instance, loss is typically ~8 cm^{-1} at 3 THz with a confinement factor of ~0.3. The main advantage of this waveguide is the large fraction of the mode propagating outside the gain medium providing a high efficient coupling between the guided and the free-space radiation. The coupling efficiency of waveguide devices enables 50% of the THz photons to be coupled out[51].

The improvement of the mode confinement and the reduction of the loss of semi-insulating surface plasmon waveguides can be made by replacing the lower thin heavy doped layer with a layer of metal to form a metal-metal waveguide. The typical mode profile and the waveguide schematic are reported in Figure 3.9. Since the skin depth in gold is only several hundred Angstroms at THz frequencies, the metal-metal waveguide shows weak loss with a confinement factor close to unity. For instance, loss is typically ~15 cm^{-1} at 3 THz with a confinement factor close to 1. These advantages come at the expense of processing complexity, as a flip-chip wafer bonding technology. Moreover, the mode mismatch between the guided and the free-space radiation modes is severe. With the help of surface grating, this coupling problem can be resolved.

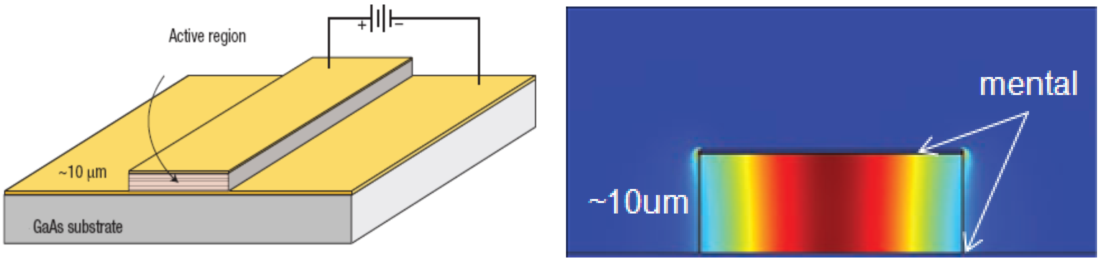

a

b

Figure 3.9: Left : Drawing of the metal-metal waveguide. Right: Electric-field profile for the fundamental propagating mode in a metal-metal waveguide.

The performances of surface plasmon waveguides are limited if the loss are much greater than the mirror loss (facets) so that photons emitted further away from the edge are absorbed, since consequently only a small fraction of emitted light escapes the waveguide. For this reason, I have fabricated some devices with a metallic grating on top of the sample, typically with period of 10-20 μm and a 50% fill factor, which we term it the subwavelength-grating surface emitting device. The purpose of the grating is to efficiently couple radiation from the large surface of a device. Coupling efficiency in grating coupled surface emitting up to 30%[52] have been reported. This approach was one of the earliest methods for measuring intersubband emission[53]. However, the edge emission configuration is preferred whenever possible, because it eliminates the possibility of any grating induced artifacts in the emission spectrum.

3.3 Device fabrication

Our designs were grown by molecular beam epitaxy (MBE) technique, which provides extremely precise thickness control of the growth layer to atomic scale. The samples were grown on semi-insulating (100) oriented GaAs wafers by S. Kumar and E. Linfield of Leeds University. The super-superlattice structures of our samples are inserted in a stack of layers including sacrificial layers and contact layers as illustrated in Figure 3.10. The 300 nm $Al_{0.5}Ga_{0.5}As$ layer is an etch stop layer for substrate removal for double-metal waveguide structures. The 600 nm and 80 nm n^{+}GaAs layers provide the bottom ohmic and top contacts respectively. The bottom n^{+}GaAs layer is thicker for the etch depth tolerance.

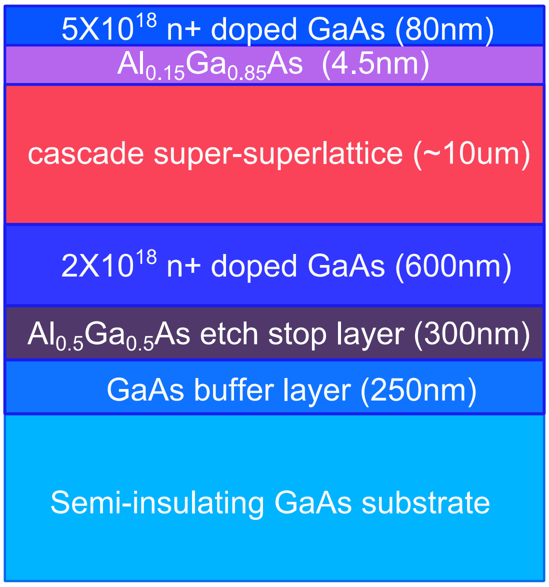

Figure 3.10: Structure of the MBE-grown doped Bloch samples, showing the thickness and the doping of the sacrificial layers, the active region and the contact layers.

I have carried out all the fabrication at University Paris-Sud in the Centrale Technologique Universitaire(CTU) Minerve collaborating with R. Colombelli and D. Fowler, with the exception of the wafer bonding stage, which was fabricated by Applied Microengineering Ltd at UK. The fabrication follows the standard contact photolithography techniques. The fabrication processes of the semi-insulating surface plasmon structures and double-metal structures are discussed in the following. Both semi-insulating surface plasmon waveguides and surface emitting grating devices are based on the same single surface plasmon structures. The process sequences are thus similar for both types of devices, except for the mesa shaped ridge or square. The detailed processing procedure and recipe can be found in the Appendix.

3.3.1 Semi-insulating surface plasmon structure

Following MBE growth, three photolithography steps are performed for the processing. The Figure 3.11 illustrates the process sequences.

- The first step is to define the mesas on the epitaxial layers in a form of a ridge or a square for semi-insulating surface plasmon waveguides and surface emitting grating devices respectively. After the wafer is cleaned, the positive photoresist S1818 is spun onto the wafer surface. The photoresist is then baked for harden. With designed mask for ridge or grating mesa, the wafer is exposited in the UV radiation, and developed in MF319 or MF351 developer. If the wafer is well developed in this step, it is going be wet etched for mesa. The typical etchant solution for AlGaAs/GaAs material system is H_2SO_4:H_2O_2:H_2O, with the ratio of 1:8:40. This type of etchant etches both AlGaAs and GaAs with equal speed, which guarantees good quality of the mesa edge. The concentration of H_2O in the etchant can also be changed to control the etching speed. The etching is carried out with several intervals. For each interval, the etching depth was regularly measured by the surface profiler (Dektak), making sure that the etching stops right in the upper middle of 600 nm n^+ doped GaAs layer. Longer or short etching time may induce over or under etching, which may cause parasitic resistance, or an open circuit.

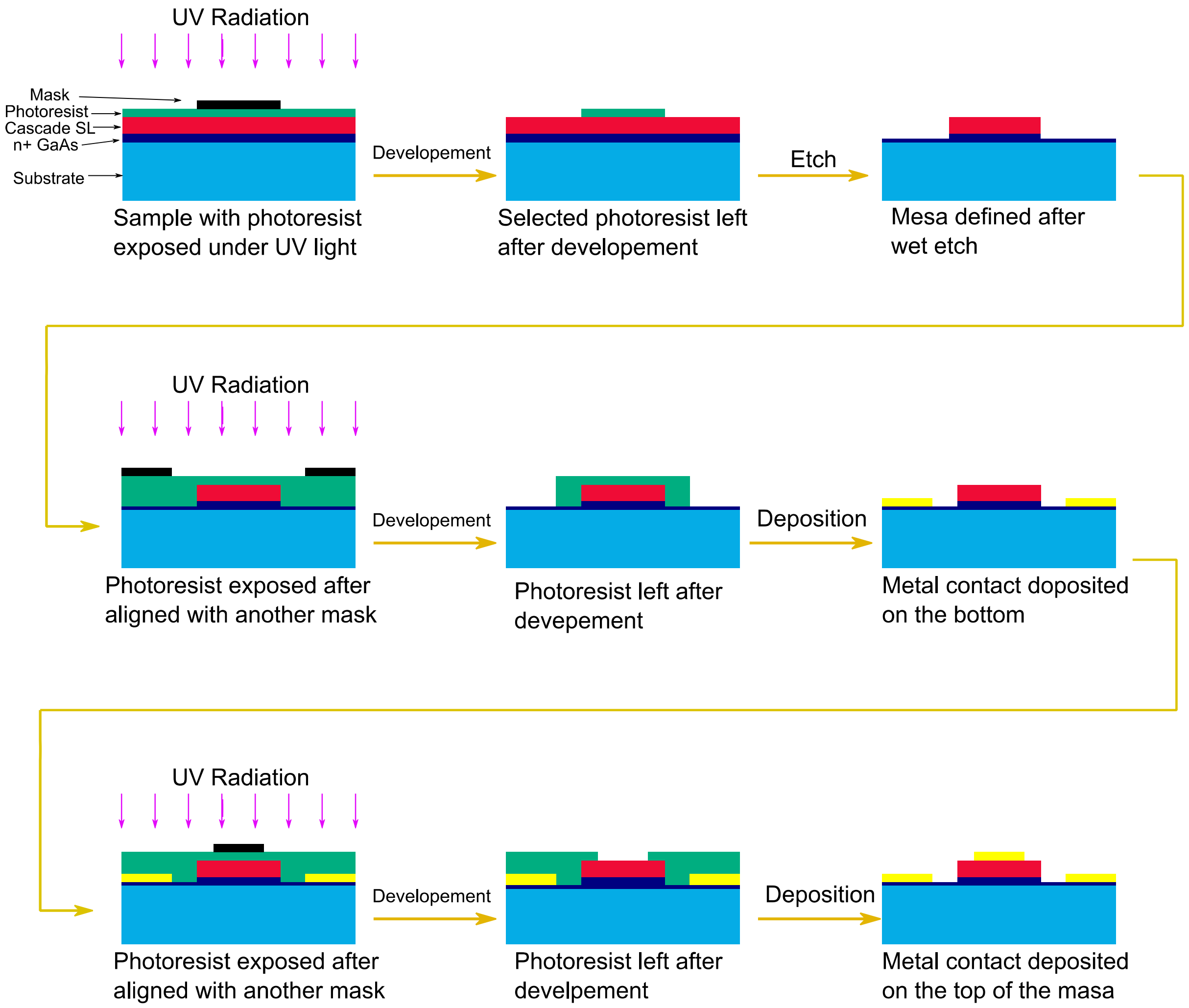

Figure 3.11 Schematic diagram of the technological processes to fabricate the semi-insulating surface plasmon structures.

- The second step is performed to provide NiGeAu alloyed ohmic contacts as bottom contacts. Image reversal photoresist Ti35ES was used in this lithography stage, since edges of this photoresist have undercut profile, which allow the later lift-off process after metal deposition. The mask alignment and development follow the same procedure as previous lithography. Ni/Au/Ni/Ge/Au was deposited on the n+ layer about 50 µm away from the mesa, following by the rapid thermal annealing to form alloyed ohmic contact. The annealing was carried out at 400^{o}C and lasted 1 min.

- The third step is to deposit the metallic non-alloyed Schottky contacts on the top of epitaxial layers as the top contact. The process was the same as the bottom contact process. Ti/Au was deposited on top of the mesa, but not annealed. Indeed, if the top metal is annealed, the dopants under the metal film can diffuse into the active region and contaminate it. Moreover, the diffusing of the dopants induces thick heavy doping area, which can increase the free electron absorption of the THz radiation. The top Schottky contact formed by Ti/Au metal and 50 nm heavily doped n^+GaAs layer is reported as 0.8 V [4].

3.3.2 Double metal structure

The major steps of the double metal structure processing procedure are illustrated in Figure 3.12. The detailed procedure can be found in Appendix

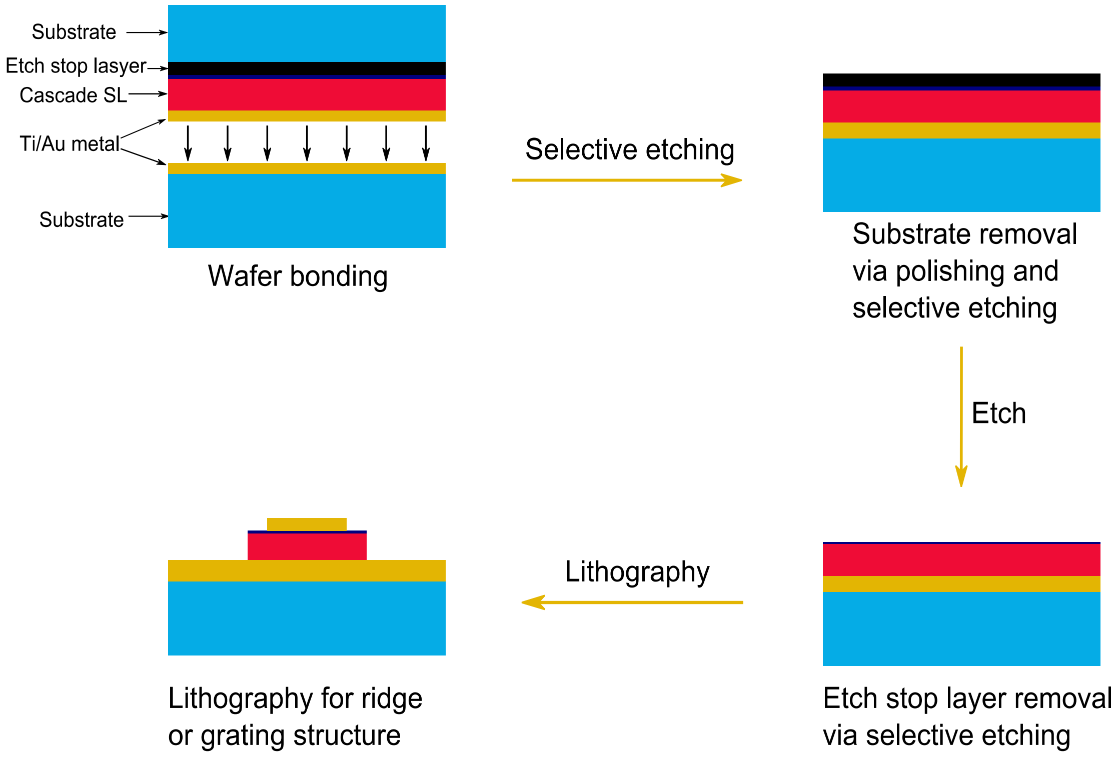

Figure 3.12: Schematic diagram of the technological process for the fabrication of the double metal structures.

After the MBE growth, the wafer was cleaned with solvent and acid. Ti/Au (10nm/500nm) metal was then deposited on the top. A piece of semi-insulating GaAs substrate was cleaned and Ti/Au (10nm/500nm) was deposited on it, as the new supporting substrate. The two pieces of wafer were carefully aligned according to the crystal axes, and then thermal compressed together. The firm Applied Microengineering Ltd at UK carried out this process. After the wafer was bonded, the substrate of the original wafer was removed. At first, it was mechanical polished from about 400 μm to 100 μm thick. During the mechanical polishing, the sand papers with grain sizes of 30 μm, 12 μm and 3 μm were subsequently used to keep uniform surface and avoid grooves. Care should be taken to make sure not only the surface uniform but also the etching thickness uniform, as big nonuniformity of the substrate thickness may induce thinner part being the over etched in the subsequent wet etching. The remaining substrate was selectively etched by citric acid/H_2O_2 solution. Citric acid monohydrate, hydrogen peroxide and DI water were mixed with the ratio of $C_6H_8O_7$:H_2O_2:H_2O (3g:1mL:3mL) for preparing the solution. The selectivity of GaAs versus $Al_{0.45}Ga_{0.45}As$ as high as 200 has been reached [54] for this composition. We used $Al_{0.5}Ga_{0.5}As$ as a stop layer, which would give much higher selective etch ratio. The etch stop layer of 300 nm is used for all our samples. When the substrate was all etched, the surface became mirror like, which was a good indication that this process was finished.

Following substrate removal, the etch stop layer was also removed. 300 nm thick $Al_{0.5}Ga_{0.5}As$ on top of the GaAs was selectively etched by HF. A longer time of more than 2 min is preferred for this etching for totally removal, due to extremely high selectivity of $Al_{0.5}Ga_{0.5}As$ over GaAs in HF solution[55]. Beneath the etch stop layer, the 600 nm heavily doped layer, which original used as bottom ohmic contact for semi-insulating structures, was thinned to about 100 nm, to limit the free electron absorption.

After the previous processing, the wafer was processed in two technological stages. First, the mesas on the epitaxial layers were defined with the same procedure than the one used for the processing of semi-insulating surface plasmon waveguides. Secondly, the metallic non-alloyed ohmic contacts were deposited on the epitaxial layers to do the top contact. At last, to facilitate the device mounting and to reduce the thermal dissipation, a metal layer of Ti/Au (10nm/200nm) was on the backside of the sample. The sample is then ready for its mounting and for the realization of wire bonding.

3.3.3 Device mounting

The processed semi-insulating structures and double metal structures were mounted onto sample holders made of copper. The processed samples were leaved into small device pieces, containing one or two mesas. The device pieces were soldered with Indium on a copper surface, with two electrical pads on both sides. An Au wire was then used to connect the top contact with one pad, serving as positive electrode. The bottom contact of the mesa was connected to the copper holder using gold wire, which was then connected to a negative electrode. Figure 3.13 shows the mounted and bonded device, where the gold bonding wire is connected with the pad.

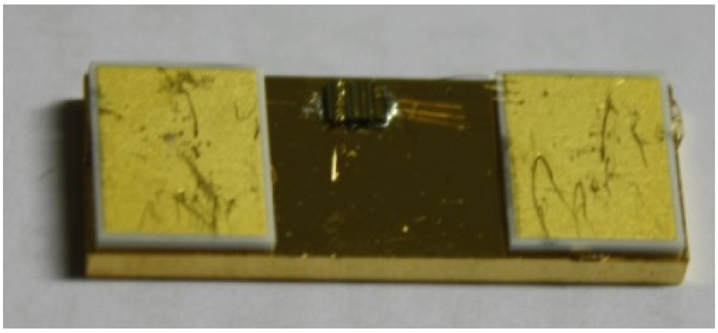

Figure 3.13: Schematic of a mounted and bonded device.

3.4 Experimental set-up

To study these doped cascade super-superlattice devices, we carried out three measurements. At primary, the current-voltage (I-V) characteristics of the devices were measured to study the electron transport and band alignment in the devices. Then, we used Fourier Transform Infrared Spectroscopy (FTIR) measurements, to measure the spectrum of the THz radiation emitted by these devices. To probe the gain with the aim to observe the dispersive gain predicted semi-classically and with quantum-mechanic, we performed THz time domain spectroscopy (TDS) measurements.

As mentioned previously, the top and bottom contacts of each mesa were connected to two electrodes; the bias is applied between these electrodes. The bias value on the samples was measured using oscilloscope and the current was measured using a homemade current sensor. All the measurements were performed at cryogenic temperature under liquid helium (~10 K) except special indication.

3.4.1 Fourier Transform Infrared spectroscopy

Fourier Transform Infrared spectroscopy (FTIR) is wildly used in measuring the THz intersubband spontaneous emission and stimulated emission for THz quantum cascade structure. It is also used in this thesis to detect THz emission from Bloch oscillations. The detail description can be found in well known text books[56, 57]. The setup for our measurement is Bruker 66V/s. The main measuring path is shown in Figure 3.14.

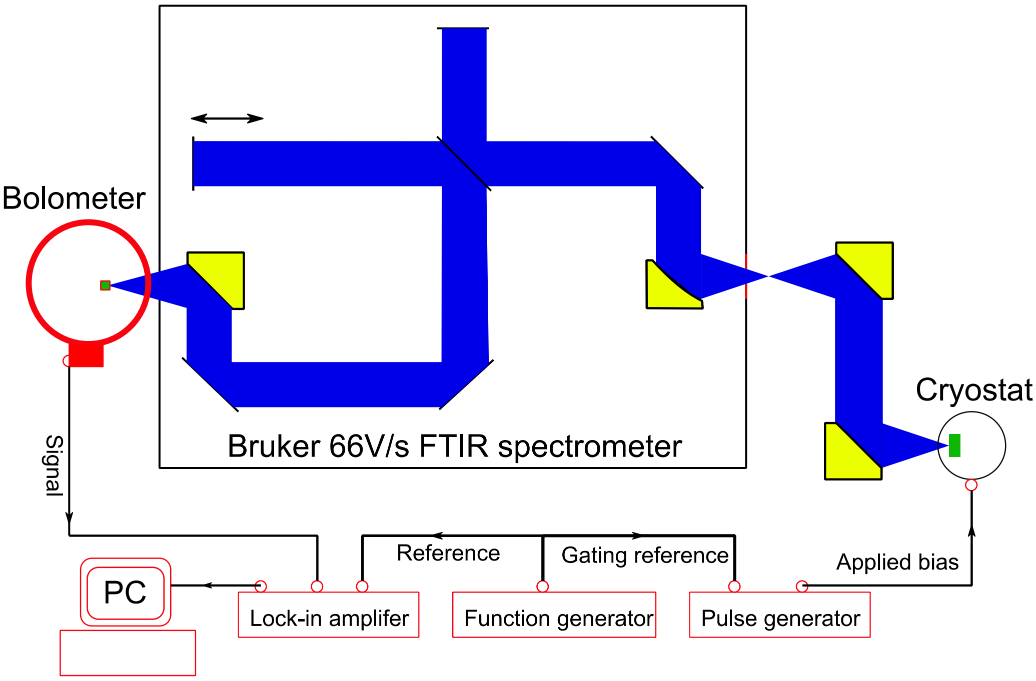

Figure 3.14: Experimental setup for emission measurements based on FTIR spectrometer operating in step scan mode.

The Bloch oscillator device was mounted in the cryostat cold finger, which was kept cryogenic temperature by continuous flowing liquid He. The Bloch emission, either form ridge edge or grating surface, is collected through two parabolic mirrors into the spectrometer. The terahertz emission transported through Michelson interferometer would be detected by the bolometer. A lock-in amplifier was used to suppress the noise. Several key components are illustrated as follows.

Beam splitter

Several different Beamsplitters can be chosen for Bruker 66V/s according to required wavelength. KBr beamsplitter has a broad pass of 375 cm^{-1} to 7000 cm^{-1} (11.4 THz to 212THz) for middle infrared. The Quartz beam splitter ranges from 2800 cm^{-1} to 25000 cm^{-1}, corresponding to 84.8 THz to 757.6 THz. The Mylar beam splitter is for far infrared, with thickness of 6 um, 50 um and 125 um, their passing range is 30 cm^{-1} to 650 cm^{-1}(0.9 THz to 19.7 THz), 10 cm^{-1} to 55 cm^{-1}(0.3 THz to 1.7 THz), and 4 cm^{-1} to 30 cm^{-1}(0.1 THz to 0.3THz). For our consideration, the Bloch oscillations have the working range of around 3THz, which is about 100 cm^{-1}, the Mylar beam splitter with thickness of 6 um is preferred.

Bolometer

The weak Bloch oscillations emission was detected by silicon composite bolometer, together with lock-in amplifier to increase the signal noise ratio. The bolometer is from Infrared Laboratories. The silicon thermal detection module is responsible for the detection, where the silicon element responds to the radiation heating, changes resistance, and then transmits to voltage signal. As the thermal responds time of the silicon element is on the order of millisecond range, the chopping frequency is limited by no more than 400 Hz. In our case, 300Hz was used. The silicon element works in liquid He temperature, which is realized by the heat sink connecting with the liquid He dewar. Since the bolometer is broadband detector, the spectrum selection is controlled by a series of cut-off filters. The two filters responds in our bolometer is shown in Figure 3.15 where the radiation is from the internal Globar source. The filter 1 is more sensitive than filter 2 for the range of higher than 3 THz (100 cm^{-1}), and filter 2 has advantage in frequency lower than 3THz. Filter 1 is selected for our measurement.

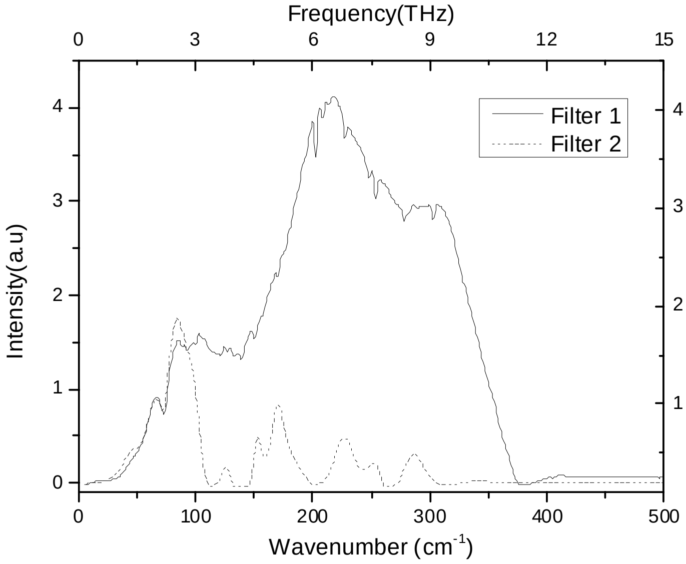

Figure 3.15: Globar emission spectra at 300 K taken with the Si bolometer using Filter 1 and Filter 2.

Step scan mode

The FTIR can work on rapid scan and step scan mode. The step scan mode has the advantage for weak signal measurement, which is the case for our experiment. So the spectra of our samples were achieved in the step scan mode. For the step scan measurement, the translating mirror moves certain distance to get the interferogram of the emission intensity as function of the mirror position. During the movement of the translating mirror, it pauses at each step, and the intensity is recorded by the lock-in amplifier, and then the mirror moves to the next position and pauses again. The interferogram recorded through the whole moving distacne is then Fourier transformed to yield power spectrum. To ensure enough responds time for lock-in amplifier, the pausing time was set 3 times of the lock-in constant time. With 1s lock-in constant time and 282 scanning point, it takes about 14mins for every scan. The AC electrical bias with frequency of 100 kHz and 10% duty cycle was intentionally used to avoid thermal heating and also preserving detectable emission signal. Function generator Agilent 33220A was used to gate the pulse generator at 300Hz as the Lock-in reference for step scan mode operation.

3.4.2 THz time domain spectroscopy

Bloch gain has long been predicted in superlattice under bias, as illustrated in part 2.3. The crossover between THz gain and absorption happens at Bloch resonance. Measuring this electric field depended crossover will give clear evidence of the Bloch oscillation existence. Shimada[21] claimed to have observed gain in optical pumped superlattice, through indirect calculation of the THz transient, although it was doubted by other authors[58]. Until now, no gain related to Bloch oscillation has been obtained directly in superlattice. Gain measurement in THz QCL have been successfully carried out recently using THz TDS[44,45].As the TDS setup is similar with the Bloch emission TDS used in the following chapter, I will just briefly describe the setup and concentrate on the measuring mechanism, detailed information of the THz time domain spectroscopy setup can be found in chapter 4.

Figure 3.16 shows the THz TDS setup developed by S. Dhillon and J. Tignon at LPA (ENS), which I used for the absorption/gain spectra measurements. The Ti: Sapphire femto-second laser provide 100 fs laser at 800 nm wavelength with modulation frequency of 76 MHz. the photoconductive inter-digitated antenna under bias is illuminated by femo-second laser and generates THz transient. The emitted THz is collected and focused on the Bloch oscillator devices. As the relative long wavelength of THz, the focus beam is estimated of about 300 μm diameter under diffraction limit. To well couple the THz beam in to the waveguide, the semi-insulating surface plasmon ridge waveguide device is preferred comparing with double metal waveguide for large mode area and easy coupling. The focused THz transient transmits through the device and was detected by 200 μm GaP electro-optic crystal. THz frequency up to 4.5 THz can be well detected with this crystal. A delay line stage was mounted on the probe beam to map out the whole THz pulse transient. A lock-in amplifier was used to increase the signal noise ratio with the reference frequency given by the modulated bias on the antenna. Figure 3.17 shows the THz time domain transient measured in the setup and the frequency spectrum calculated by the Fourier transform of the measured THz time domain transient without Bloch device.

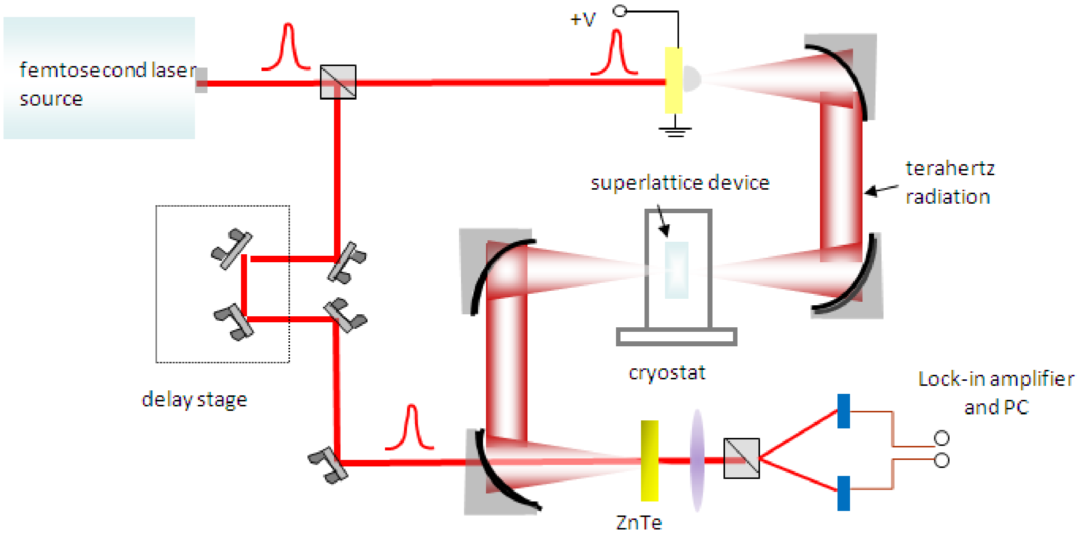

Figure 3.16: Schematic drawing of the THz time domain spectroscopy setup developed by S. Dhillon and J. Tignon from LPA (ENS).

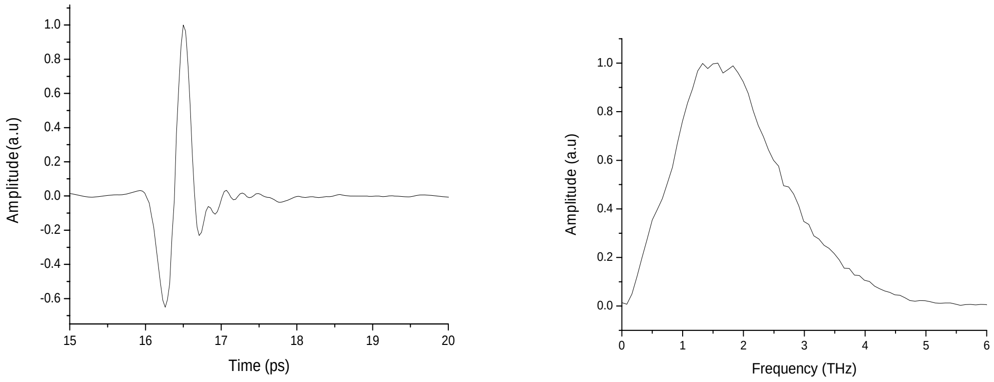

a b

Figure 3.17: Temporal waveform (a) and amplitude spectra (b) emitted by the photoconductive antenna and detected by the electro-optic sampling technique.

The basic idea to obtain the gain and loss of the Bloch oscillator is comparing the transmitted THz pulse when the biased is on and off. The difference between these two will give gain and loss induced by the bias. The basic assumption in this method is that the absorption induced by the waveguide, substrate or doping layer is the same for bias on and off. The easy way is to direct measurement THz spectra with bias on or off, and compare these two to have gain or loss information. But the problem is that the input THz pulse intensity is small and the device gain or absorption, which is normally narrow band, overlaps only a small extremity of the input THz bandwidth, which induces low sensitivity. So another technique was developed by previous authors in LPA (ENS) [59, 60], where our experiments were also carried out.

The transmitted THz at frequency ω from the sample can be written as

$$S(\omega) = T\exp[-\alpha L/2 + i\Delta k_{\alpha} L]\exp[-\gamma L/2 + i\Delta k_{\gamma} L]E_{in}(\omega) \qquad 3.6$$

$$R(\omega) = T\exp[-\alpha L/2 + i\Delta k_{\alpha} L]E_{in}(\omega) \qquad 3.7$$

The $S(\omega)$ and $R(\omega)$ represent the transmitted THz field with bias on or off respectively. The T is the THz coupling coefficient for in and out the sample. α and $\Delta k_{\alpha}L$ are the loss and loss induced phase of the waveguide. Here they are supposed to be the same for bias both on and off. γ and $\Delta k_{\gamma}L$ are the sample gain and gain induced phase. The previous equations are in frequency domain, the time domain correspondences are $S(t)$ and $R(t)$.

During the measurement, the antenna bias was modulated at 50 kHz with duty cycle of 50%, it is the same to say that the generated time domain THz pulse is in modulated in 50 kHz. The waveguide ridge sample is biased in 25 kHz pulse with duty cycle of 25%. This pulse width is the same with antenna electrical bias, but is turned off for every another antenna pulse (see Figure 3.18). The two pulse generators are phase locked and the 25 kHz was send to the lock-in as the reference. In this case, the lock-in measured the difference between the signal with the sample bias turned on and off:

$$Diff(t) = \pm(R(t) - S(t)) \qquad 3.8$$

This is the difference signal in time domain, the corresponding difference signal in frequency domain is obtained by the Fourier transform:

$$Diff(\omega) = \pm[R(\omega) - S(\omega)] \qquad 3.9$$

The problem of this method is that it is hard to know whether R-S or S-R is measured, so whether it is gain or loss is determined by reference measurements.

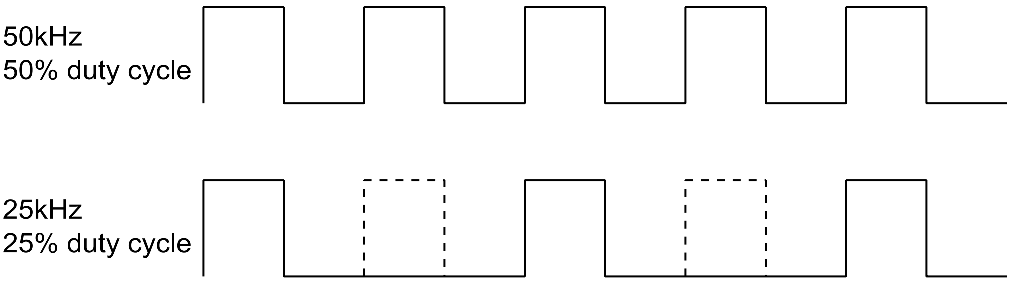

Figure 3.18: Schematic of the modulation technique of the photoconductive antenna and of the Bloch device used for the absorption/gain measurement.

By taking a reference scan $R(\omega)$ when the sample bias is off. The gain or loss can be calculated as

$$\exp[-\gamma L/2 + i\Delta k_{\gamma} L] = [Diff\,(\omega) \pm R(\omega)]/R(\omega) \qquad 3.10$$

From this, both gain and phase change for the waveguide can be calculated:

$$\gamma = \frac{2}{L}\ln\left(\frac{\left|Diff\,(\omega) \pm R(\omega)\right|}{\left|R(\omega)\right|}\right) \qquad 3.11$$

$$\Delta\varphi = \arctan\left(\frac{\mathrm{Im}[Diff\,(\omega)]\,\mathrm{Re}[R(\omega)] - \mathrm{Re}[Diff\,(\omega)]\,\mathrm{Im}[R(\omega)]}{\mathrm{Im}[Diff\,(\omega)]\,\mathrm{Re}[R(\omega)] + \mathrm{Re}[Diff\,(\omega)]\,\mathrm{Im}[R(\omega)]}\right) \qquad 3.12$$

3.5 Result and discussion

Several measurements will be discussed in this part to verify the structure design and processing and also to provide essential feedbacks for future improvement.

3.5.1 I-V characteristic

a) Experimental Set Up

For the I-V measurement, the device mounted on the cryostat was connected to an Agilent 8114A pulse generator. The top n+ contact layer was connected with the ground and similarly the bottom n+ was connected with the source, so that reverse bias voltage was applied on the device. Thus, the structure is in negative polarity. For instance, the corresponding band structure for the sampleL358 is shown in Figure 3.19. In order to avoid thermal contribution, the I-V characteristics were measured in a pulse mode with voltage pulses of 1250 ns duration at a repetition rate of 1 kHz.

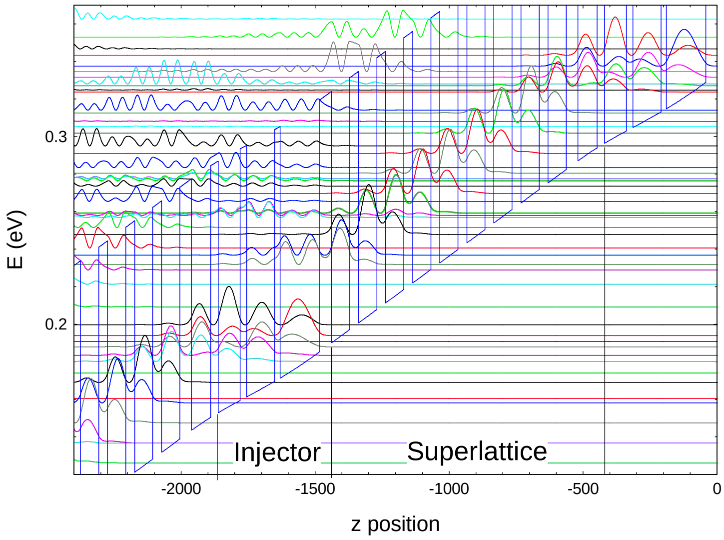

Figure 3.19: Self-consistent conduction band profiles of L358 sample under negative polarity ($E_{applied}$=10 kV/cm)

The electrical properties of the devices provide insight into the evolution of the band structure with the applied electric field. Information can be gathered on negative differential conductance regime and alignment of the energy bands on these structures. Indeed, under an electric field ranging from 6 kV/cm to 10 kV/cm according to the considered samples, the resonance condition is reached and electrons can cascade throughout each period of the super-superlattice structure: electrons are resonantly injected into the each elementary superlattice. Far-infrared emission is expected to occur via a diagonal transition of electrons between the WSLs (first miniband) of the quantum wells of the elementary superlattices. The injector is used to extract electrons from the each elementary superlattice and channel them into the next period by resonant tunneling and phonon-assisted transition. As this process relies on resonant transport through the quantum wells, signatures are observed in the current-voltage characteristics.

b) Results

L358

The I-V characteristic of the sample L358 with mesa size of 475 μm×610 μm and with a surface grating period of 40 μm(filling factor 50%) is shown in Figure 3.20. Up to 2 V, the current does not flow indicating that there is no electric field inside the active layer. This voltage offset is thus related to additional series resistances in the device mostly due to the non-alloyed Schottky contact[4], and this voltage offset decreases with the temperature increase as will discussed later. When a small electric field (voltage) is applied inside the active layer (3 V<V<9 V), the current density increases since the tunneling current can flow through the superlattice miniband and the periods within the structure begin to align to the desired configuration. As the field is increased (9 V<V<13 V), an alignment between the energy subbands in adjacent wells is getting worse and we observe a reduction of the slope of the I-V characteristic resulting from the competition between the driving force (electric field) and subbands mismatch. When the field is increased further (V>13 V), whereas the subbands misalignment is still increases, the transport is efficient again and the current density begins to increase as at low electric field. At high electric field, the current is dominated both by the conduction over the quantum well barriers and the escape into the continuum and by the intersubband Zener tunneling. The later mechanism results from the alignment in the super-superlattice structure, of the lower subband of quantum wells with the upper subband of neighbor quantum wells. Due to these contributions in the current at high electric field, the region of negative differential conductance is not visible in the voltage range where the subbands mismatch is significant too strongly localized the wavefunctions on their own WSL; instead only a decrease of the differential conductance with the increase of the voltage is observed. Note that the effective electric field inside the super-superlattice cannot be easily deduced from the applied voltage value V due to the additional contribution of contacts in the drop voltage but since the thickness of active layers are l~10 μm, the effective field in the super-superlattice structure is in the range of V/l.

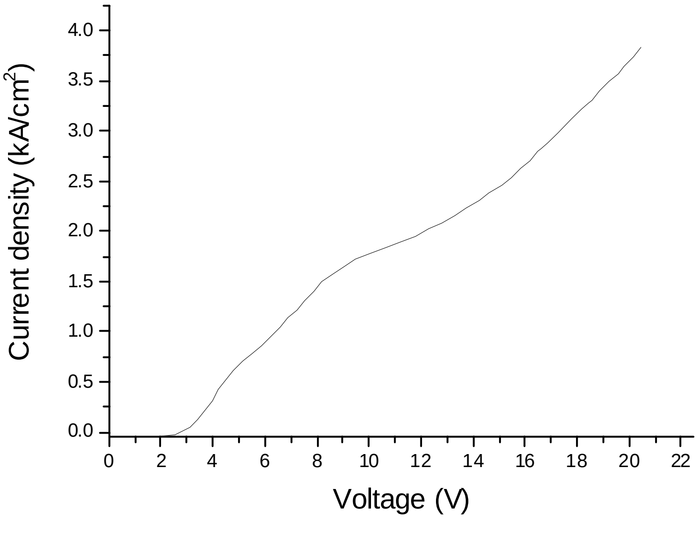

Figure 3.20 Current density versus voltage at 10 K in pulsed mode for L358sample.

To extract information related to the energy band alignment, I have plotted on Figure 3.21 the differential conductance as a function of the applied voltage. Such representation highlights resonances and changes in the slope of the I-V characteristic. As mentioned previously, once the drop voltage at the Schottky contact is compensated, the current density starts to increase with the increase of the electric field. As the electric field increases, the electron wavefunction tends to be localized, and a decrease of the differential conductance is expected; that's what we observed between 3 V and 6 V. A slight increase of the differential conductance is observed around 7 V, the exact interpretation remains to be answer, but one possible reason is the following. As can be seen on the band structure profile at 8 kV/cm (Figure 3.22 a), the wavefunctions of excited states in the injector overlap with the wavefunctions of the Wannier Stark ladders in the superlattice. This overlap may cause parasitic current injection into the continuum, increasing the differential conductance of the sample. The minimum of the differential conductance arrives at 11 V, which corresponds to an applied electric field in the range of 11 kV/cm. As can be seen from the band profile (Figure 3.22 b), at such applied electric field, the electron wave functions of the WSLs in the superlattice are relatively localized and no wavefunction overlap with the excited states in the injectors is observed. Further increase of the applied electric field is expected to induce negative differential conductance since the electron wavefunctions in the superlattice are more strongly localized and the subbands in the injector tend to mismatch. However, an increase of the differential conductance instead of a negative differential conductance is observed. This increase of the differential conductance at a bias voltage higher than 12 Vis related to both the conduction over the quantum well barriers and the escape of electrons into the continuum, and to the intersubband Zener tunneling preventing the observation of the negative differential conductance. In addition, we observed some local rises in the differential conductance at 12.5 V, 15.8 V and 17.5 V. These rises may be due to the alignment of the wavefunctions of excited states in the injector with the wavefunctions of the Wannier Stark ladders in the superlattice (as seen in the conduction band profile at an applied electric field of 12 kV/cm in Figure 3.23).

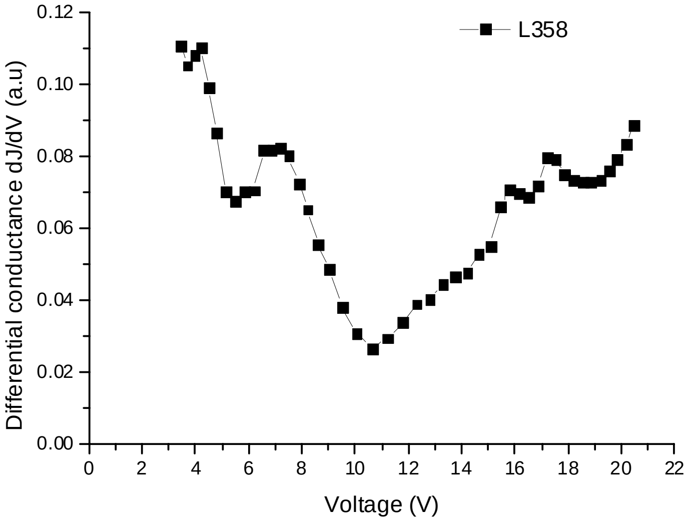

Figure 3.21: Differential conductance as function as voltage at 10 K in pulsed mode for the L358 sample.

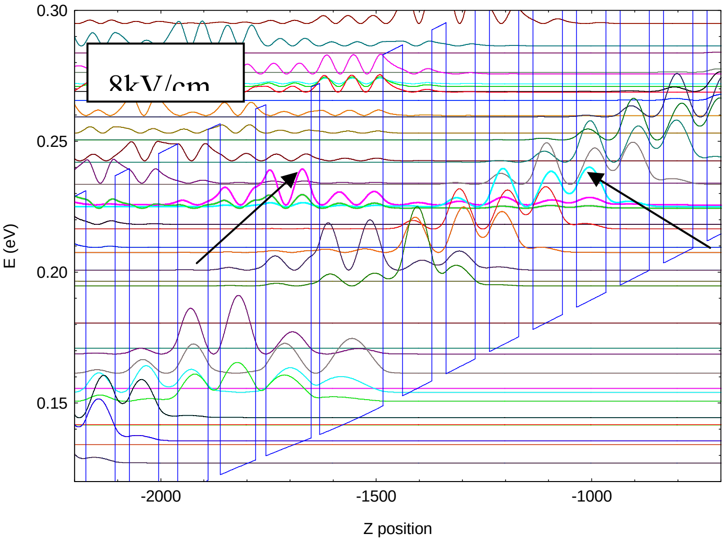

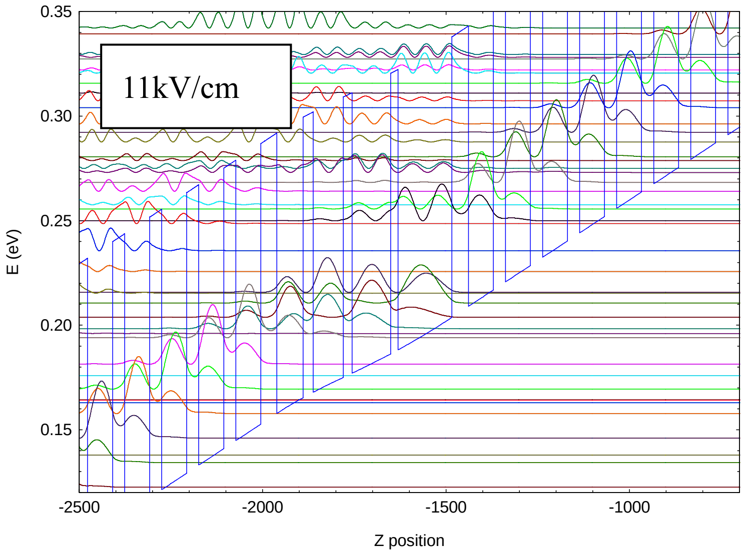

Figure 3.22: Self-consistent conduction band profiles of L358 sample for an applied electric field of 8 kV/cm and of 11 kV/cm.

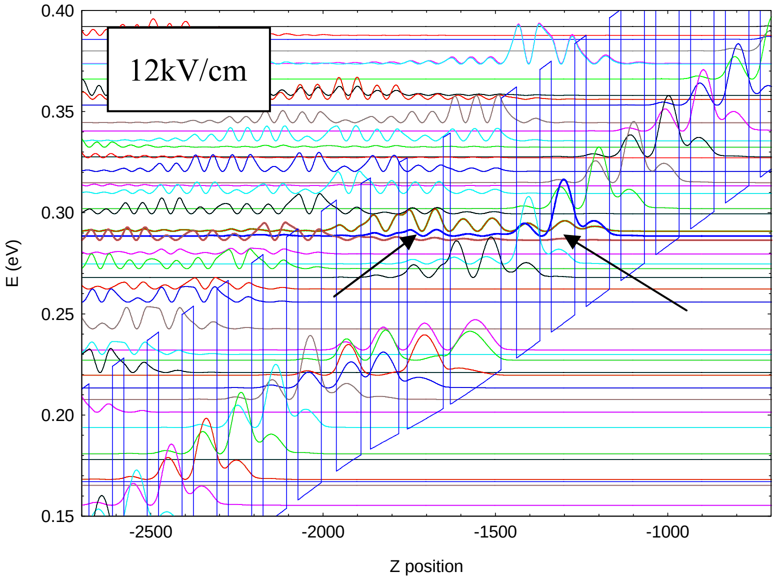

Figure 3.23: Self-consistent conduction band profile of L358 sample for an applied electric field of 12 kV/cm.

The I-V characteristic was also measured at different heat sink temperatures. In the measurement, the small mesa with 130 μm × 130 μm was used to reduce the thermal accumulation. Keithley model 2400 Sourcemeter was used to act as the power source as well as to record the current. The results are shown in Figure 3.24. As discussed in chapter 2, the increase of the temperature induces thermal broadened distribution of electrons in the conduction band, and reduces the conductance. For small miniband, the electron miniband transport presents thermal saturation [61, 62]. The semiclassical Boltzmann transport equation gives the temperature dependence of the conductance along the superlattice region:

$$\sigma(T) = \sigma_0 \frac{I_1(\Delta/(2k_B T))}{I_0(\Delta/(2k_B T))} \tag{3.13}$$

Where $I_n(x)$ are the Bessel functions of complex argument and $\sigma_0 = Ne^2\tau_z/m_z$ is the Drude conductivity with τ_z and m_z, the momentum relaxation time and effective mass along the superlattice axis. For the L358sample, the width of the first miniband is 24 meV. I calculated the relative conductance as a function of the temperature; the result is shown in Figure 3.25. With the increase of the temperature, the relative conductance decreases. This means that the current in the superlattice region should decrease with the temperature increase, which is not what we observe in Figure 3.24. The measured increase of the current in the L358 sample as the temperature increase is attributed to the involving of the injector region. When the temperature increases, the electrons gain higher energy, which may assist them to escape to the excited band of the injector or to the higher minibands. Even through the contribution of the parasitic current competes with the reduction of the current resulting from the subbands mismatch at intermediate applied electric field, the change in the slope of the I-V characteristic at intermediate electric field is still observed until 220 K. The Figure 3.24 inset shows the enlarged part of the current at low voltage. A reduction of the offset voltage with the increase of the temperature is observed, which is consistent with the reduction of the Schottky barrier expected as the temperature increases[63].

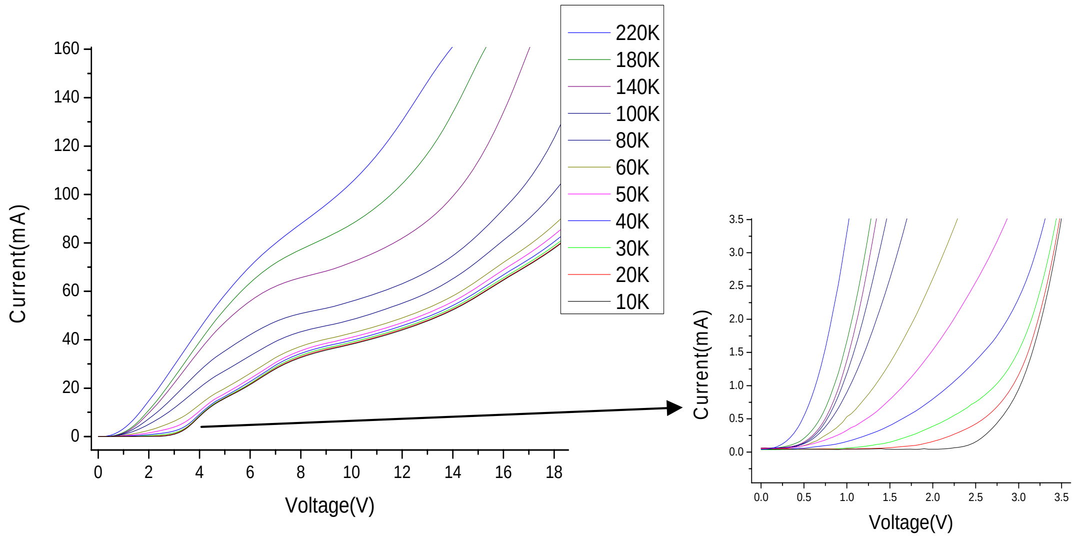

Figure 3.24: Current versus voltage for L358 sample with 130 µm×130 µm dimensions at different temperatures from 10 K to 220 K. The inset shows the enlarged part of the voltage offset.

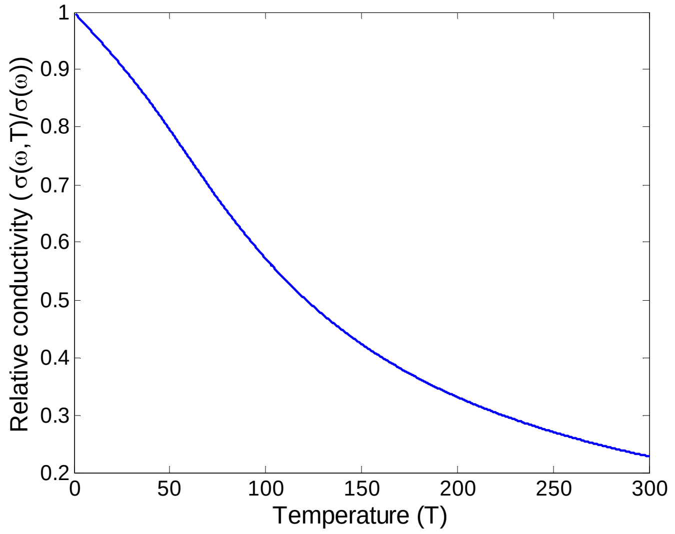

Figure 3.25: The calculated miniband relative conductance of superlattice as function of the temperature[61]

L414 and L416

The samples L358, L414, and L416 have the same design except the density of the doping and its profile. L358 sample is doped only in the injector wells and barriers with 1×10^{16}cm^{-3} doping density. L414 sample is doped in the injector wells and barriers with 4×10^{16}cm^{-3}. For the L416 sample, not only the injector is doped with 4×10^{16}cm^{-3}, but also the superlattice module with a doping density of 8×10^{15}cm^{-3}.

Figure 3.26 displays the I-V characteristics of the samples L358, L414 and L416 with mesa size of 475 µm×610 µm and second order metallic grating on the mesa. For the L414 sample, the increase of the current until ~6 V corresponds to the electron flow through the superlattice and the injector regions. Between 6 V and 12 V, a reduction of the slope of the I-V characteristic is still observed, even through this effect is less pronounced than in the L358 sample. This lowing of the current increase with the voltage increase is attributed to the electron wavefunction localization in the WSL of the superlattice region. Above 12 V, the current increases almost linearly with the applied electric field. The current characteristic of the L416 sample is different to the previous two samples, on the overall voltage range, the current increases almost linearly, no reduction of the slope of the I-V curve is observed.

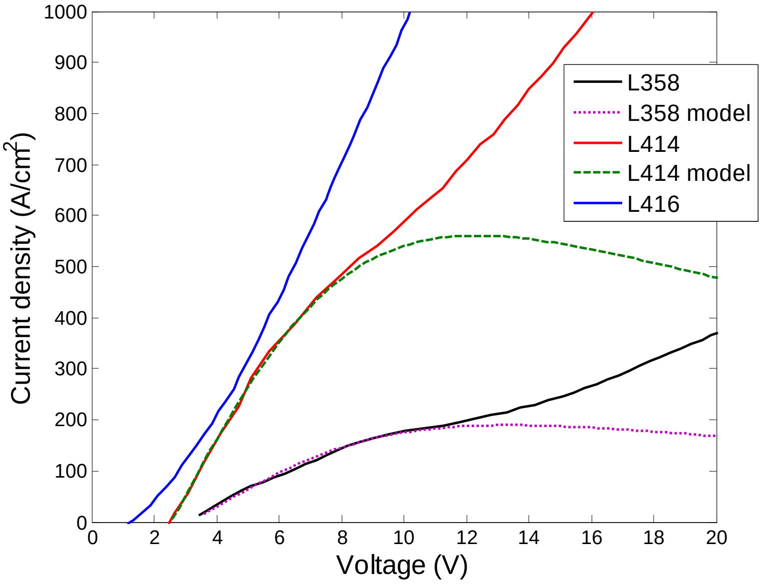

Figure 3.26: I-V characteristics at 10 K for the samples L358, L414 and L416 with mesas of 475 µm×610 µm. The dashed lines are the fits using the Esaki-Tsu model.

The dashed lines in Figure 3.26 are the fits of the I-V characteristics using the Esaki-Tsu model given by the equation 2.20:

$$j = Aen_d v_{drift} \frac{\hbar}{\tau} \frac{ed(\frac{U-U_0}{l})}{(\frac{\hbar}{\tau})^2 + (ed(\frac{U-U_0}{l}))^2} \tag{3.14}$$

where n_d is the sample doping density, v_{drift} the electron drift velocity, τ the scattering time, A is constant of proportionality, U_0 accounts for the voltage drop at series resistance (Schottky contacts) and l the superlattice active region thickness.The dashed lines are the currents versus voltage calculated with $n_d=2.7\times10^{16}$ cm^{-3} for sample L414 and $n_d=9\times10^{15}$ cm^{-3}for sample L358 (these values are close to the design values), $v_{drift}=0.95\times10^5$cm/s and $\tau=67$ fs for both samples, $U_0=3.6$ V for L358 sample and $U_0=2$ V for L414 sample and l =10 μm for both samples.

The differential conductances of the samples L358 and L414 are calculated and reported in Figure 3.27.As analyzed previously, the differential conductance decreases as the electron wavefunction tends localization, which is observed from 3 V to 11 V for the L358 sample and from 3 V to 9 V for the L414 sample. The differential conductance minimum of the L414 sample appears earlier than the L358 sample. As these samples preserve the same multilayer stack except the doping density, this difference can be explained by the non-uniform distribution of the electric field in the superlattice and the injector region. The two band profiles at 10 V are shown in Figure 3.28. We see that the injector region of the L414 sample experiences a smaller electric field because of the higher doping density. So, for a same electric field applied to the sample, the superlattice region in the L414 sample is subjected to a higher electric field.

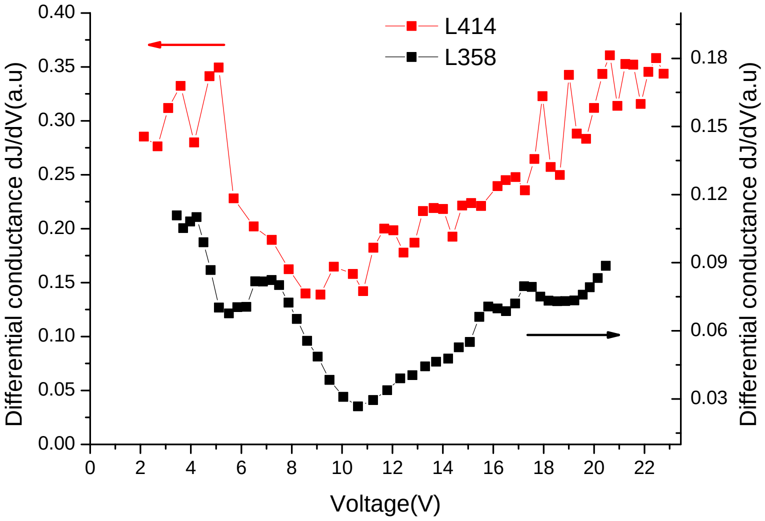

Figure 3.27: Differential conductance versus voltage at 10 K in pulsed mode for the samples L358 and L414.

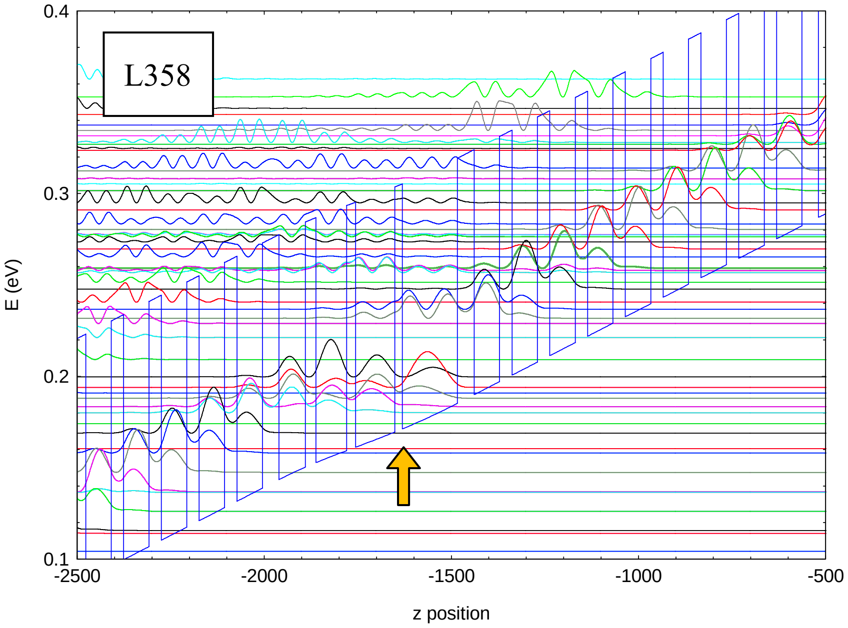

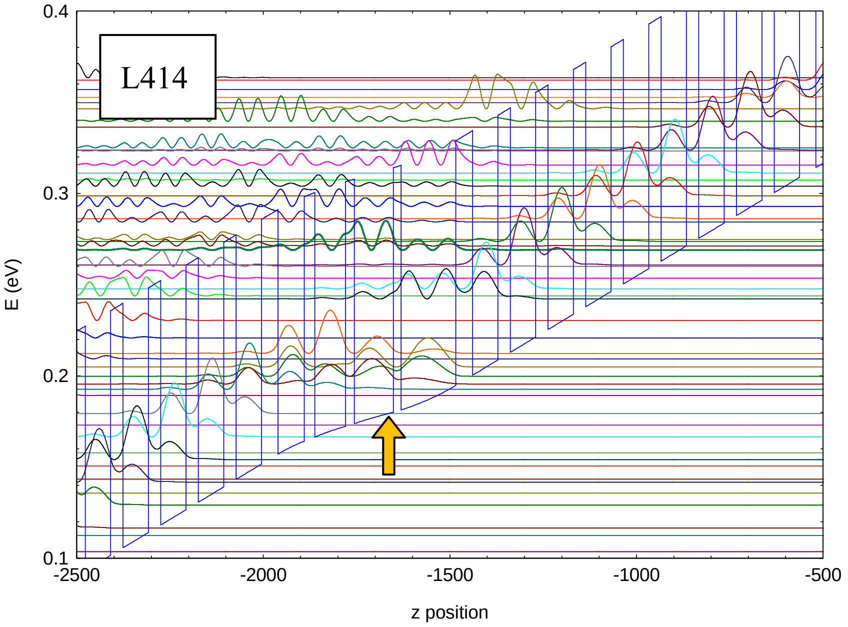

Figure 3.28: Self-consistent conduction band profiles of the L358 sample (upper) and the L414 sample (lower) for an applied electric field of 10 kV/cm. The arrows show the region of the doped injector where the electric field is weaker.

The differential conductance of the L416 sample is calculated and reported in Figure 3.29. The differential conductance increases first with the increase of the applied electric field below 6 V, as the subbands of the injector are gradually aligned for resonant tunneling. Then the differential conductance saturates. No reduction of the differential conductance is observed. As can be seen in Figure 3.26, the current densities in the L416 sample are higher than in the samples L358 and L414, which cause higher thermal dissipation. The thermal heating assists the parasitic current channels and prevents the observation of a reduction of the conductance[20]

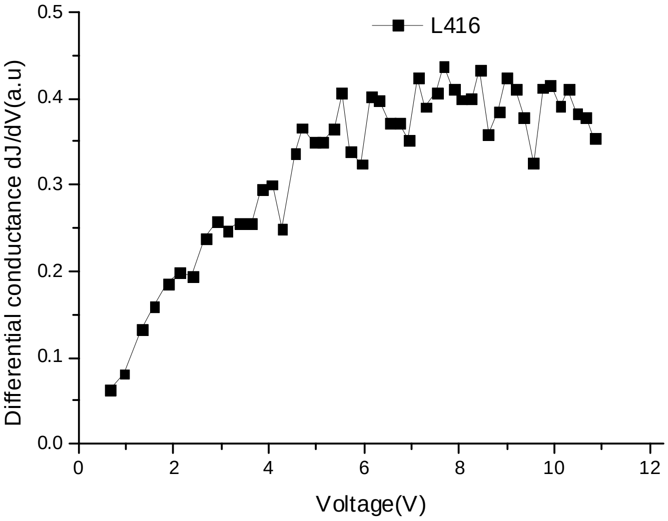

Figure 3.29: Differential conductance as function voltage at 10 K in pulsed mode for the L416 sample.

To conclude, the increasing of the doping density in the samples L414 and L416 did not benefit to the observation of the negative differential conductance in the super-superlattice structure. On contrary, a leakage of current to the excited states of the injector or continuum band is observed. To reduce the electron conduction over the quantum well barriers and their escape into the continuum, new material systems with higher barrier height must be chosen. We have selected the alternative material system $Al_{0.33}Ga_{0.67}As$/GaAs since the height of the barrier is increased from 134 meV to 295 meV. Using thus material system, I have designed and fabricated a second series of samples: samples L527 and L665.

L527

Except the height of the barriers, the L527 sample design is nearly the same than the L358 sample. The module sheet doping density was set as $6.465\times10^{10}cm^{-2}$, keeping similar with L358. Based on the gain measurements of L358 that will be discuss after, we modify the four-well injector to three-well injector to reduce the THz absorption in the injector region. Figure 3.30 shows the measured I-V characteristic and its fit with the Esaki-Tsu model in dashed line. The discrepancy between data and the fit at low voltage is due to the role of the injector, not accounted in the model: the subbands in the injector are not aligned to provide electron tunneling. The conduction band profile for the L527 sample under an applied electric field of 2 kV/cm is reported in Figure 3.31. The electron wavefunctions are not well overlapped at this low electric field, which induces a slow increase of the current. To get further information of the conduction band alignment, the differential conductance is extracted from the data and plotted in Figure 3.32, together with the one extracted from the fit. Once the subbands in the injector are gradually aligned, the resonance condition is reached providing an efficient electron transport through the super-superlattice structure, which is indicated by the increase of the differential conductance between 3 V and 6 V. Then, the differential conductance decreases up to 12 V. As given by the model, this reduction of the differential conductance comes from the localization of the wave functions in the quantum wells of the superlattices. A main result is the observation of the negative differential conductance between 11 V and 20 V. In this voltage region, we observe a plateau of the negative differential conductance, which is the result of the competition between the current reduction induced by the electron wave function localization in the superlattice and the current increase induced by the electron tunneling to excited states in the injectors and intersubbands Zener tunneling. Above 20 V, the latter mechanisms dominate the current transport and a rise of current versus the voltage is observed.

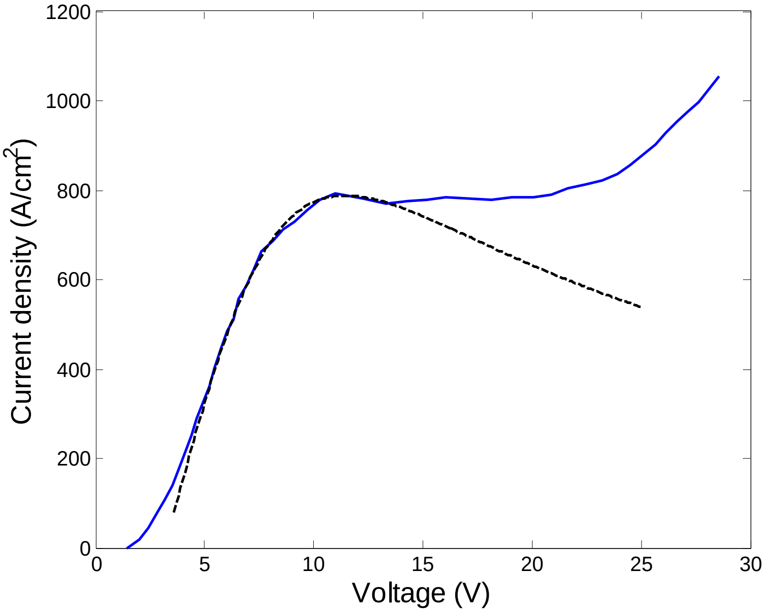

Figure 3.30: Current density versus voltage at 10 K for the L527 sample. The dashed lines is the fitting using the Esaki-Tsu model with the, drift velocity of $v_{drift}=2.25\times10^5$cm/s, scattering time of 83 fs, doping density of $n_d=9\times10^{15}$ cm^{-3} and voltage offset of $U_0=3.6$ V.

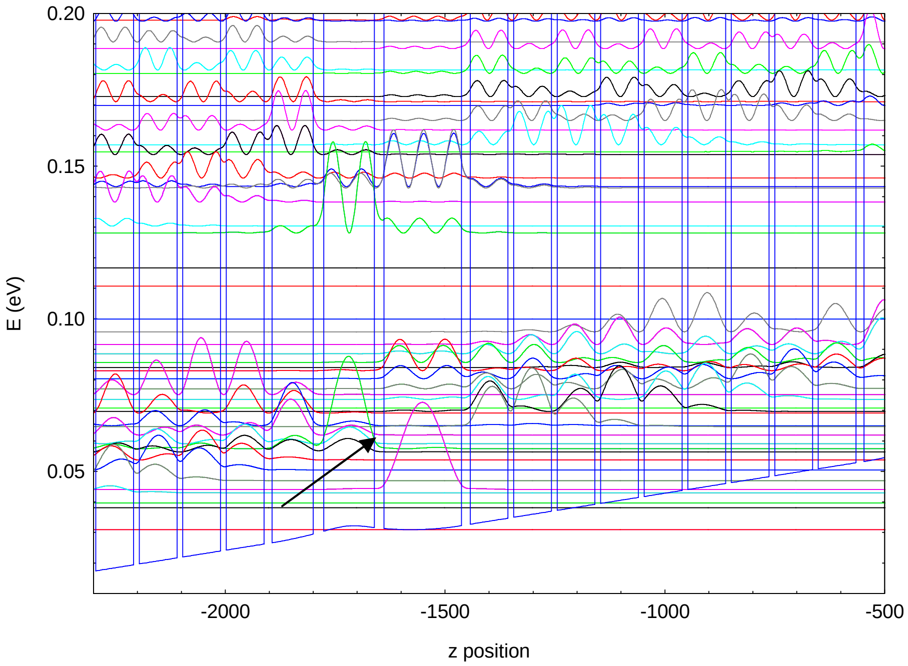

Figure 3.31: Self-consistent conduction band profiles of the L527 sample for an applied electric field of 2 kV/cm.

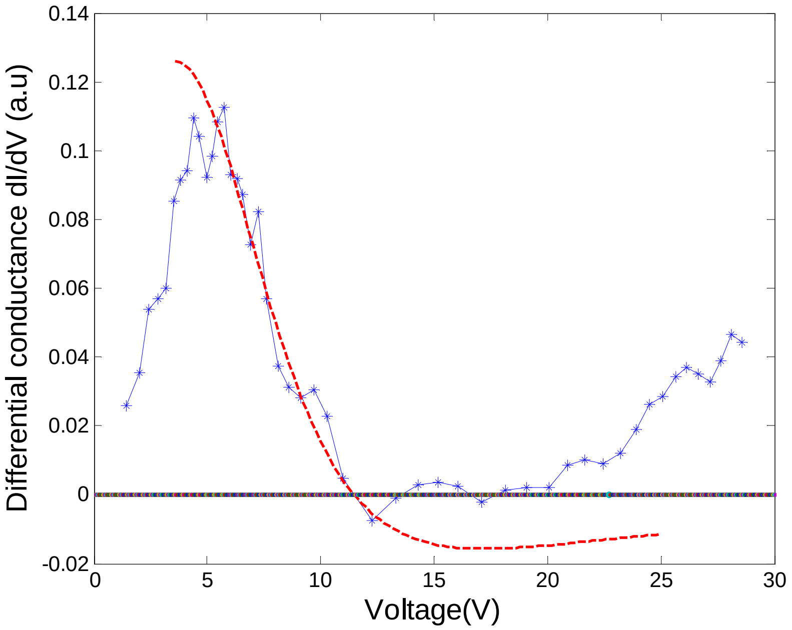

Figure 3.32: The differential conductance versus voltage at 10 K for the L527 sample. The dashed lines are the fits using the Esaki-Tsu model.

L665

The sample L665 was designed in the same way than the L527 sample, except that the superlattice region consists of 5 periods of unit cells instead of 9 periods in the L527 sample and only the barriers in the injectors region are doped with a module sheet density of 6.3 × 10^{10} cm^{-2}. The I-V characteristic of the L665 sample is depicted in

. The extracted differential conductance of the L665 sample is illustrated in Figure 3.34. At low voltages below 5 V, the current increases because the energy subbands in the injectors are gradually aligned for resonant tunneling. Between 5 V to 7 V, the current differential conductance decreases when the electron wave functions become localized in superlattice region. An abnormal sudden decrease of differential conductance from 7 V to 9 V was observed. To reveal the reason of this sudden decrease of differential conductance, energy band structure profile with applied voltage between 7 V and 9 V was investigated. A tunneling channel was observed in the energy band structure profile at 7.55 V, however tunneling channel causes increasing of current not decreasing. So the origin of this unstable behavior is not clear. Indeed, strong localization of electron wave function in the injector region was observed at 9.7 V, as indicated by the arrow in Figure 3.35. This explains the negative differential conductance at 9.7 V. For voltage higher than 9.7 V, the current plateau persists with slightly increasing. This characteristic stems from the competition between reducing of current because of electron localization and increasing of current because of electron tunneling to excited states in the injectors.

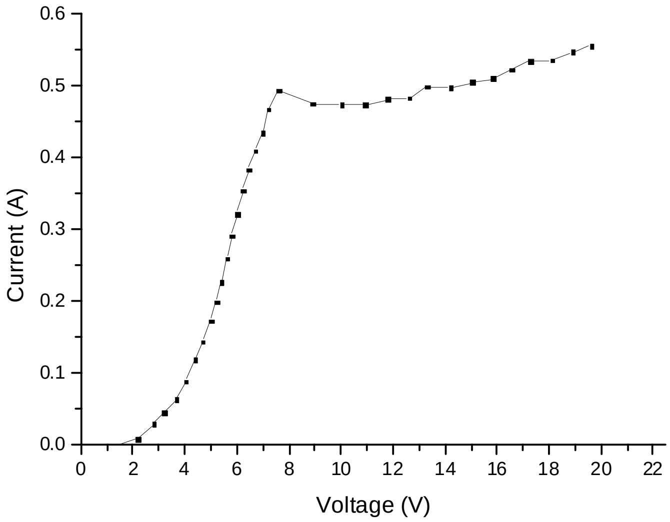

Figure 3.33: Current versus voltage at 10 K in pulsed mode for the L665 sample.

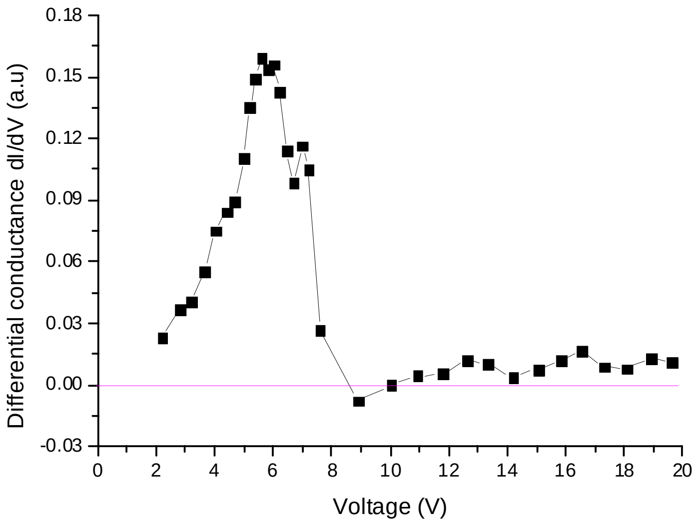

Figure 3.34: Differential conductance versus voltage at 10 K in pulsed mode for the L665 sample.

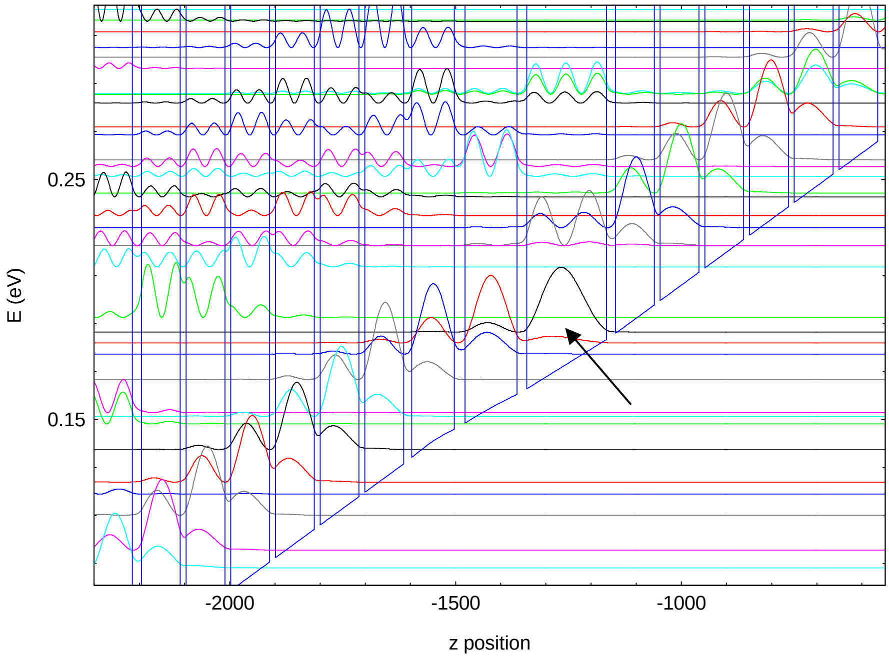

Figure 3.35: Self-consistent conduction band profiles of the L665 sample for an applied voltage of 9.7 V.

3.5.2 Electroluminescence measurements

The electroluminescence spectra of all the samples listed in Table 3.2 were measured. The samples were processed into ridge waveguides or surface emitting grating devices. As pointed out previously, the THz emission resulting from second-order transitions is TM polarized. This is one of the criteria to identify the emission related to Bloch gain. The surface grating couples out only the TM polarized emission, whereas the edge-emitting ridge waveguide allows the THz emission with both TM and TE polarization. To detect only the TM polarized emission, we used a grating polarizer. The second criteria to identify the emission related to Bloch gain is the linear shift of the peak frequency of the emission with the bias voltage since the Bloch frequency increases linearly with the applied electric field. The results of several measurements are presented and discussed in this section. All the measurements were carried out at 10 K. The resolution of the step scan mode is 8 cm^{-1}.

L358 surface emitting grating device

Figure 3.36 shows the emitted light intensity versus the current (L-I) and the V-I curve of L358 from surface-emitting device at 10 K. The mesa is 475 μm×610 μm, and the surface grating periods is 30 μm with 50% filling factor. Between 10 V to 13 V, we observe a reduction of the conductance due to the localization of electron wave functions in the quantum wells of the superlattices as discussed previously, and this is in this voltage range that the emission related to Bloch gain is expected. The electroluminescence intensity was recorded using the lock-in amplifier. We observe that the electroluminescence signal increases as the increase of the current (voltage bias). We also measured the spectra of this sample with FTIR operating in the step scan mode, but we didn’t observe reliable spectra, because of their extremely low emission intensity.

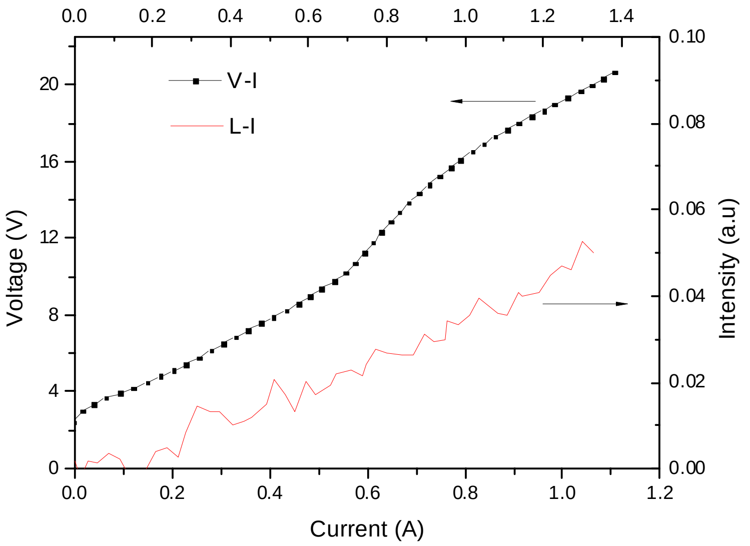

Figure 3.36: V-I and L-I curves for L358 surface-emitting sample at 10 K. The mesa is 475 μm×610 μm, and the surface grating periods is 30 μm with 50% filling factor.

L416 semi-insulating surface plasmon ridge waveguide

The L416 semi-insulating surface plasmon ridge waveguide was tested and the measured V-I and L-I characteristics are shown in Figure 3.37. The light emission of the ridge waveguide was coupled directly from the edge of the ridge. Comparing with the surface-emitting device, both TE polarized and TM polarized edge emission is coupled out. The identification of the origin of the emission is performed by selectively detecting the TE polarization and the TM polarization of the electroluminescence with the grid polarizer. Both TE and TM polarized emissions are measured and shown in the Figure 3.37. From the L-I curve, it is observed a change in the phase of the measured signal from the lock-in. Indeed, the emission intensity first increases in absolute value up as the current increases up to 1.2 A but with a phase opposite to the signal measured at higher current (I>1.2 A) which increases with the increase of the current up to 1.5 A. This change in the phase of the signal indicates that there exist at least two different emission mechanisms, which with opposite phases. The TE and TM polarized emissions give relatively similar features but with different intensities, indicating that the detected signal is not only a thermal emission. Indeed, thermal emission provides no distinguishable features for the TE and the TM polarization.

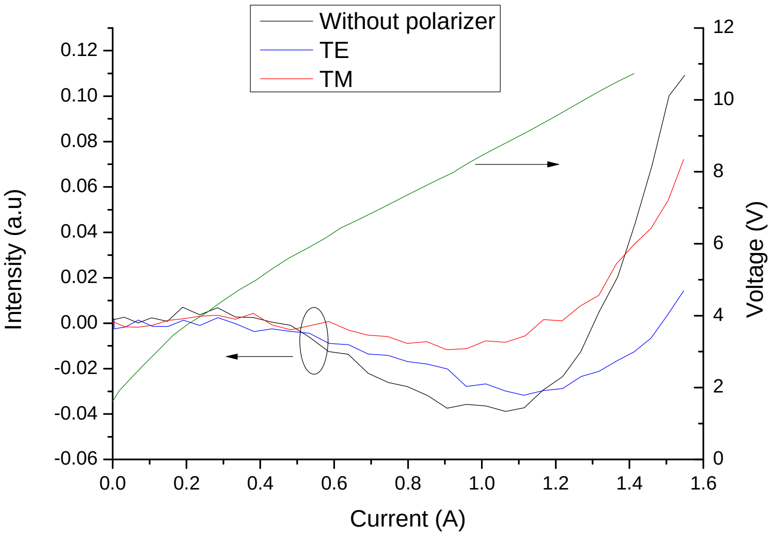

Figure 3.37: V-I and L-I characteristics for L416 semi-insulating surface plasmon waveguide at 10 K. The TE and TM polarized L-I characteristics were also measured using a grid polarizer.

The emission spectra were recorded at 9 V (1.1 A) without polarizer, as well as for TE and TM polarizations. The spectra are reported in Figure 3.38. For TE and TM polarized emission, the emission intensities are weak. Two broad peaks centered at 11 meV and 35 meV are observed for TM polarized emission and three broad peaks centered at 8 meV, 21 meV and 35 meV are observed for TE polarized emission. To verify the reliability and reproducibility of the spectrum, two spectra without polarizer and in the same experimental conditions were recorded at 9 V, as shown in the Figure 3.38. It is clear that due to the weak intensity of the signal the reproducibility of the spectra is poor.

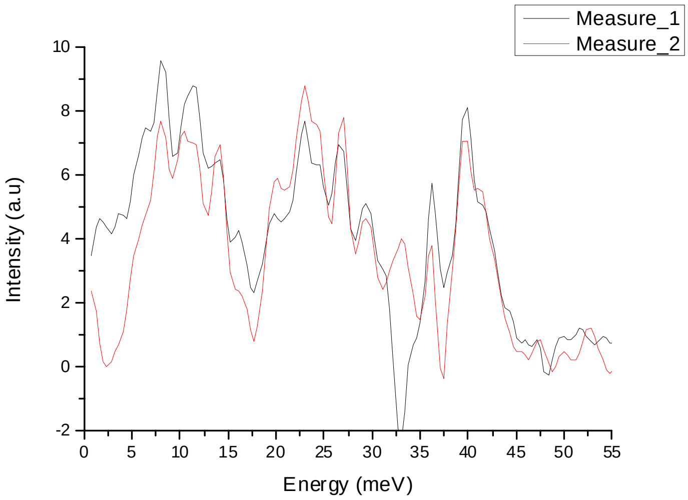

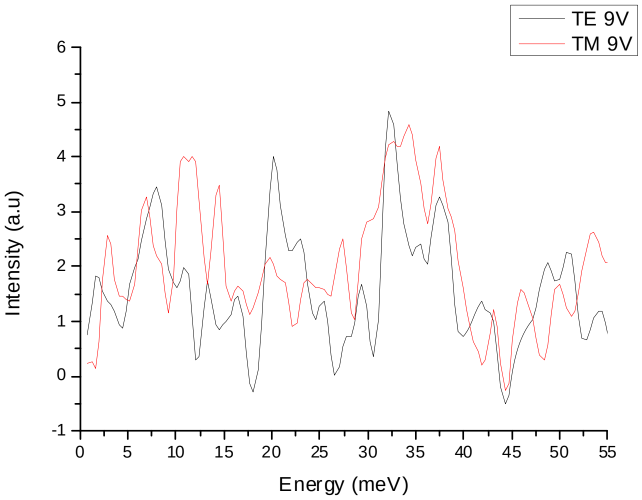

Figure 3.38: L416 spectra at 10 K from ridge waveguide biased at 9 V, measured without polarized (upper) and for TE and TM polarizations (lower).

L527 semi-insulating surface plasmon ridge waveguide

Figure 3.39 shows the V-I and L-I curves for L527 semi-insulating surface plasmon ridge waveguide. The device size is 500 μm×145 μm. As discussed in the previous part, the differential conductance of the device is negative between 14 V to 24 V, and we also observe some small fluctuations of the current in this voltage range. The TE and TM polarized emissions were recorded as a function of the current (L-I curve). At low current (I<0.55 A), the light intensity is extremely weak for both polarizations. The emission intensity begins to increase just before the transport regime with negative differential conductance starts. The TE polarized emission shows higher intensity than the TM polarized one. We measured the emission spectra (Figure 3.40) with FTIR spectrometer at the voltage corresponding to the transport regime with negative differential conductance. For the TE polarized emission, we observe one broad peak (FWHM=5.1meV) centered at ~22 meV (5.45 THz), and its intensity increases with the increase of the bias voltage. To verify the reproducible of the measurements, the spectrum at 14 V were measured twice, and the similarity of each other demonstrates the relatively good reliability of our measurements. For the TM polarized emission, we also observe the broad peak centered at 22 meV (5.45 THz) but with lower intensity. The intensity of the broad peak also increases with the increase of the bias voltage. The fine satellite peaks on the main peak region are always the same. These may come from the combination of beam splitter, filters, and windows in the FTIR spectrometer and the bolometer. These fine satellite peaks add difficulties for interpreting the data. Due to its polarization mainly TE, we expect that this broad peak centered at 22 meV is not related to perpendicular current through the super-superlattice but could rather originate from in-plane current. Such lateral exists for instance in the n+-doped GaAs layer beneath the active layer and used for the bottom contact. The TM polarized emission spectrum also shows another broad peak (FWHM=7.6 meV) centered at ~9.7meV (2.4 THz). The intensity of this peak is relatively constant with the increase of the bias voltage. This low frequency peak has the promising characteristic to be only TM polarized so it can be attributed to vertical transport through the super-superlattice structure. If this low frequency peak emission would originate from Bloch gain, according to the calculation of the energy splitting of the WSL, changing the applied voltage from 10 V to 18 V should shift the peak frequency from 10 meV to 18 meV. However, no clear shift is observed in the spectra when changing the bias voltage.

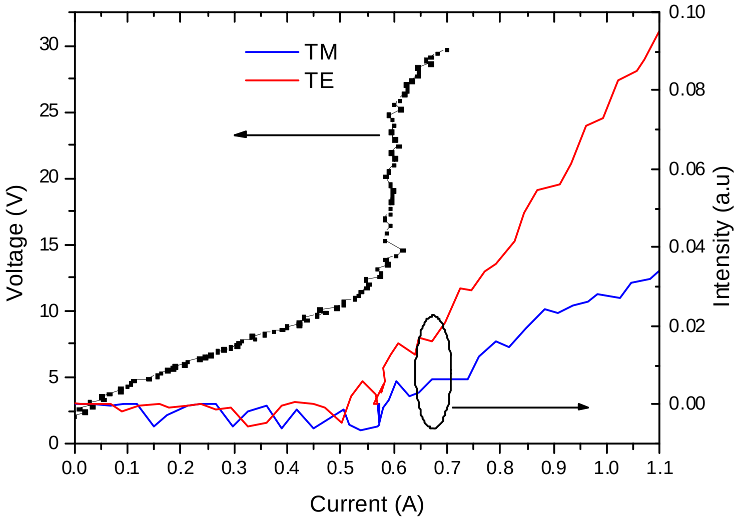

Figure 3.39:V-I and L-I characteristics for L527 semi-insulating surface plasmon ridge waveguide at 10 K. The TE and TM polarized L-I characteristics were measured using a grid polarizer.

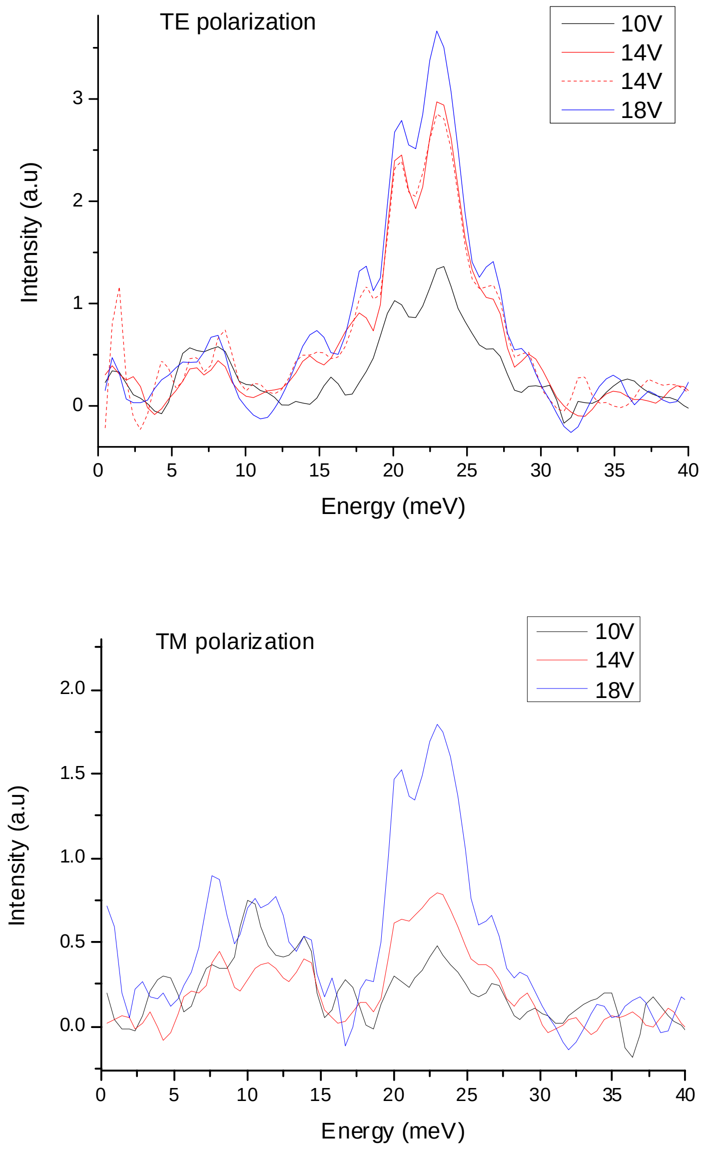

Figure 3.40: L527spectra at 10 K from ridge waveguide at different bias voltages and for TE polarization (upper) and TM polarization (lower).

L527 subwavelength-grating surface emitting device

To improve the extraction efficiency of the THz radiation emitted by our devices, I processed subwavelength-grating devices, where the grating period on the surface is in the subwavelength range giving broadband coupling efficiency[64].

Figure 3.41 gives the L-I and V-I curves of the L527 subwavelength-grating surface emitting device. The mesa size is 300 μm×400 μm. The V-I characteristic shows the similar negative differential conductance character as the ridge waveguide device. The L-I curve also indicates that the emission starts to increase when the negative differential conductance regime is reached, but with a steeper increase. We measured the spectra at several bias voltages within the negative differential conductance region. From the measurements reported in Figure 3.42, we observe that all the spectra show the broad emission peak centered at ~9.7 meV (2.4 THz), which is the same than the one measured with the ridge waveguide in TM polarized configuration. All the satellite peaks didn't change with the change of the bias voltage. No frequency shift as function of voltage is observed. Besides, a small peak from 1 meV to 4 meV gradually appears as the voltage increases. The FTIR spectrometer is not sensitive to this low frequency region as discussed before, so this peak may comes from the noise.

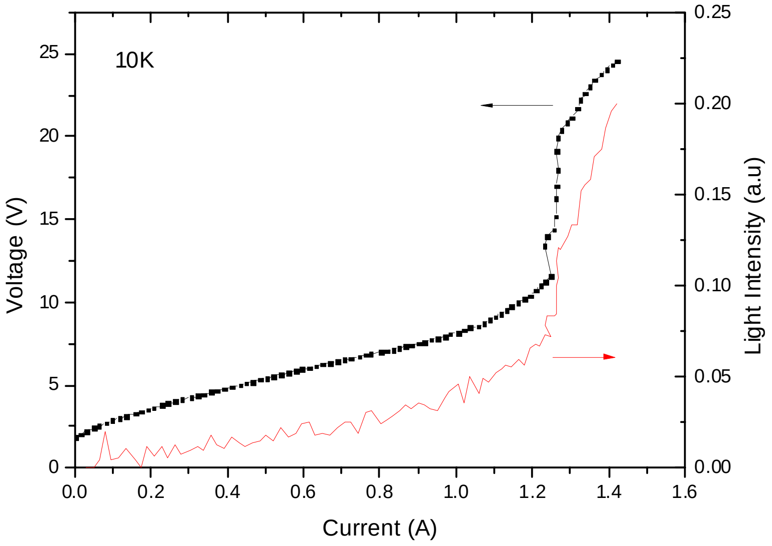

Figure 3.41: L-I and I-V plots at 10 K for L527 subwavelength-grating surface emitting device. The mesa size is 300 μm×400 μm, the grating period is 16 μm, with a filling factor of 50%.

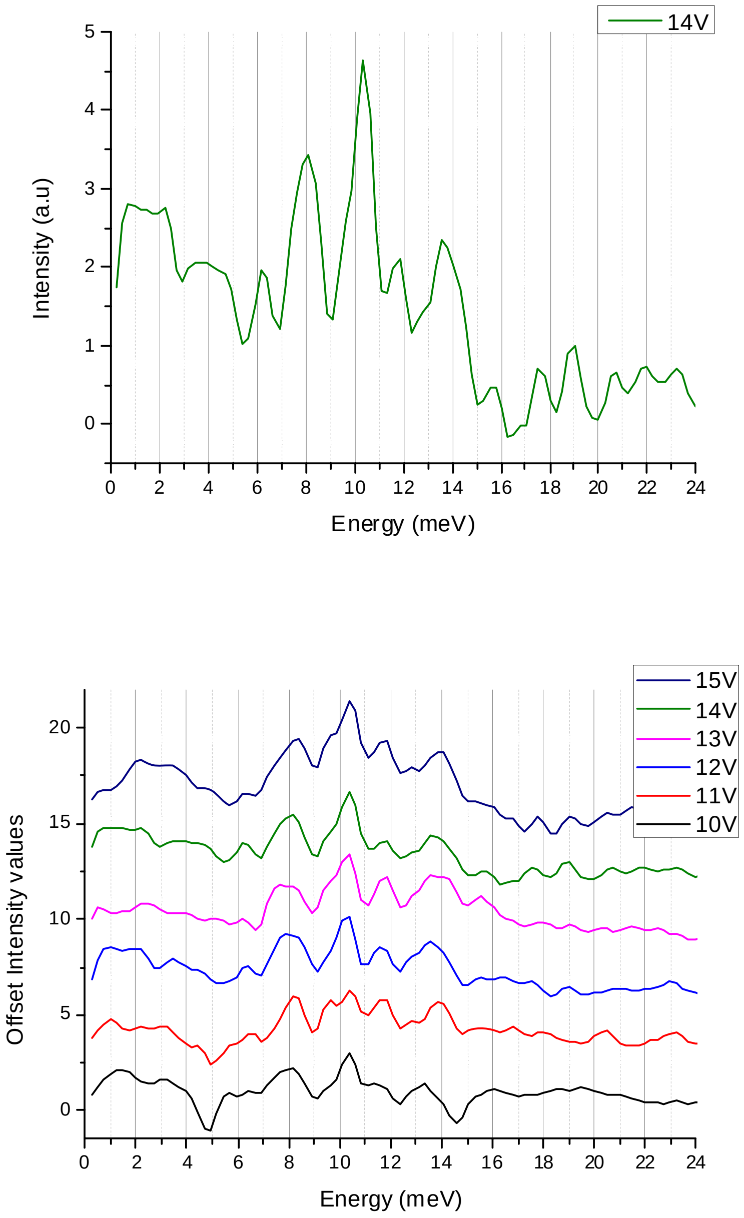

Figure 3.42:L527 spectra at 10 K from subwavelength-grating surface emitting device at different bias voltages.

L527 double-metal subwavelength-grating surface emitting device

I process some devices with metal-metal waveguides since such waveguides have the advantage of low loss and strong mode confinement. However,the strong confinement of the THz mode into the active region with subwavelength dimensions induces a strong divergent of the emitted radiation. By employing surface subwavelength-gratings, the divergence is reduced and the TM polarized THz emission is well coupled out from the large surface. The sample L527 was processed into a double metal subwavelength-gratingsurface emitting device. The L-I and V-I curves are illustrated in Figure 3.43. The sample in use has the size of 400 μm × 400 μm. The V-I shows only a decrease of differential conductance at intermediate bias voltage, and the emission intensity increases very slowly with the increase of the current. The Figure 3.44 shows the emission spectra from the double-metal L527 device at different bias voltages around the negative differential conductance region. We observe an extremely broad peak centered around ~10 meV whose intensity increases with the voltage increase. This peak is relatively similar to the one observed in the TM polarized emission spectra of the L416 sample. Likewise, there is not clear evidence that the emission frequency peak shift with the applied voltage.

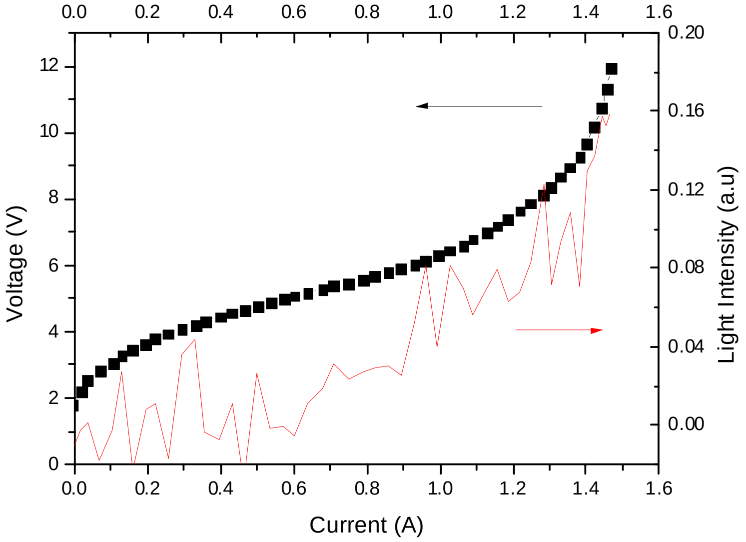

Figure 3.43: L-I and I-V plot at 10 K for L527 double metal subwavelength-grating surface emitting device. The mesa size is 300 μm×400 μm, the grating period is 16 μm, with filling factor of 50%.

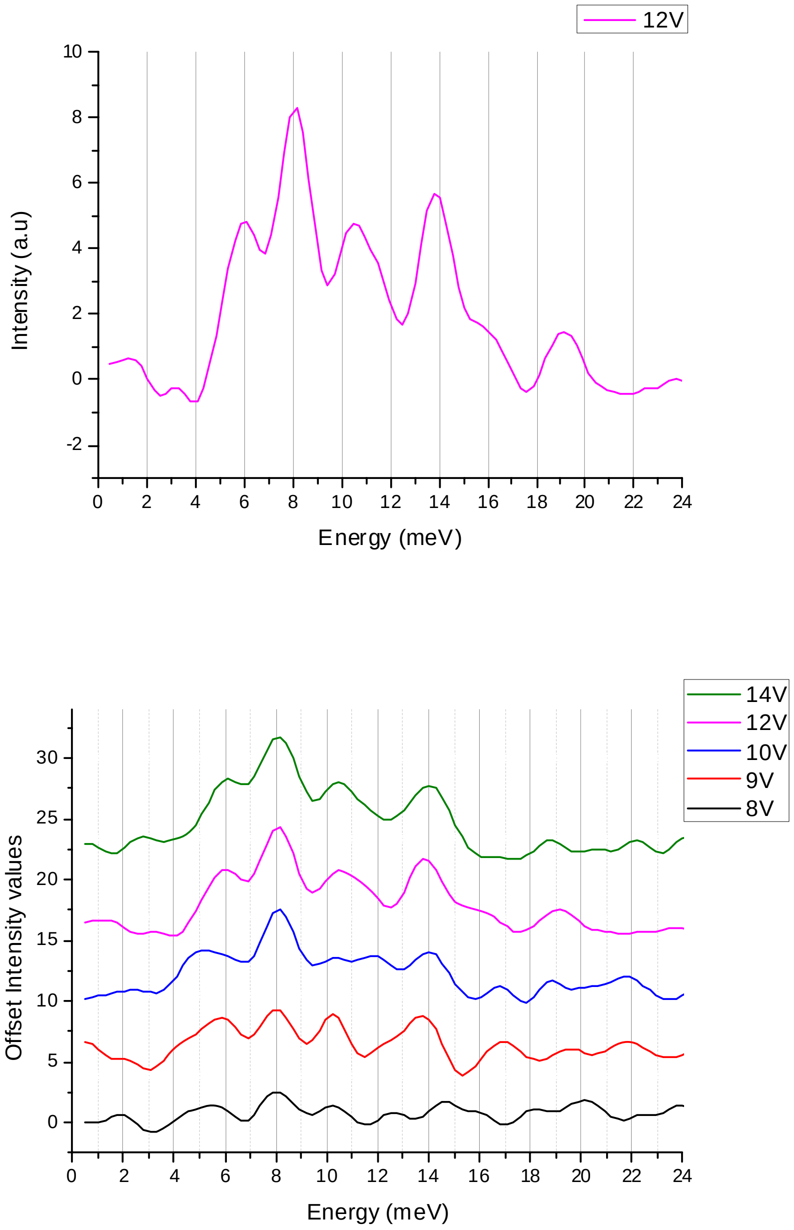

Figure 3.44: L527 emission spectra at 10 K from double metal subwavelength-grating surface emitting device at different bias voltages.

Lateral current emission and comparison

In most of the measured spectra, two main peaks are observed: one broad peak centered at ~22 meV (5.45 THz) mostly TE polarized and one broad peak centered at ~9.7 meV (2.4 THz), which is TM polarized. Even if the FWHM of these peaks is changed from one sample to the other, their central energy (or frequency) is similar for all the samples. As I have suggested previously, the TE polarization of the high frequency peak let us to believe that the emission may originate from an in-plane current as the one flowing in the n+-doped GaAs layer. To identify the origin of these two broad peaks, I prepare specific samples to apply a voltage across contacts on the bottom n+-doped GaAs layer.

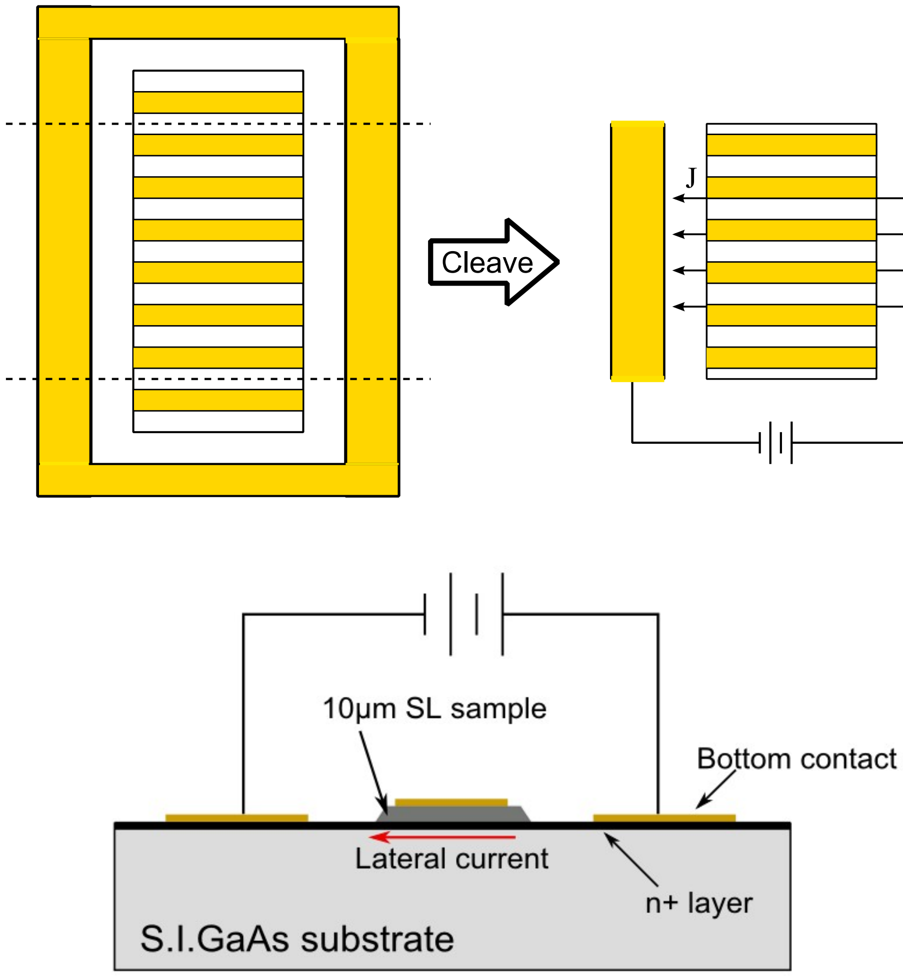

Figure 3.45: The lateral current measurement configuration. a) Device processed for grating coupling. b) Device connection for ridge coupling

The devices are processed as shown in Figure 3.45. The grating device a) was cleaved at both ends and then the bias voltage is applied between two bottom contact sclose to the grating. The current thus flows laterally through the n^{+}-doped GaAs layer beneath the superlattice active region. In this case, no current flows vertically through the super-superlattice structure and therefore no intersubband emission is expected. The radiation emitted by this n^{+}doped GaAs layer is transmitted through the active region and coupled out by the grating. The resistance between the two bottom contacts is low (15 Ω) as expected and the emission spectra is measured at a current value of ~0.9 A, which is acomparable value with the current values of the recorded spectra of the super-superlattice samples. The emission spectra delivered by this lateral current are shown in Figure 3.46. We also investigated the lateral current flowing through the n^+-doped GaAs layer of a ridge waveguide. The device connections are shown in Figure 3.45 b): two bottom contacts of the semi-insulating surface plasmon ridge waveguide are connected and biased. The contact resistance of such device is also low (6 Ω), and the emission spectra were recorded at 1 A and 1.5 A and are reported on Figure 3.47.

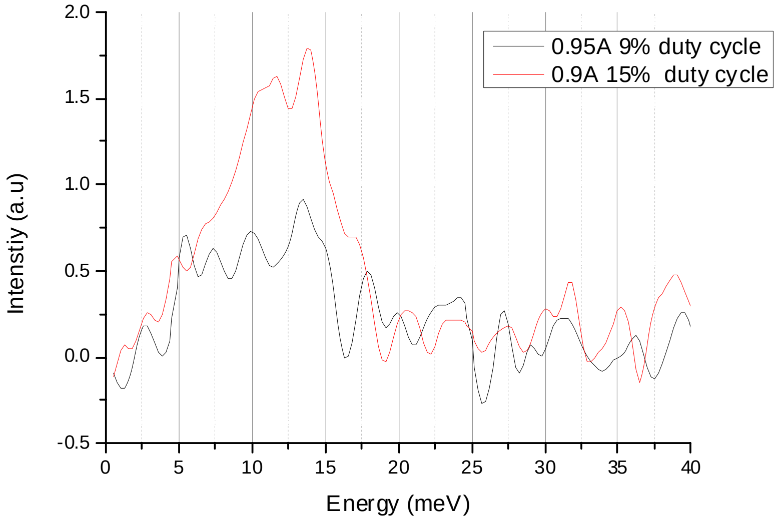

Figure 3.46: lateral current emission from grating device.

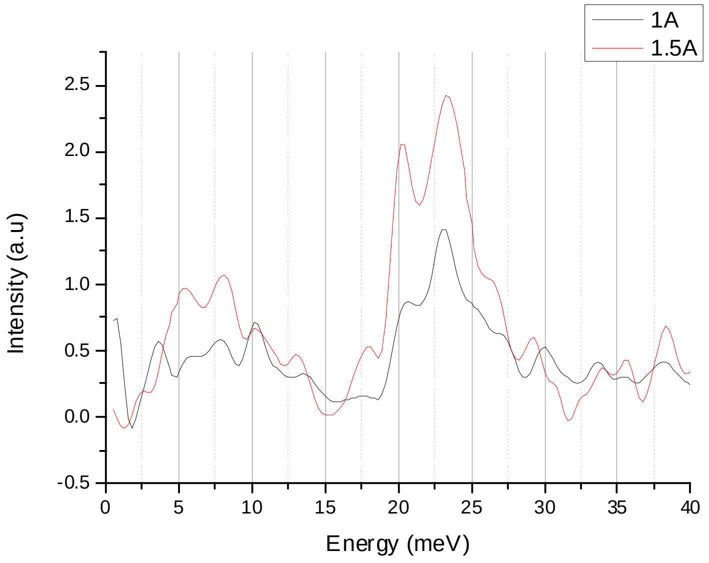

Figure 3.47: Emission spectra from the lateral current of the ridge device

The emission from the lateral current of the ridge waveguide show two main peaks centered at ~8 meV and ~22 meV. In return, only one emission peak is observed in the emission spectra of the grating device, which is centered at ~10 meV. The difference between the two devices is that the grating device only couples TM polarized emission, while the ridge waveguide couples both TM and TE polarized emissions. So the high-energy peak observed in the spectra of the ridge waveguide at 22 meV is identified as TE polarized and the lower energy peak around 9 meV may be the hybrid TE and TM polarized emission.

To identify the origin of these doped layer emission, we first suggest it is thermal emission. As the thermal emission has no dependence on polarization, it can be TE or TM polarized. And it is used to explain the electroluminescence at around 10 meV. As plotted in Figure 3.48 is the blackbody emission for three different temperatures. Since the sample temperature is higher than the hint temperature, three higher temperatures blackbody emission is plotted. For sample temperature between 30 K and 50 K, the blackbody emission peak lies between 7 meV to 12 meV, which overlaps with the measured emission range. The measured emission intensity increase with current and duty cycle, which can be explained that the increased current or duty cycle increase the sample temperature and then increase the thermal emission intensity. Whereas the thermal emission peak also increase with increasing temperature, which is not observed in the measurement.

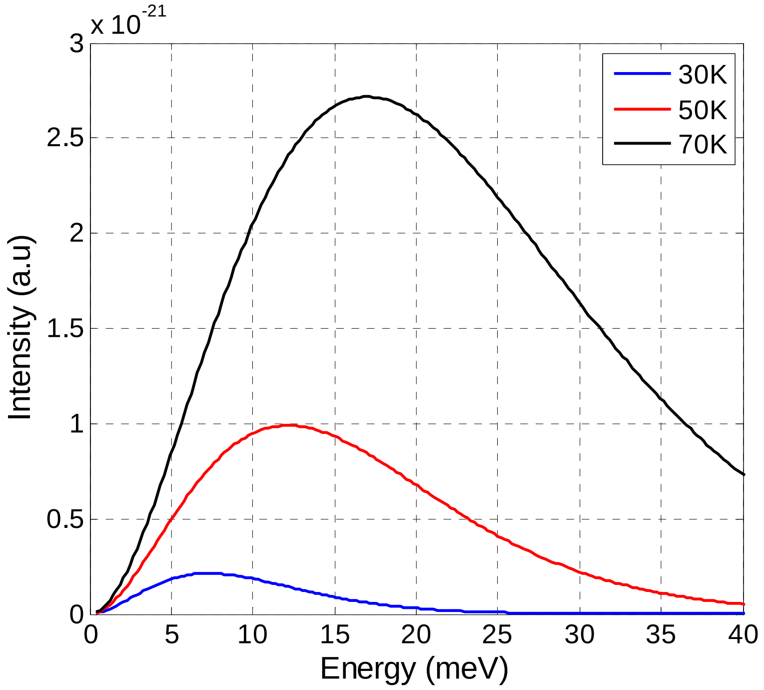

Figure 3.48: black body emission spectra for temperatures of 30K, 50K and 70K.

Another mechanism that can explain the measured electroluminescence at about 10 meV is the donor impurity emission. Since doped layer is about 600 nm thick with Si doped density of 2×10^{18}cm^{-3}, which is possible that the impurity levels will contribute to the emission. Figure 3.49 illustrates electroluminescence measured with FTIR from Si doped $Al_{0.3}Ga_{0.7}As$/GaAs superlattice and the corresponding energy level profile[65]. The measured electroluminescence from 2p$_{xy}$-1s, 1-1s, 2p$_z$-2s, as well as 2-1 transitions shows the luminescence peak of 6.3 meV, 10 meV, 12.4 meV and 14.9 meV. These impurity electroluminescence spectra range overlaps with what we measured in the lateral current emission at around 10 meV, which indicates that impurity emission may contribution to our experimental result.

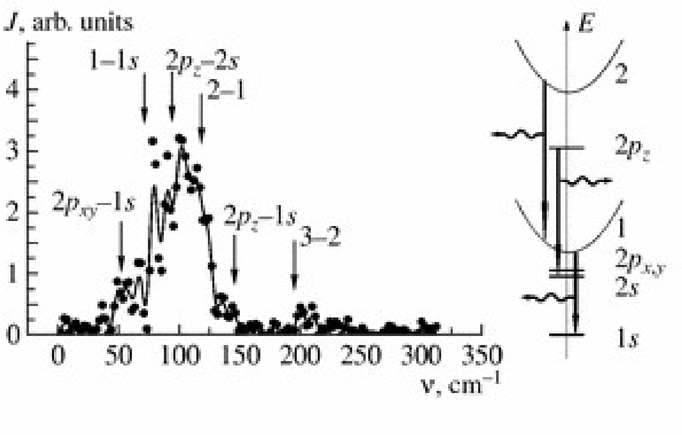

Figure 3.49: electroluminescence measured from Si doped superlattice and the schematic diagram of energy levels and possible optical transitions. Taken from reference.[65]

In addition to the devices based on lateral current, the emission spectra of the other three devices based on vertical current for L527 are also sketched in Figure 3.50: the semi-insulating subwavelength-grating surface emitting device, the double-metal subwavelength-grating surface emitting device and the semi-insulating surface plasmon ridge waveguide. To ensure a relative comparable intensity, the duty cycles of the electrical AC voltage pulses for all the devices are normalized to 10%.

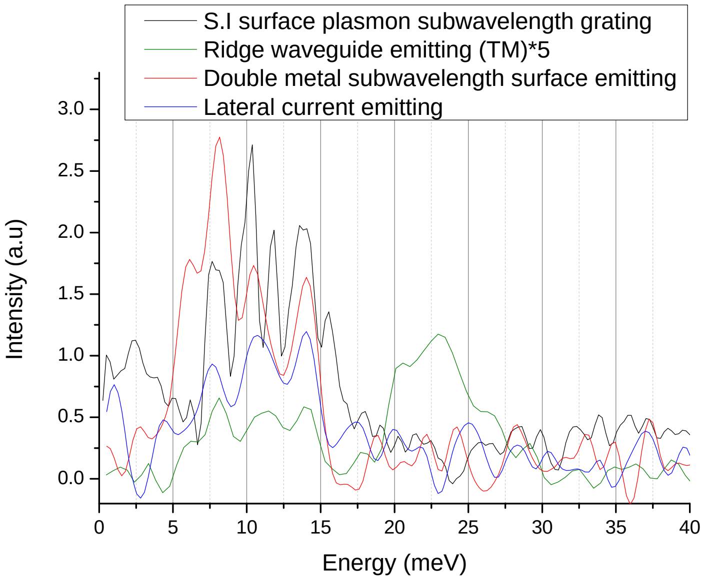

Figure 3.50: Emission spectra provided by the lateral current through the bottom n+doped GaAs layer compared to the emission spectra in a regime of vertical current through the super-superlattice structures.

We clearly see the broad peak centered at ~10 meV in the emission spectra of all the five devices. As discussed earlier in the lateral current part, this broad band emission range can be explained by black body emission or impurity emission. There may exist the Bloch emission, but these unwanted signal screen small Bloch emission signals in this frequency range, which in turn prevents the observation of the Bloch resonance peak shift with the increase of the bias.

To overcome this problem, we further plan to develop new Bloch devices operating at high frequency, in order that the Bloch frequency correspond to energies ranging from 12 meV (3THz) to 24 meV (6THz). In this frequency region, even though the lateral current provides emission, the emission is TE polarized. Using grating coupling configuration, there will be no contribution of the lateral current emission in the frequency range of interest. Moreover, this frequency range is 12 meV lower than the LO phonon resonance in GaAs material, making sure that the LO phonon scattering will not take the main contribution for the electron transport.

3.5.3 Bloch oscillation gain measurement

The recent developments of gain measurement technique in THz QCL provide more sensitive detection enabling to probe the absorption and the gain dynamics inside the active region of the laser. We carried out absorption measurements on the super-superlattice devices we have developed with the aim to observe Bloch gain. The measurements were carried out at ENS Paris in collaboration with S. Dhillon and J. Tignon, using the set-up and the method described in part 3.4.2. In such this experiment, one of the key steps is to couple the THz pulses into and out of the super-superlattice devices. Semi-insulating surface plasmon structure has the advantage of a larger mode extension compared to double surface plasmon structures and hence has the advantage for efficient THz coupling in and out. Consequently, all the super-sperlattice samples used for absorption measurements were processed into semi-insulating surface plasmon ridge waveguides.

L358

The L358 ridge waveguide used for the absorption spectrum measurement is 45 µm large and 1 mm long. Figure 3.51a) shows the THz pulses transmitted through the L358 sample without bias voltage and with a bias voltage of 14 V. Figure 3.51b) shows the corresponding amplitude spectra obtained by Fourier transform. As we can see from these figures, small differences are observed in both time domain and frequency domain between signals without and with bias voltage. Around1.1 THz, the amplitude of the spectrum measured when the device is biased at 14 V is lower than the spectrum measured when the device is not biased (0 V), indicating an increase of the absorption loss in this frequency range when voltage is applied. In addition, at2 THz, the amplitude of the spectrum measured when the device is biased at 14 V is higher than the spectrum measured when the device is not biased (0 V). This increase of the transmitted signal when a voltage is applied to the device indicates at least a reduction of the absorption loss. The 0 V signal serves as the reference $R(\omega)$ and $R(t)$, as will be used latter.

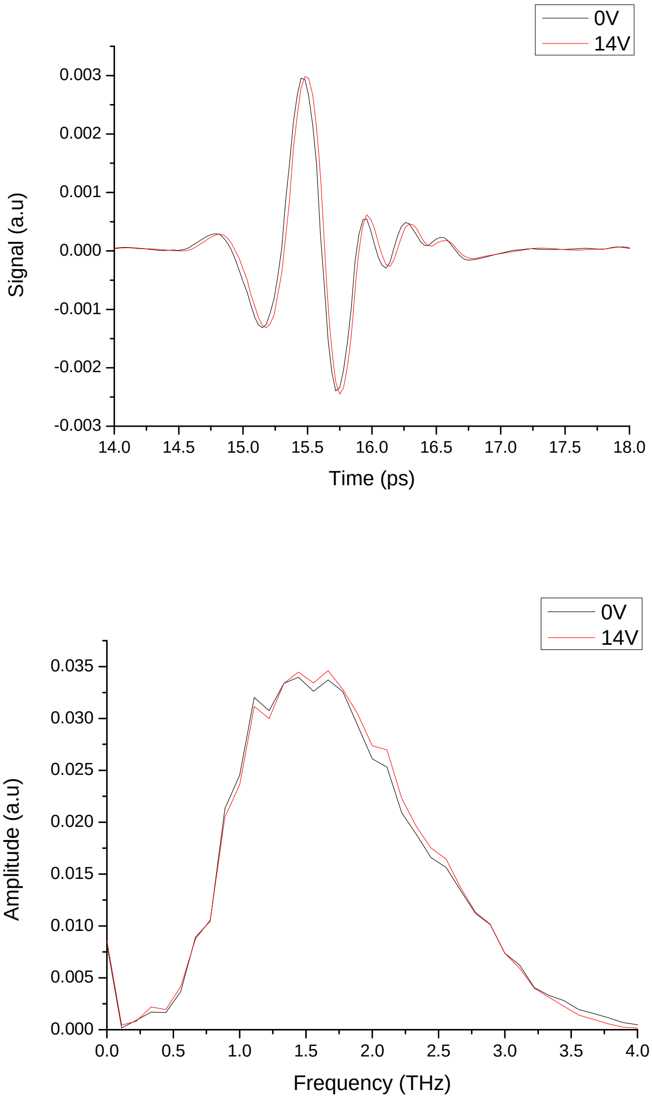

Figure 3.51: a) THz pulses transmitted through the L358 sample without bias voltage and with a bias voltage of 14 V. b) the corresponding amplitude spectra obtained by Fourier

transform.

In a second stage, we applied on the antenna a voltage modulated at a frequency of 50 kHz and 50% duty cycle, and on the device a voltage modulated at a frequency of 25 kHz and 25% duty cycle; the latter was also used as the reference signal for the lock-in amplifier. The differential signals $Diff(t)$ were measured as indicated in part 3.4.2 for different bias voltages. Note that from the I-V characteristic of the L358 sample, we have seen that the minimum of the differential conductance occurs at 11 V. Figure 3.52 a) shows the differential transient for different applied voltages ranging from 4 V to 18 V. We clearly observe a continuous shift of the transient to longer delays as the applied voltage increases. We also observe that the amplitude of the differential signals increases when the applied voltage increases from 4 V to 11V ; at higher applied voltage, the amplitude of the differential signal decreases. The Fourier transform of the time domain signal $Diff(\omega)$ is reported in Figure 3.52 b).

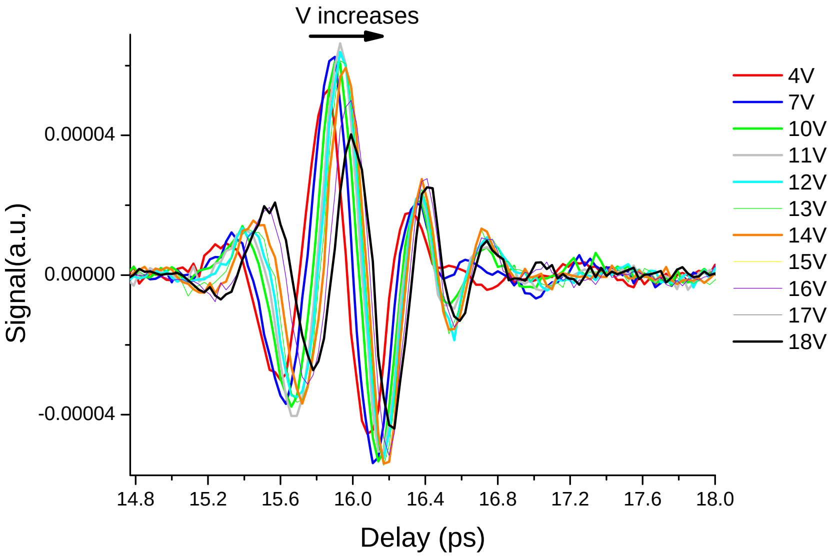

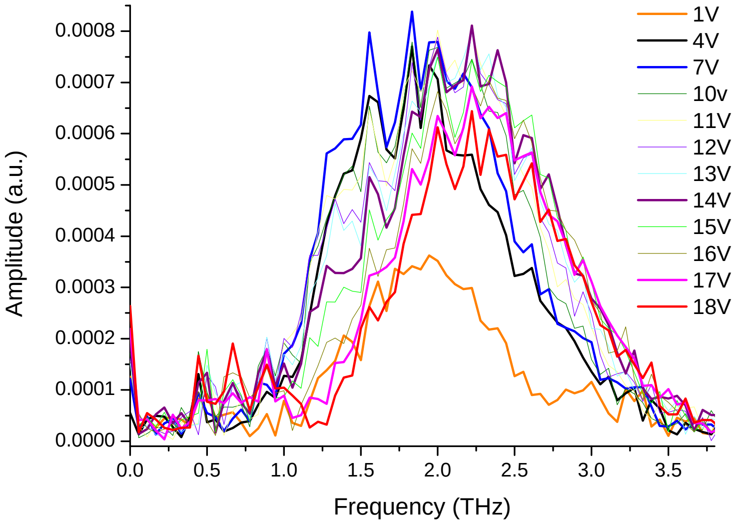

Figure 3.52: a) Differential transients for different applied voltages ranging from 4 V to 18 V. b) The corresponding spectra obtained by Fourier transform.

From these measurements, we have calculated the absorption spectra of the L358 sample according to the equation 3.21, as shown in Figure 3.53. To determine the sign of the absorption, we consider the results reported in Figure 1 which showed an increase of the loss around 1.1 THz when the applied voltage is 14 V. As seen from the absorption spectra, at frequency lower than 1.3 THz, the loss are increased as the applied voltage increases whereas at frequency around 2.4 THz, the absorption becomes negative and gain is obtained when a voltage is applied to the device. The frequency at which occurs the crossover from loss to gain decreases as the applied voltage increases. This behavior is opposite to the one we expect if this gain was related to Bloch gain. Indeed, the Bloch frequency is proportional to the effective electric field applied to the superlattice, and absorption (gain) is expected at frequencies lower (higher) than the Bloch frequency. The frequency at which occurs the crossover from Bloch loss to Bloch gain increases with the increase of the applied voltage, which is not the case with the L358 sample. Note that the values of gain reported in Figure 3 are very low. For 1 V to 7 V, the gain persists up to 3.5 THz. At higher voltages, the gain begins to decrease at high frequencies, and the frequency at which occurs the gain to loss crossover decreases with the increase of the bias voltage. Since the loss and the gain measured here cannot be easily related to Bloch mechanism, the question that arises is their origin. We suggest that the loss and the gain can result from the involving of the injector. Indeed, the injector includes four doped quantum wells, so transitions can occur from low electron levels of the quantum wells to some excited states or to WSLs providing loss and gain. The applied voltage modifies the energies of such transitions. Figure 4 depicts the conduction energy band profile at an applied electric field of 7 kV/cm a) and 10 kV/cm b), enlarged at the injector region. As discussed previously, applied voltages of 7 V and 10 V correspond approximately to electric fields of 7 kV/cm and 10 kV/cm. As pointed out in Figure 4 a), the energy differences between the four lower electron levels in the injector are 3.5 meV and 7.5 meV for an applied electric field of 7 kV/cm, corresponding to frequencies of 0.875 THz and 1.875 THz. Taking into account that the scattering induced energy level broadening, such frequencies may explain the absorption observed in the frequency range from 0.66THz to 1.75 THz. For an applied electric field of 10 kV/cm, the energy differences between the four lower electron levels in the injector are shifted to 4.6 meV (1.1 THz), 5.9 meV (1.44 THz) and 6 meV (1.46 THz). These values are consistent with the observation of an absorption from0.7 THz to 1.64 THz and thus with the decrease of the frequency at which the loss to gain crossover occurs compared to the one measured at 7 kV/cm. For an applied electric field higher than 12 kV/cm, the electron wavefunctions in the superlattice region can overlap with the wavefunctions of the excited states in the injector. Consequently, the electrons can tunnel from the WSLs to excited states in the injector and transitions from excited states of the injector are allowed, inducing absorption. Figure 5 displays the conduction energy band profile for an applied electric field of 13 kV/cm, the arrows indicate the possible electron transitions from excited states of injector to higher excited states or to the continuum band at the energies of 11meV(2.68THz) and 12 meV (2.93 THz). These transitions can explain the absorption observed at higher frequency, around 3 THz, in the measurements.

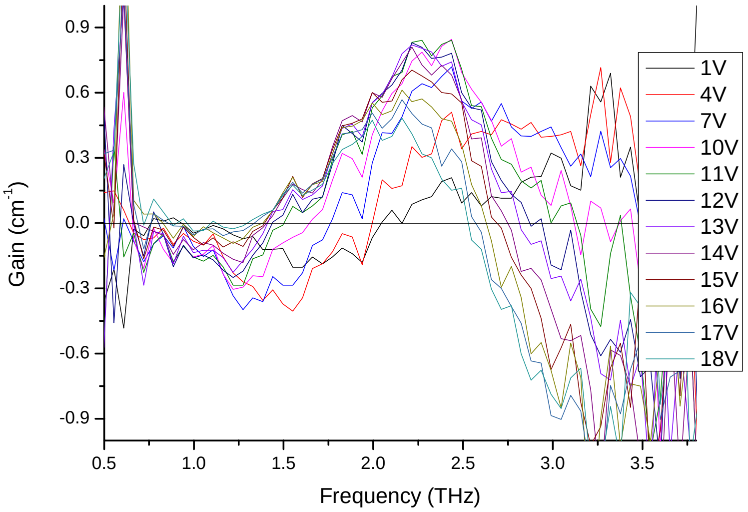

Figure 3.53: Absorption spectra for the L358 sample at 20 K at different voltages ranging from 1 V to 18 V.

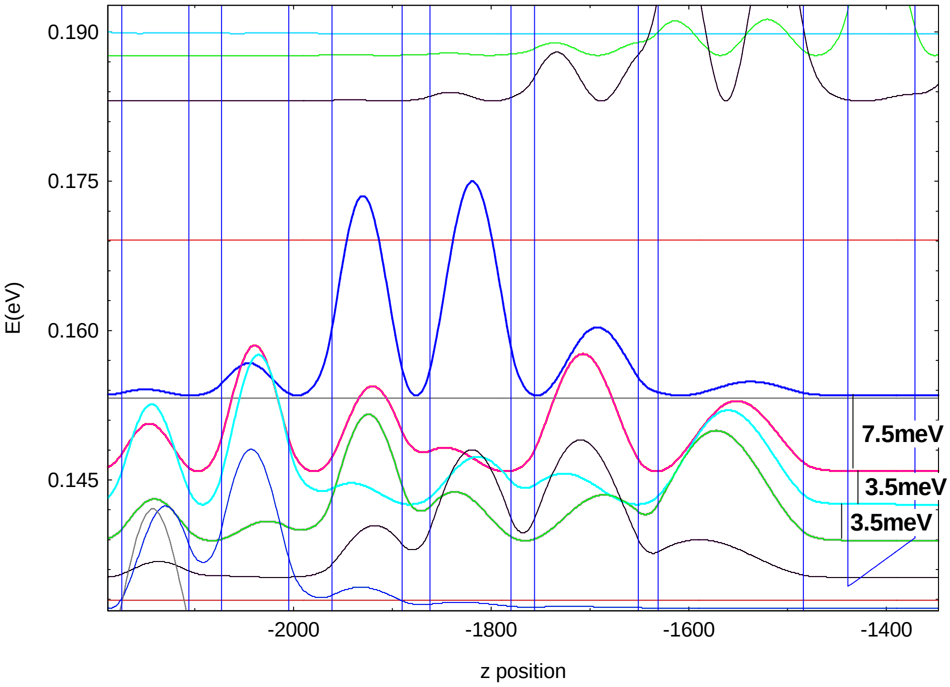

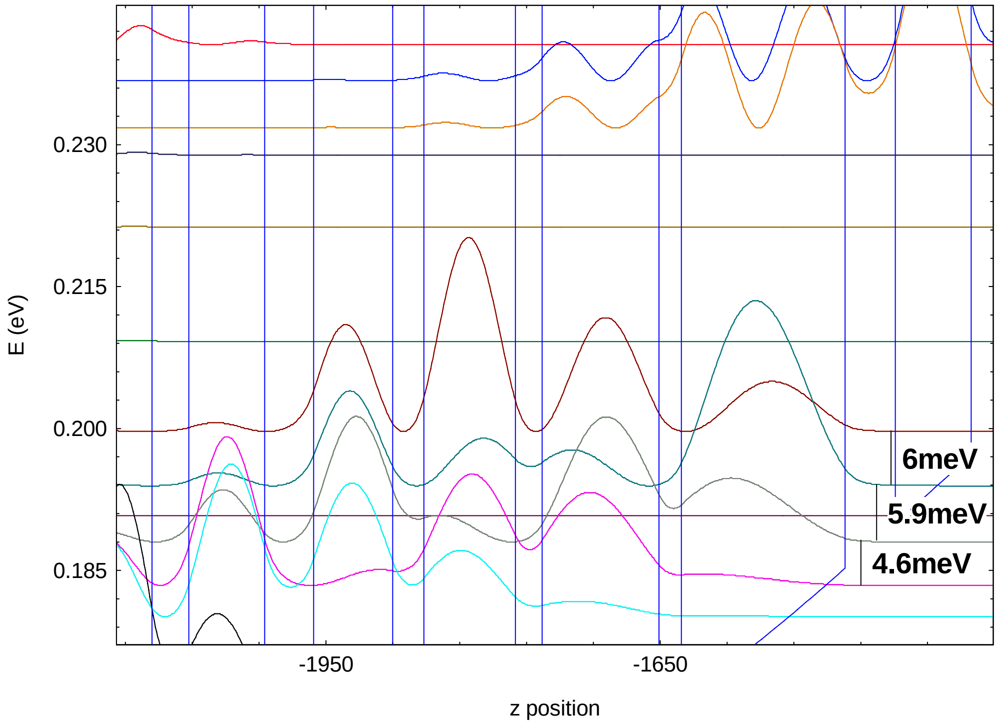

Figure 3.54: Conduction band profile of sample L358 with bias of a) 7 kV/cm and b) 10 kV/cm. The possible electron absorptions transitions in the injector region are indicated with transition energy.

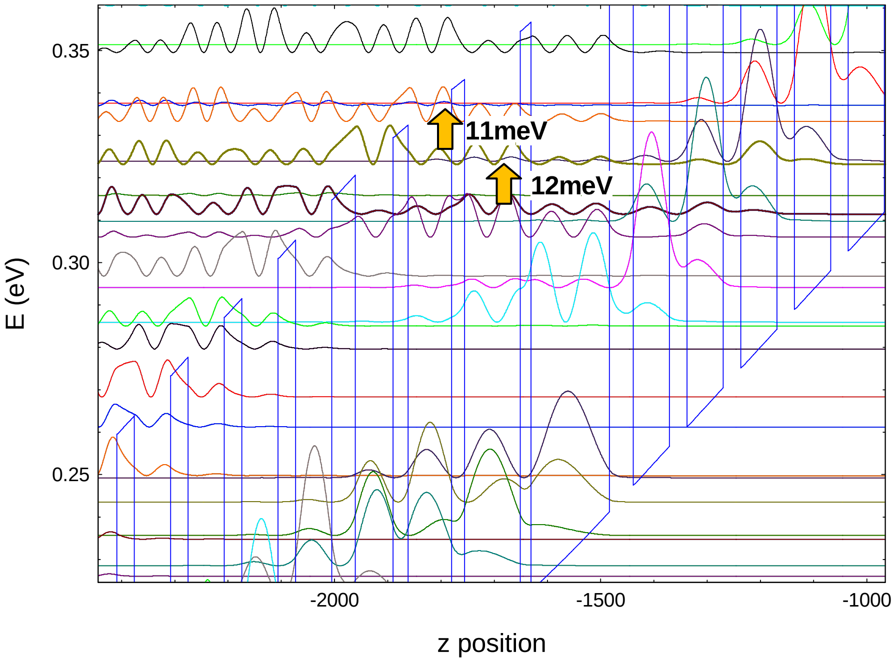

Figure 3.55 : Conduction band profile of sample L358 with bias of 13 kV/cm. The possible

electron absorptions transitions induced by the tunneling are indicated by the arrows with transition energy.

In summary, the absorption spectra of L358samplemeasured for different applied electric fields show very weak gain and absorption. Moreover, the measured absorption and gain cannot be related to Bloch gain. Through detailed analysis of the energy conduction band profile and the absorption spectra, it is found that absorption may originate from unwanted electron transitions from the energy levels of the injector. To reduce the influence of the injector in this measurement, we designed new series of sample (series 2) with only three wells in the injector and with lower energy differences between the first electron levels: L527 and L665.

L527

Figure 6 shows the absorption spectra at different applied voltages for L527 sample. At frequency around 1.5 THz, the absorption is independent of the applied voltage. This contribution in the absorption may come from waveguide loss or n doped layers, and thus is not relevant for our study. When voltages of 5 V and 7.5 V are applied to the device, gain is observed from 2 THz up to 4.3 THz and its magnitude is constant. At higher voltages, the gain amplitude decreases with the increase of the voltage and the frequency at which occurs the crossover from gain to loss decreases from 4.3 THz to 3.3 THz. Such evolution of the gain to loss crossover frequency is opposite to the one expected for the Bloch effect. Moreover, since in L527 sample, the energy differences between the lower electron levels in the injector are less 1.3 THz , the origin of the absorption and the gain cannot be attributed to unwanted transitions in the injector. We suggest that the observed absorption and gain are originated from the electron transitions between resonant and localized impurity states and to the electron transitions involving the subband states since the quantum wells in the injector region are Si doped with the sheet density of 6.465×10^{10} cm^{-2}. From reference[65], the transition *2pz-2s* in GaAs/AlGaAs quantum wells structures doped with Si is located at 3.3 THz; this value correspond approximately to the spectral position of the gain peak. This contribution of the impurity may come from the doped quantum wells of the injector and by the n^{+}-doped GaAs layer beneath the super-superlattice active layer. To minimize the impurity contribution to absorption and gain we have designed the L665 sample, in which the only barriers of the injector are doped and no more the quantum wells.

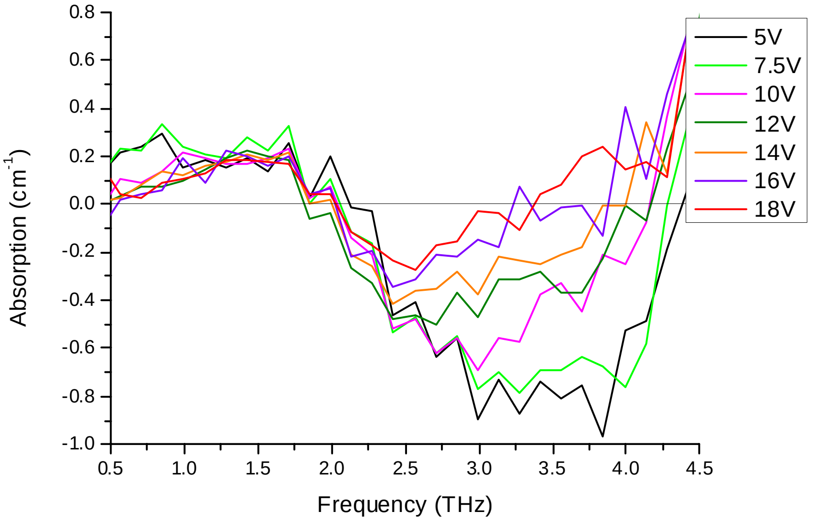

Figure 3.56: Absorption spectra of the L527 sample at 10 K at different applied voltage ranging from 5 V to 18 V.

L665

Figure 7 depicts the measured absorption spectra for the L665sample. At frequency below 2 THz, the absorption still exists. Between 2 THz and 3.5 THz, the gain is still observed and at higher frequency, the absorption appears.

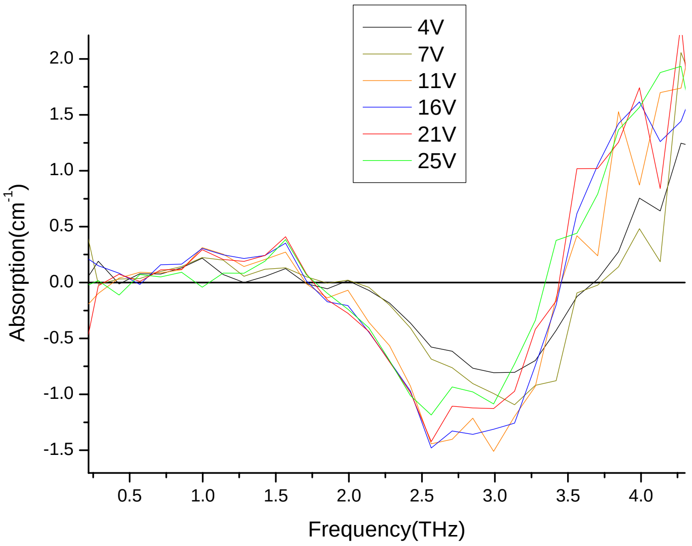

Figure 3.57: Absorption spectra of the L665 sample at 10 K at different applied voltage ranging from 4 V to 25 V.

We observed that the gain peak decreases from 3.2 THz to 2.6 THz as the applied voltage increases from 4 V to 25 V, that the magnitude of the gain increases with the increase of the voltage from 4 V to 11 V and remains relatively constant beyond 11 V at a typical value of 1.3 cm^{-1}. As in the L527 sample, the frequency at which occurs the crossover from gain to absorption decreases as the applied voltage is increased, indicating that this gain and absorption features cannot be related to Bloch effects. The similarity between the absorption spectra of the L527 sample and the L665 sample let us believe that the contribution of the electron transitions between resonant and localized impurity states and to the electron transitions involving the subband states still happens, and probably in the n^+-doped GaAs layer of 600 nm thick beneath the super-superlattice active layer

3.6 Conclusion and perspective

In this chapter, we have designed, fabricated as well as tested cascade super-superlattice structure devices based on AlGaAs/GaAs superlattice system. The cascade super-superlattice strucuture was designed based on resonance LO phonon injector scheme, where the thin elementary superlattices are imbedded with resonant LO phonon injector to simultaneously preserve the Bloch gain and suppress the electrical domain formation. The samples were processed into semi-insulating surface plasmon waveguide edge emitting device, semi-insulating subwavelength-grating surface emitting device, and double mental subwavelength-grating surface emitting device for experimental measurement. The electroluminescence at around 10 meV (2.4 THz) was observed for all the devices, however, the center frequency of the electroluminescence spectra is not sensitive to the applied voltage, which is not expected in theory. Further investigation of black body emission and lateral current electromagnetic emission from n+doped bulk GaAs present the same electroluminescence spectra, indicating that what we have observed may originate from black body emission or impurity energy level transition. The absorption/gain of semi-insulating surface plasmon waveguide devices was measured using THz TDS to explore the Bloch gain. The gain to loss crossover was obtained at around 3 THz for all the test devices, and the frequency where the gain to loss crossover occurs shifts to lower frequency with increasing electric field, which is opposite to the theory prediction. Considering the measurement results are not sensitive to the sample design, it is indicated that the electron transitions between resonant and localized impurity states and to the electron transitions involving the subband states contribute to the measured result.

To overcome this problem, we further plan to develop new Bloch devices operating at high frequency, ranging from 12 meV (3THz) to 24 meV (6THz). In this frequency region, the Bloch gain is expected to be observed in higher frequency than the resonant transition between impurity states, such that the distortion from impurity can be excluded. Moreover, the frequency range is 12 meV lower than the LO phonon resonance in GaAs material, making sure that the LO phonon scattering will not take the main contribution for the electron transport and a large part of the electrons can still contribute to the Bloch gain.

.

4 Bloch emission time domain spectroscopy

In this chapter, we explore the THz emission of Bloch oscillations in undoped superlattices illuminated by femto-second optical pulses. Firstly, we investigate the Wannier Stark Ladder (WSL) using photocurrent spectroscopy based on FTIR spectrometer. Secondly, the THz emission of Bloch oscillations was detected using THz time domain spectroscopy.

4.1 Exitonic Wannier Stark Ladder

The conduction band profile and the energy states in superlattice biased by a dc electrical field were discussed in paragraph 2.2, where electrons were treated as free carriers with confinement in the growth direction. Equally spaced discrete energy levels called WSL states are formed. In the experiments reported in this chapter, the electrons are not free electrons; they are generated through optical interband transition, which simultaneously generated electron-hole pairs with Coulomb interaction (exciton). The exciton substantially changes the energy states in the conduction band, leading to asymmetry in the excitonic Wannier-Stark ladder and thus to unevenly spaced energy excitonic WSL states.

Dignam and Sipe presented the first calculation of exciton image WSL[66, 67] considering the bound 1s exciton, for which the electron-hole pairs are treated as only confined in the growth direction. Because of the exciton binding energy, the conduction band energy levels of equation 2.12 would be modified as

$$E_n = E_0 + nedF + E_{exci}(n, F) \qquad 4.1$$

where the $\mathrm{E_{exci}(n, F)}$ represents the exciton binding energy at the n$^{\mathrm{th}}$ well under the electric field F. The exciton binding energy varies with different quantum well states, it is larger for negative states while weaker for positive states. The exciton WSL of a $Al_{0.3}Ga_{0.7}As$/GaAs superlattice with 6.7 nm thick well and 1.7 nm thick barrier shown in Figure 4.1 was calculated by Dignam and Sipe. The energy axis is relative to the GaAs band edge. The diameters of the circles correspond to the oscillator strength of the transitions. It can be seen that the negative WSLs are much closer to the center transition and preserve stronger oscillator strength comparing with their positive counterpart WSLs.

The Dignam and Sipe model only included the 1s bound state, the continuum state which represents the in plane motion of exciton was neglected. Whittaker[68] first developed a full exciton model with both 1s exciton and continuum states included. Figure 4.2 illustrates the absorption spectrum calculated with 1s exciton included but without exciton continuum states included (left) and with exciton continuum included (right). 1s exciton calculation shows only discrete WSL absorption peaks, while for the absorption with the exciton continuum states included, the continuum absorption edge is clearly visible beside the 1s exciton levels. Another different interesting feature is that the absorption peak is asymmetric in exciton absorption calculated with continuum, as can been seen for +1, 0 , -1 absorption peaks, and the asymmetric is stronger for +1 absorption and less stronger for 0, -1 absorption peak. This phenomenon is interpreted as the quantum interference between different absorption paths for transition to: 1) the discreet 1s level and 2) the continuum of the energetically lower state, from the shared ground heavy hole states. This is normally known as the Fano effect and was verified in experiment by Holfeld[69] in superlattice.

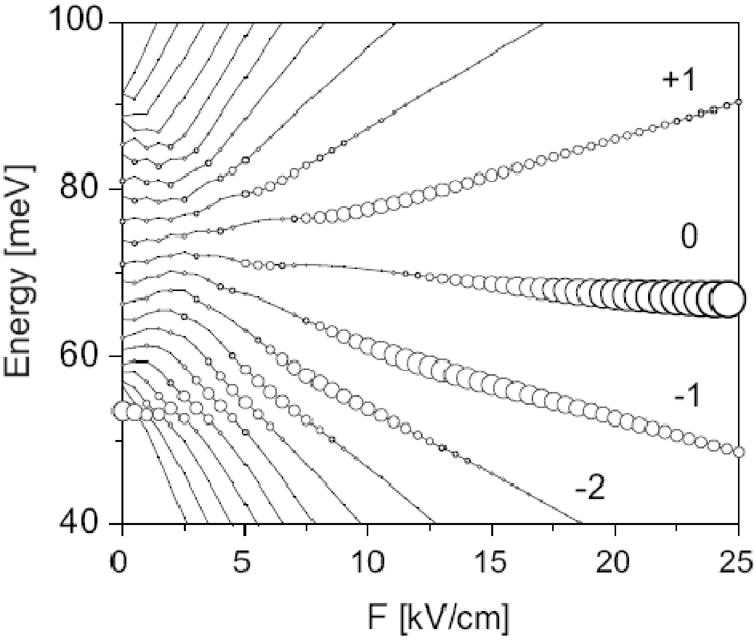

Figure 4.1: Calculated exciton fan chart of 1s heavy-hole excitons. The energy axis is given relative to the GaAs band edge. The diameters of the circles correspond to the oscillator strength of the transitions. Taken from reference[33]

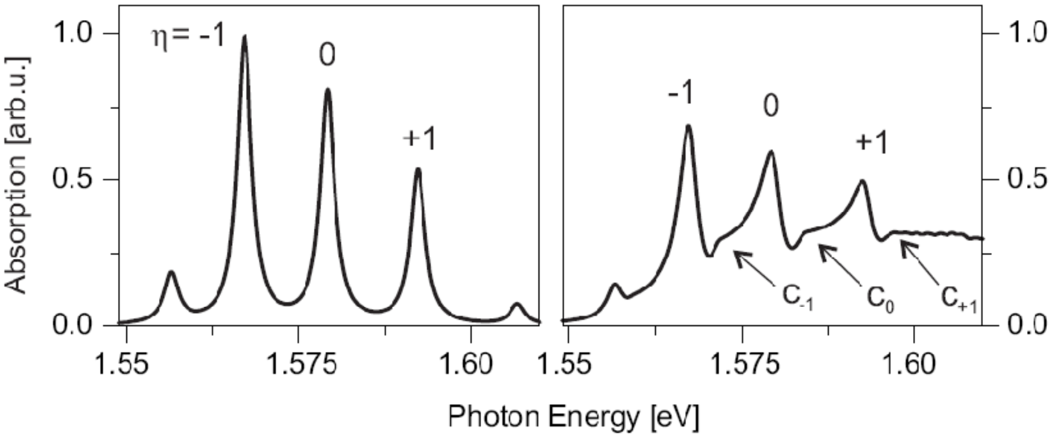

Figure 4.2: Theoretical heavy-hole exciton absorption for F=15 kV/cm from Reference[70]. Left: Without exciton continuum states. Right: With exciton continuum included: the continuum edges are marked by c_n.

4.2 Sample description

The samples used for optical investigation of Bloch oscillations were undoped $Al_xGa_{1-x}As/GaAs$ semiconductor superlattice. The sample information is summarized in table 4.1. Sample 9AQ13 and B9R231 were grown by J.C.Harman in Laboratoire Photonique et Nanostructures (LPN). V1764 was provided by Kaz Hirakawa in Tokyo University.

Parameters	9AQ13	B9R231	V1764
a	9.7 nm	6.8 nm	8.49 nm
b	1.7 nm	1.2 nm	0.56 nm
d=a+b	11.4 nm	8 nm	9.05 nm
x	33%	33%	100%
Δ	18 meV	52 meV	35 meV

Table 4.1 Parameters of the semiconductor superlattice samples used for the optical investigation of Bloch oscillations, where a is the well width, b the barrier width and x_{Al} the Aluminium mode fraction. The miniband width is represented by Δ.

9AQ13 sample was grown on heavily n^+-doped GaAs substrate, it has 40 periods of superlattice unit cells and there are 50 nm $Al_{0.33}Ga_{0.67}As$ buffer layers on the both sides of the superlattice region. The width of the first miniband is 18 meV and the first minigap is 55 meV. B9R231 has 130 periods of superlattice unit cells, and there is a 300 nm thick $Al_{0.33}Ga_{0.67}As$

buffer layer beneath the superlattice region and a 200 nm-thick $Al_{0.33}Ga_{0.67}As$ layer on top. The width of the first miniband is 52 meV and the width of the first minigap is 63 meV. While for V1764, the superlattice barrier is AlAs, the width of the first miniband is 35 meV and the first minigap is 80 meV.

Using traditional optical lithography technique, as described earlier, the samples were wet etched to form circular mesas, see Figure 4.3. The mesa diameters are 600 μm. The mesa thicknesses are 556 nm, 1540 nm and 500 nm for 9AQ13, B9R231 and V1764 respectively. On top of the mesa, Ti/Au (10 nm/200 nm) was first deposited to form the ring circle and, inside the ring a Cr/Au (1 nm/5 nm) semitransparent layer is deposited. The semitransparent layer works as a Schottky top contact whilst enabling light transmission. The bottom contact of the device was deposited near the mesa on the n-doped GaAs substrate using Ti/Au/Ti/Ge/Au metals and annealing to provide ohmic contact. The electric field bias was achieved by connecting the bottom and the top contacts to a dc voltage source (Agilent E3647A power supply), which can provide up to 35 V dc bias.

For all the measurements, the samples were mounted in the liquid He flowing cryostat to set cryogenic temperature. The cryostat series is XE-102-6E3, the input and output windows are made of 3 mm thick quartz, enabling both near infrared and THz transmission.

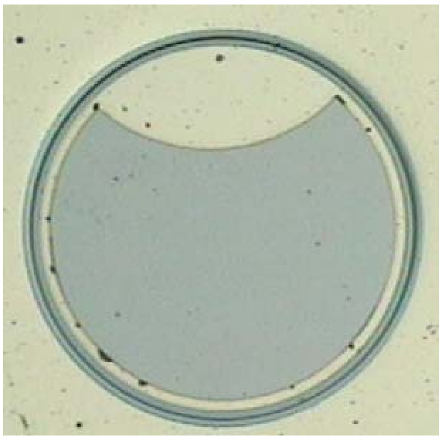

Figure 4.3: Image of the processed mesa structure for optically

4.3 WSL photocurrent spectroscopy investigated by FTIR

The WSL was first predicted in theory by Wannier in 1960. Since then, there has been long controversial of whether the WSL states or even Bloch oscillations really exists[71]. The argument was rather in theory before high quality superlattice can be grown. With the development of MBE technique, high quality superlattice was no longer obstacle for superlattice in later 1980s. In 1988, Mendez, Agullo-Rueda and Hong[12] announced their experiments of the first observation of Stark localization in semiconductor superlattice through photoluminescence and photocurrent experiments. Almost at the same time P. Voisin et al.[72] also observed the WSL states using electro-reflectance experiment.

Here, we exploit Fourier transform photocurrent spectroscopy experiments to investigate the WSL of the undoped superlattice samples. The configuration of the measurement is similar to the FTIR spectroscopy setup used to measure the electroluminescence spectrum in chapter 3. For the electroluminescence spectrum measurement reported chapter 3, the Bloch device was working as the light source, the emitted light transmits through the Michelson interferometer, and the interfered light was detected by the bolometer. Whereas here, the white light from a Tungsten lamp is transmitted through the Michelson interferometer and illuminates the superlattice device. The generated photocurrent is recorded using current preamplifier as the photocurrent interferogram, from which the Fourier transform provides the photocurrent spectrum. The experimental configuration is show in Figure 4.4.

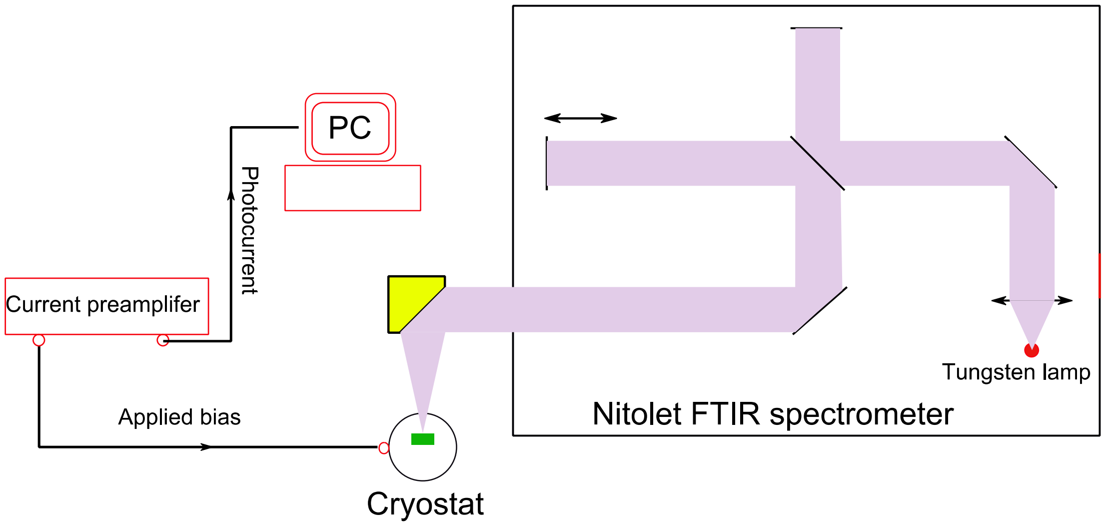

Figure 4.4: Photocurrent spectroscopy setup based on FTIR spectrometer.

The FTIR spectroscopy system is a Nicolet FTIR with a Tungsten lamp inside used as the white light source, providing continuous emission from visible to near infrared. A quartz beam splitter is placed in the Michelson interferometer. After the interferometer, the white light is guided and focused on the superlattice sample. A dc voltage is applied to the superlattice sample and the photocurrent is coupled to a current preamplifier connected to a computer.

In contrast to the electroluminescence measurements discussed previously, the Nicolet FTIR spectrometer works in the rapid scan mode for this photocurrent spectra measurement. The translating mirror moves continuously without pause, the photocurrent is recorded continuously during the moving and gives the interferogram. The interferogram was then processed by Fourier transform to generate photocurrent spectrum.

Figure 4.5 shows the photocurrent spectrum at applied voltage of -0.3 V. Figure 4.6 shows the photocurrent recorded at different applied voltages; the photocurrent is offset at the y axis and the lines are added for the guide of the eyes. Combining these two figures, we can identify 5 photocurrent peaks corresponding to heavy hole–electron transitions, which are named hh_{+1}, hh_0, hh_{-1} and hh_{-2}, and one peak for light hole–electron transition, lh_0. Their spectral position shifts with the increase of the bias voltage, leading to the increase of the energy splitting between the adjacent photocurrent peaks, as expected. The photocurrent current was distorted by the Fourier transform at -0.5 V, nevertheless, it did not prevent from identifying the WSL states. Between heavy hole–electron transitions hh_{-1} and hh_0, as well as between hh_0 and lh_0 transition peaks, we observe some small photocurrent tips, which are attributed to the heavy hole-electron 2s transitions. This 2s exciton transitions were also observed by Leisching et al. [73], in a relatively similar superlattice structure. Besides, for the hh_{-1} and hh_0 transitions, the photocurrent clearly shows asymmetric shapes, due to Fano effects as discussed previously.

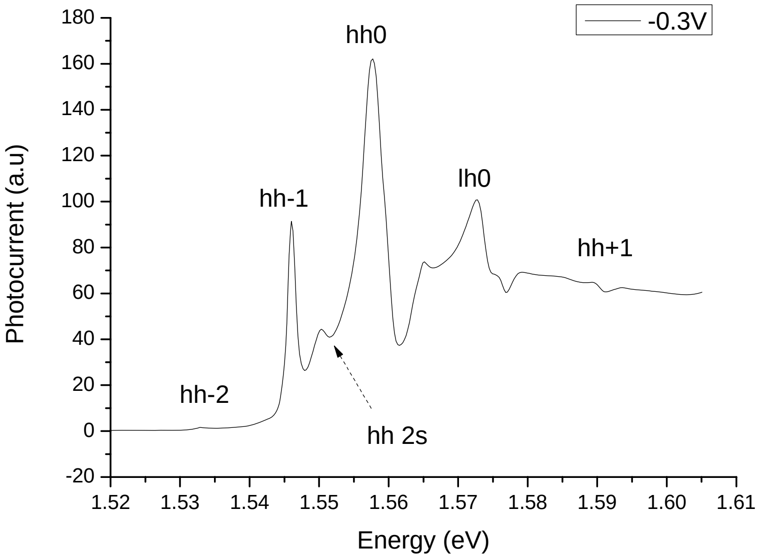

Figure 4.5: Photocurrent spectrum for 9AQ13 sample biased with an electrical field of

8.1 kV/cm at 10 K.

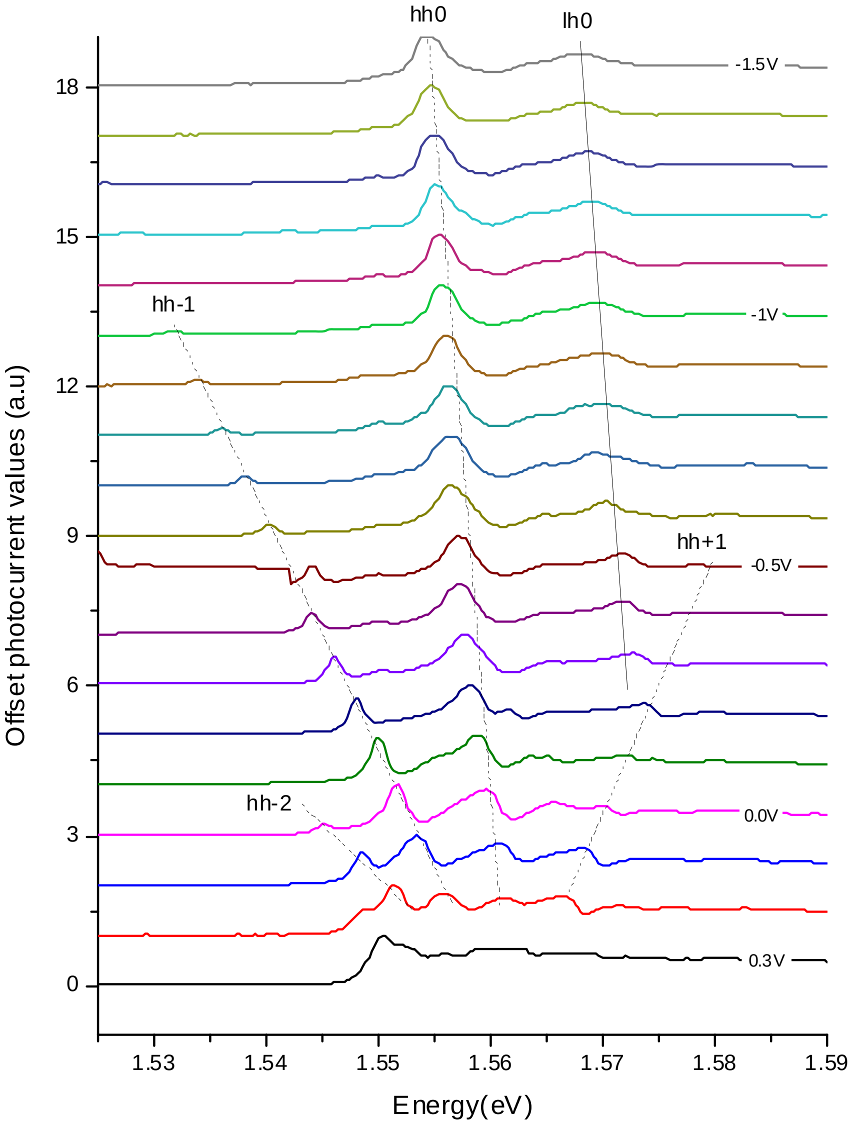

Figure 4.6: Photocurrent spectra of the 9AQ13 sample at 10 K for different applied voltages. The photocurrent spectra are shifted vertically for clarify.

We observe that the internal electric field starts to rise at 0.3 V. This voltage offset was also observed for the doped superlattice device (L358) and is attributed to voltage drop at the Schottky top contact.

In order to determine the effective internal electric field on the superlattice region, we consider the energy splitting between Wannier Stark ladder state, which is proportional to the potential drop in the superlattice region at relatively high bias voltage (since excitonic effect distorts the energy spaces stronger at low voltage). The energy splitting between WSL states can be written as :

$$\Delta E = edF = ed\frac{V_1 - V_0}{D} \qquad 4.2$$

Where V_1 is the applied voltage to the whole device and V_0 is the offset due to the Schottky contact. The energy splitting can be measured directly from the WSL spectrum, which gives (in eV)

$$\Delta E = E_0^1 - E_1^1 \qquad 4.3$$

Where the E_0^1 represents the Stark ladder hh_0 energy at a voltage V_1, and E_1^1 represents the Stark ladder hh_{-1} energy at a voltage V_1. Chosen several applied voltages, we get the mean offset voltage V_0 of 0.32V. Note that this offset voltage can include in addition to the Schottky contact contribution some carrier screening of the electric field inside the superlattice structure. Based on this offset, we are able to calculate the internal electrical field on the superlattice.

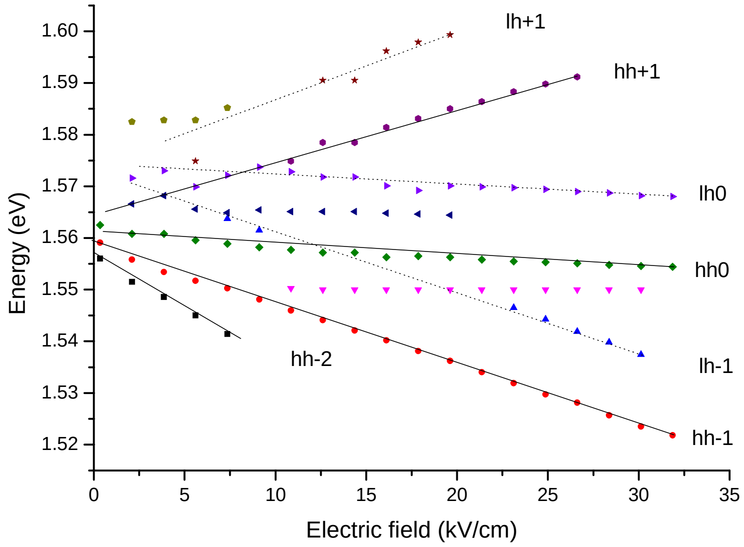

Figure 4.7: Fan chart of the Wannier-Stark ladders as observed in photocurrent spectra of the 9AQ13 sample at 10 K and at low excitation intensity.

The Figure 4.7 shows the fan chart of the WSL as a function of the internal electric field. It is easier to see the WSL evolution with the increase of the applied voltage from the fan chart. The hh_0 transition tends to lower energy with the increase of the internal electric field, which can be explained by the quantum confined Stark effect.

The photocurrent spectroscopy for B9R231 is shown in Fig 4.8, for this sample the offset voltage is -1.5V. Because of the small quantum barrier width of the superlattice comparing to the 9AQ13 sample, the coupling between quantum wells is much stronger, which provides more pronounced WSL. In the Figure 4.8, even the heavy hole-electron transition hh_{-4} photocurrent peak is observed. It can be clearly seen that with the increase of the applied electrical field, the conduction band gradually changes from miniband range to WSL. In contrast with the 9AQ13 sample, the heavy hole-electron 2s transitions are not observed.

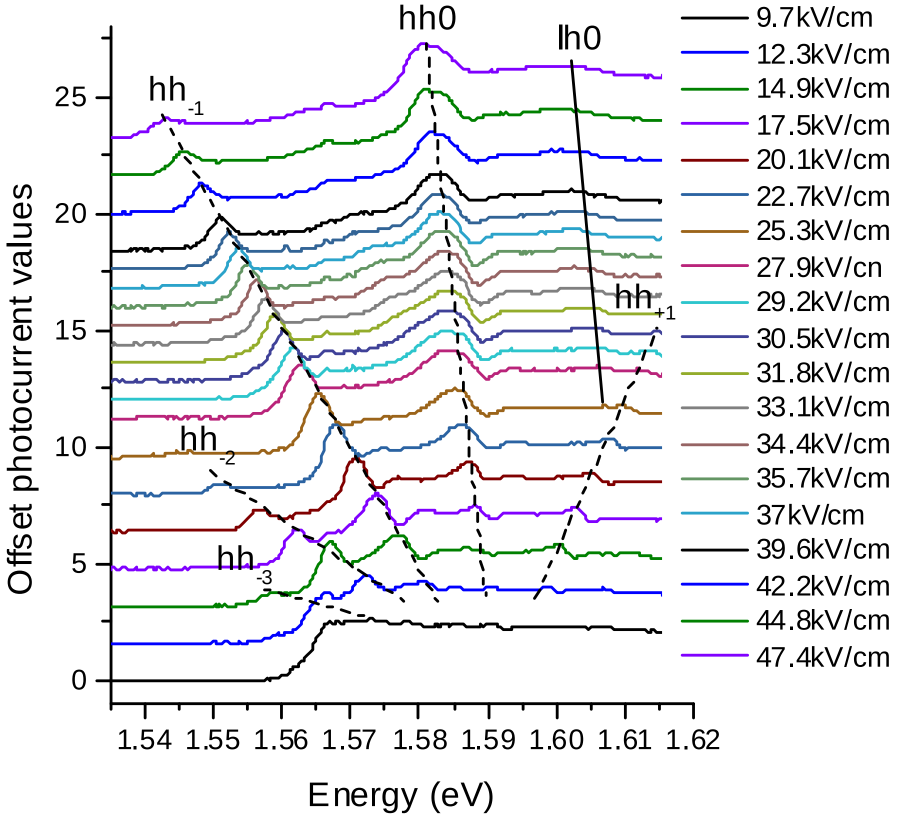

Figure 4.8: Photocurrent spectra of the B9R231 sample at 10 K for different applied voltages. The photocurrent spectra are shifted vertically for clarify.

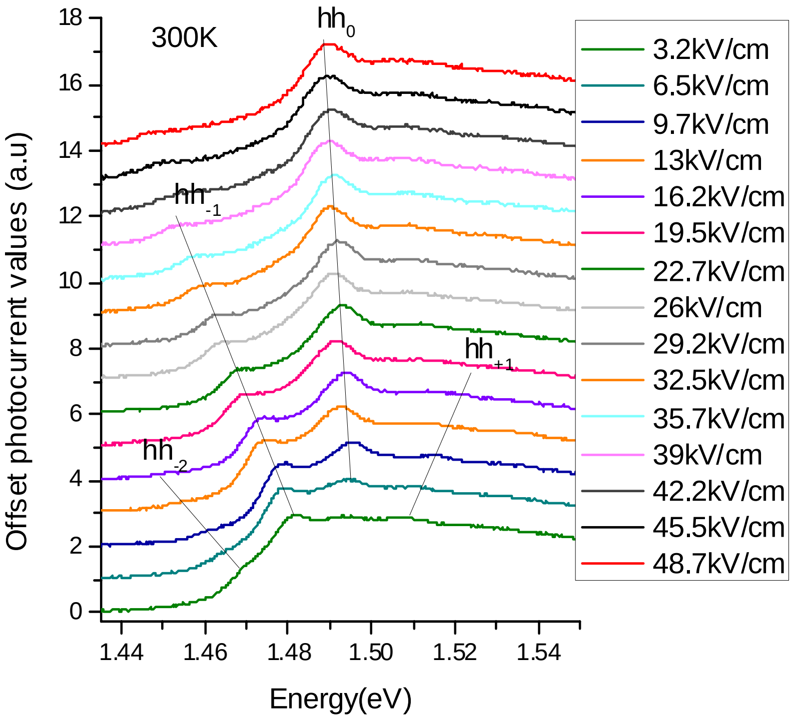

Figure 4.9: Photocurrent spectra of the B9R231 sample at 300 K for different applied voltages. The photocurrent spectra are shifted vertically for clarify.

The photocurrent of the B9R231 sample was also measured at room temperature. The photocurrent spectrum is shown Figure 4.9. At room temperature, the heavy hole-electron transitions hh$_{-2}$ is still resolved with broader resonances. This broadening is attributed to the much faster decoherence time resulting from the rapid ionization of excitons at room temperature since the thermal energy *kT* is much larger than the exciton binding energy. We observe that the offset voltage is smaller at room temperature, as previously observed by Leisching et al.[73] until 200 K. We will discuss this point in the next chapter in detail.

4.4 Experimental setup for time domain THz emission spectroscopy

For optical investigation of Bloch oscillations, broadband optical pulse illuminates biased superlattice samples, and generates electrons simultaneously on neighboring WSL states. The photoexcited electrons preserve the same initial phase, which guarantees the coherence of the electrons. Under an applied electric field, the coherent electrons perform Bloch oscillations, acting as microscopic dipoles $p = ex$ with x, the electron displacement. The superposion of the microscopic dipoles leads to the emission of electromagnetic waves, which lies in THz region. The single microscopic dipole is oriented parallel to the growth direction of the superlattice samples, so the THz radiation is mainly polarized in parallel to the surface superlattice sample. If the illuminated area is comparable or larger than the emission wavelength, the emission is collinearly directed in the forward reflection direction and the backward refraction direction because of the constructive interference of the coherent single dipoles in a large area [33, 74]. The typical radiation geometry is shown in Figure 4.10. The femto-second laser pulses excited the superlattice sample with a tilted angle α and the emitted THz radiation can be detected in the reflection and refraction direction.

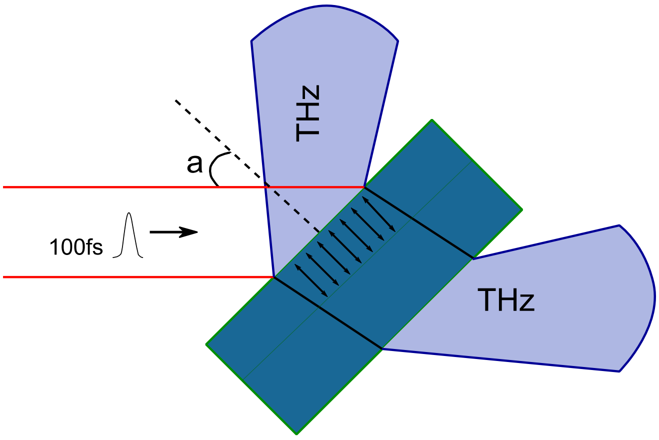

Figure 4.10: Illustration of the excitation geometry in the THz emission experiment. THz transients are emitted from the coherent dipole ensemble into cones collinear with the transmitted and the reflected optical beams.

The detailed of the TDS setup is depicted Figure 4.11. The femto-second laser is a Coherent Mira 900 Kerr-lens mode locked Ti:Sapphire laser system. It delivers Fourier transform-limited optical pulses, with 100 fs pulse width, and 20 meV spectrum width. The center wavelength is tunable from 700 nm to 1000 nm. The laser beam is first splitted by a BK7 beamsplitter into the pump beam and the probe beam. The BK7 beamsplitter is only 6.35 mm thick, preserving a small group velocity dispersion of 20 fs. Using an autocorrelator, I have measured a pump pulse width just before the cryostat window of 123 fs, and the spectrum was monitored by an Agilent 86142B optical spectrum analyzer. The centre photon energy of the pumping laser pulse was selected to be slightly smaller than the centre energy of the hh_0 transition, covering both hh_0 and hh_{-1} WSL transitions. The pump beam is focused by a focusing lens (f=25cm), producing a focusing spot of ~ 600um, approximately of the diameter with the superlattice mesa. A mechanical chopper was installed on the pump beam to provide phase-sensitive detection using a lock-in amplifier for signal processing. The chopping frequency is selected to 2.6 kHz.

The superlattice sample is mounted in a liquid He flowing cryostat, to ensure cryogenic temperature. The out coupling window of the cryostat is a 3 mm-thick quartz window, permitting both THz and infrared beam transparency. The sample is tilted of 45 degree with the respect to the direction of the pump optical beam. The emitted THz radiation is collinear with the reflected pump optical beam, making the infrared beam a good indicator for the alignment of the invisible THz beam.

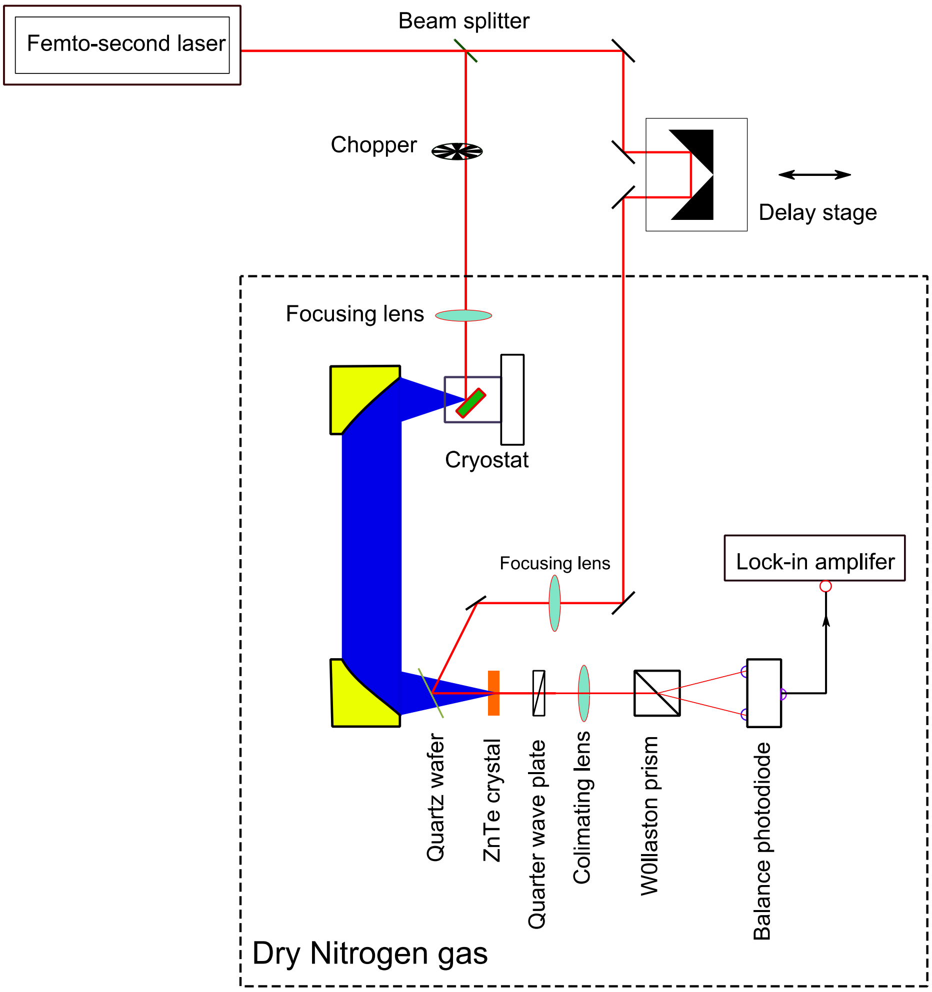

Figure 4.11: Schematic drawing of the experimental set-up.

The THz beam emitted by the superlattice sample was first collected and collimated by a 50 cm diameter, 90 degree, off-axis gold coated parabolic mirror. Since the size of the THz emission spot on the sample was comparable to the emitted wavelength, the THz beam diverges from the sample at a wavelength-dependent divergence angle. Therefore, the parabolic mirror was chosen to have a focal length as small as geometrically possible to ensure that the THz radiation was effectively collected. The collimated THz beam reflected by the mirror in the free space is then focused on an electro-optic crystal (EO crystal) using a second 90 degree, off-axis gold coated parabolic mirror, with 50 cm diameter and 79 cm focus length. Even though the whole THz beam path was enclosed in a box with dry N_2 flowing, water absorption still plays a role in the THz detected signal.

A computer controlled delay stage was installed in the probe beam to vary the path length of the probe beam. This varying of the time delay permitted the mapping out of the THz field in time. The gating probe beam was reflected by a 200 µm thick quartz wafer and focused onto the EO crystal. A gold layer of 7 nm thick was deposited on the quartz wafer to increase the reflectivity coefficient in the infrared range while preserving 50 % of transmission in the THz range. Before the THz emission of Bloch oscillations was carried out, I used the THz emission from $In_{0.53}Ga_{0.47}As$ surface to search for the optimal performances of the setup.

The THz electric field was detected by a free space electro-optic sampling technique. Electro-optic sampling and photoconductive antenna are the most widely used detection techniques for THz TDS setup[75]. These both techniques provide coherent detection with a very high signal to noise ratio. With respect to detection based on photoconductive antenna, the electro-optic sampling technique has the advantage of a very broadand detection range, up to 70 THz[76] and easy implementation. The electro-optic sampling technique exploits the linear electro-optic effect (Pockels effect)[77]. I used ZnTe crystal as the EO crystal ; this crystal is not naturally birefringent. As indicated in Figure 4.12 a), without THz electric field incident on the EO crystal, the linearly polarized optical probe beam is transmitted through the EO crystal preserving its linear polarization. Then the quart wave plate transforms the linear polarization into circular polarization. A Wollaston prism separates the circular light into two equal intensity beams, which are detected by a balance photodiode. Under good alignment, the output of the balance photodiode is zero. In the presence of the THz transient in the EO crystal, birefringence is induced in the EO crystal, which changes the linear polarization of the optical probe beam to an elliptical polarization. Thus, after the quart wave plate, the light is no more circular, and the intensity differences of the two beams after Wollaston prism incident on the photodiode are no more balanced. The induced intensity difference is proportional to the THz electric field in the EO crystal since its expression is given by :

$$\Delta I = I_0(\frac{2\pi}{\lambda} n^3 r_{41} L)F \qquad 4.4$$

Where I_0 is the intensity of the optical probe pulses, λ is the wavelength of the optical probe pulses, and n is the refractive index of the EO crystal, L is the crystal thickness; r_{41} is the electro-optic coefficient of the crystal. The intensity difference measured by the balance photodiode was feed to a lock-in amplifier with the frequency of the reference signal given by the frequency of the mechanical chopper placed on the optical pump beam. By varying the time delay between the THz electric field and the optical probe beam, we can reconstruct the whole THz transient.

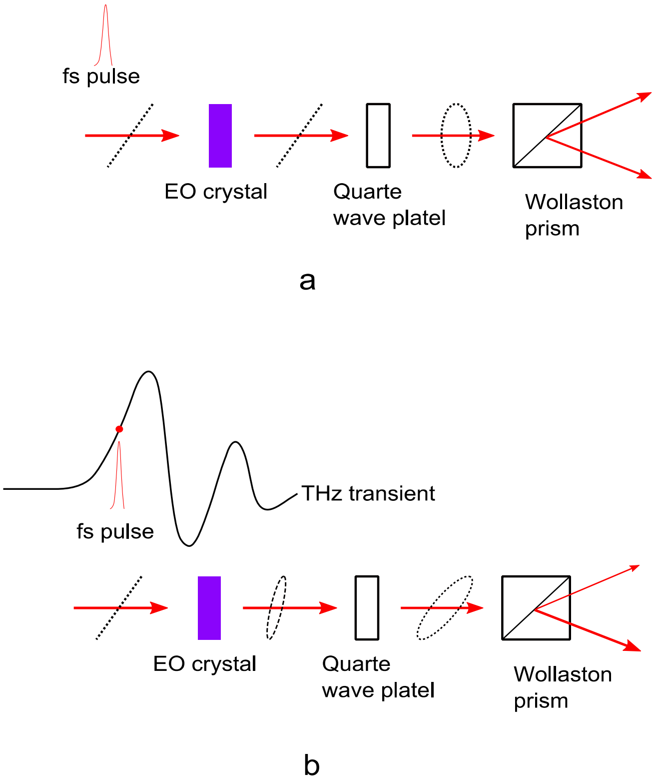

Figure 4.12: Electro-optic detection diagram without (a) and with (b) the THz transient in the EO crystal.

From the equation 4.6, we can see that the intensity modulation is not only proportional to the THz electric field, but also to the crystal thickness. Thicker is the crystal, higher the intensity modulation is. However equation 4.6 is only valid if the phase-matching condition is met. This requires that the group velocity of the optical probe pulses and the phase velocity of the THZ frequency components are equal. The velocity mismatch will cause the optical probe pulses to sweep temporally across the THz transient, and reduce the time resolution and hence the detection bandwidth. Thicker is the crystal, larger is the phase mismatch. So there is a trade-off between intensity modulation and bandwidth. The selection of the EO crystal thickness depends on the experimental bandwidth that is needed.

For optimal performances, the candidate EO crystal should have a large electro-optic coefficient and at the same time preserve low velocity mismatch. A variety of EO crystals have been proposed, like $LiTaO_3$[78], ZnTe[79] and GaP[80]. ZnTe benefits on a large electro-optic coefficient of 4 pm/V[80], in comparison for instance with 1 pm/V for GaP crystal. Moreover, the detection bandwidth is relatively broad for a thin ZnTE crystal. The shortcoming of the ZnTe crystal is it has the first TO resonance at 5.3 THz[81], which limits the detection sensitivity around this frequency. The detection response of ZnTe crystals with various thickness is found in reference[33]. In our case, we selected 500 μm-thick ZnTe crystal to ensure detection bandwidth up 4 THz.

4.5 Results

The superlattice sample used for the THz emission of Bloch oscillations was the V1764 sample. The central wavelength of the femto-second optical pulses used for the excitation was set to 790 nm (1.57 meV), slightly lower than the hh_0 transition of the WSL. The optical power of the pump beam incident on the superlattice sample was 6 mW. For a pump spot diameter of 600 μm, the carrier density was lower than 10^9 cm^{-2} to avoid screening of excitons. During the measurement, the sample was hold at 10 K, and the setup is purged with dye Nitrogen gas with humidity of 10%. To check for possible contributions caused by surface states of the semiconductor superlattice sample, the THz emission was measured for pulse energies well below the first miniband. No THz radiation was detected under this condition. Thus, we make sure that the observed THz emission only originates from the superlattice states.

Figure 4.13 shows the detected THz transients due to Bloch oscillations for increasing the applied electric field. We clearly observe that, with the increase of the applied electric field, the cycles of the oscillations in time domain increases. Figure 4.14 shows the THz amplitude spectra for different applied electric field calculated by Fourier transform of the temporal waveforms shown Figure 4.13. We observe that the spectra shift to higher frequency as the applied electric field is increased. I analyzed the central frequency of the traces by fitting a Lorentzian to the emission peak in the THz amplitude spectrum. The center frequency of the

Lorentzian function as function of the applied electric field is depicted in Figure 4.15. A linear field-dependence with an emission frequency following the WSL splitting is evident in the graph.

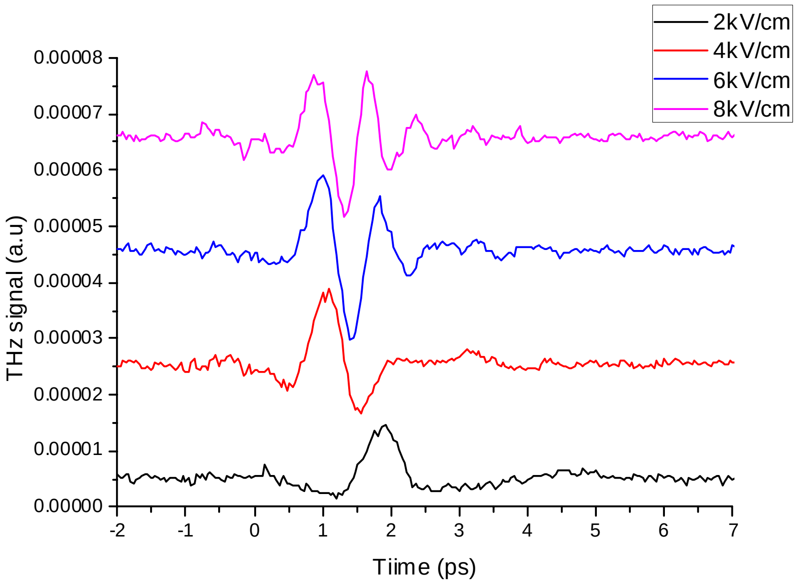

Figure 4.13: Temporal waveforms emitted due to Bloch oscillation as function of applied electric field in V1764 sample at 10 K.

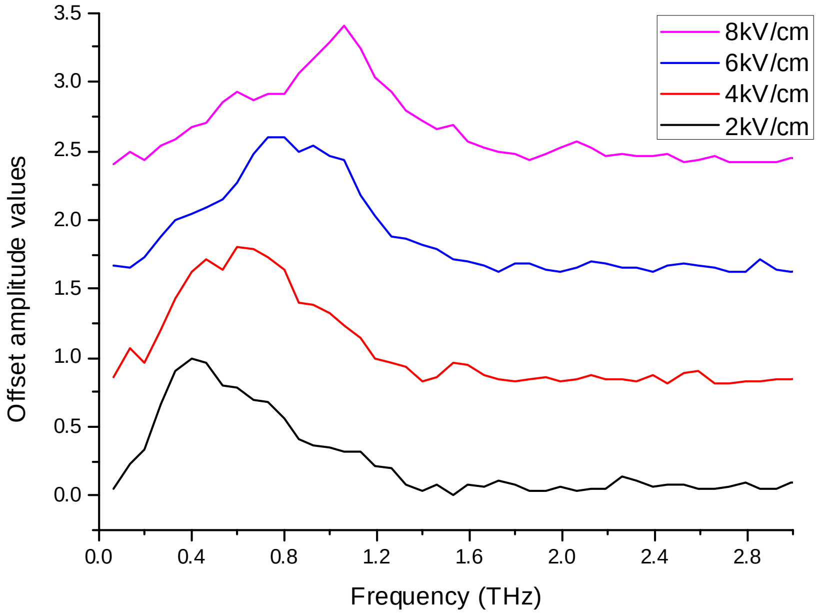

Figure 4.14: THz amplitude spectra for different applied electric field.

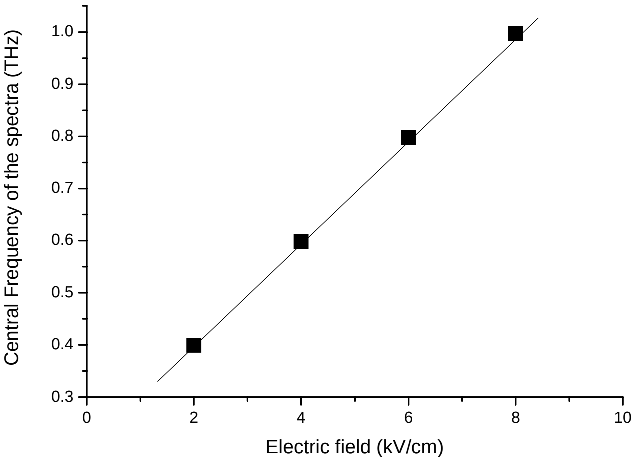

Figure 4.15: Central frequency of the THz spectra as function of applied electric field. The linear field-dependence is emphasized by a linear fit.

4.6 Perspectives

The THz emission of Bloch oscillations in optically excited undoped semiconductor superlattices have been observed by several groups[23, 26, 28]. As the electron scattering time decreases with increasing temperature, the Bloch oscillations are damped faster at high temperature. The dephasing time at room temperature is estimated to be 130fs in GaAs/AlGaAs superlattice. Consequently, detection of the THz emission of Bloch oscillations at room temperature requires the development of THz TDS set-up with a detected bandwidth of more than 10 THz[82]. Although the existence of Bloch oscillations at room temperature has been verified using a transmission electro-optic sampling technique, the THz emission of Bloch oscillations at room temperature has not been directly measured yet. The fast scattering time induces large energy level broadening. To observe Bloch oscillations at room temperature, high electric field should be applied on the superlattice to provide larger energy splitting of the WSL states than the energy level broadening. However, applied high electric field causes strong electron wavefunction localization and hence reduces the amplitude of the Bloch oscillations. As a result, superlattice structure with wide first miniband is preferred to ensure significant Bloch oscillation amplitude under high electric field applied to the superlattice. The B9R231 sample shows a wide miniband width of 52 meV and the WSL is well revolved in the photocurrent spectrum at room temperature as shown on Figure 4.9. This sample is thus a very promising device for the observation of the THz emission of Bloch oscillations at room temperature. We plan in the future to develop a new THz TDS system based on 15-fs duration optical pulses and thin ZnTe or GaP crystal enabling coherent detection of THz radiation up to 30 THz and exploit it to measure and analyse the THz emission of Bloch oscillations at room temperature.

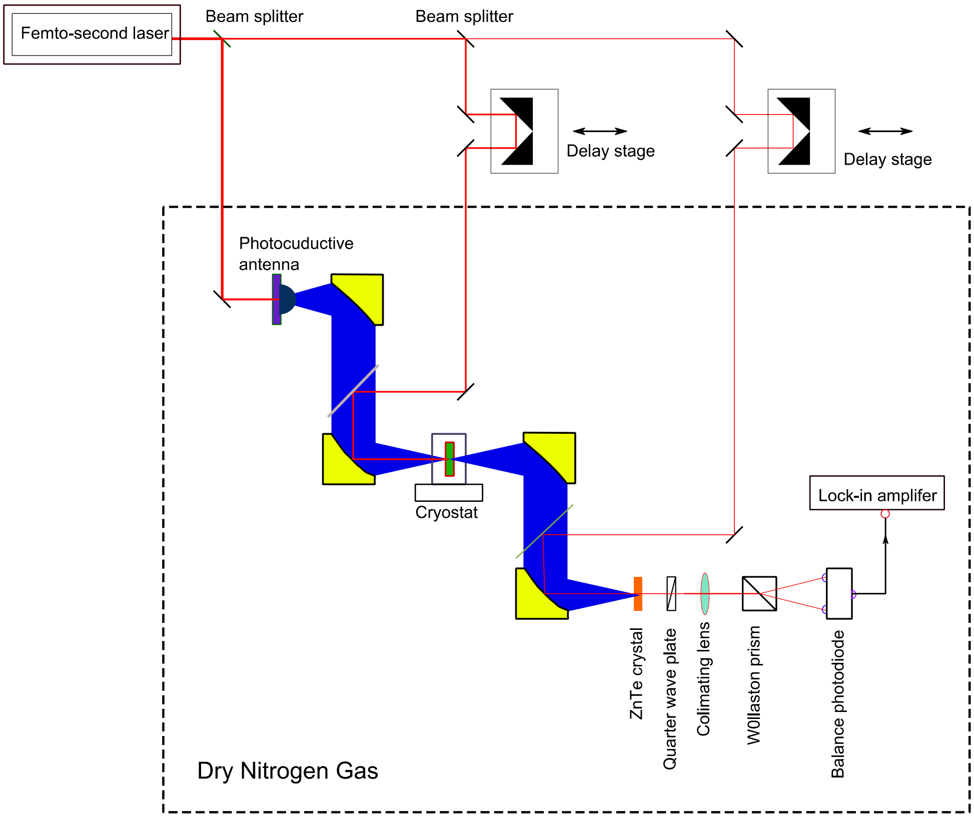

Figure 4.16: Schematic drawing of the optical pump-THz probe experimental setup for the investigation of absorption and gain dynamics associated with the Bloch oscillations.

Another future experiment we plan to perform is to study the Bloch gain associated with the Bloch oscillations in optically excited undoped superlattice sample by using an optical pump-THz probe experiment. Whereas the Bloch gain in optically excited undoped semiconductor superlattice has never been observed directly, this technique paves the way its observation opening the practical application of tunable THz sources based on Bloch oscillations. The possible experiment setup is depicted in Fig 4.16. In such experiment, the superlattice sample is optically excited by femto-second optical pump pulses to drive Bloch oscillations. A synchronized THz beam, obtained by the THz pulses delivered by an optically excited photoconductive antenna, will probe the THz response of the superlattice sample as a function of the optical pump and the THz probe delay. From this experiment, we will investigate the THz absorption and the gain associated to the Bloch oscillations and we will also exam their dynamic.

5 Photocurrent study of Wannier Stark Ladder

Photocurrent spectroscopy is widely used to explore energy band profile of semiconductor structures. In the previous chapter, photocurrent spectra of dc biased undoped superlattices were analyzed and discrete photocurrent peaks related to WSL states were observed. This study was performed using low excitation intensity provided by halogen lamp In this chapter, we present the investigation of the photocurrent-voltage characteristic in dc biased undoped superlattices under low and high excitation intensity provided by a monochromatic laser light. The laser induces and controls a differential negative conductance based on field-dependent absorption of negative index Wannier Stark transitions in undoped semiconductor superlattices. The electric field ranges of the differential negative conductance regions are controlled by the wavelength of the laser, and the magnitude of the differential negative conductance can be tuned by the optical power. Furthermore, when pumping at relatively high optical power, we found that the differential negative conductance become nonlinear and show bistable behaviors.

5.1 Laser-induced negative differential conductance (NDC)

The negative differential conductance exhibited by many materials and devices has been widely used to implement oscillators and amplifiers in the microwave and the THz frequency range. Various physical phenomenons may give rise to negative differential conductance. Indeed, since the current density in semiconductor is proportional to both the density of carriers and their drift velocity, a decrease in current density with an increasing electric field can be brought by a decrease in either of these two parameters. For instance, in the well known Gunn Effect[83], the negative differential conductivity is based on the field induced transfer of conduction band electrons from low energy, high mobility valley to higher energy, low mobility satellite valley. Whereas in gold doped germanium, the negative differential conductance is due to field enhanced trapping of the electrons[84]. Usually, the characteristics of the negative differential conductance are determined by intrinsic material and/or design parameters, which prevent their adjustments in real time by any external parameters. Here, we study the negative differential conductance based on field-induced absorption of negative index WS transitions in undoped semiconductor superlattices excited by monochromatic laser.

5.2 photocurrent spectroscopy set-up

The experimental configuration is shown in Figure 5.1, the tunable continuous Ti:Sapphire laser (Spectra-physics Model 3900) was used as the light source. The output power of the laser reaches ~0.5W when pumped by a Verdi laser of 7 W.The spectrum width of the TEM_{00} mode is less than 40 GHz. The power of the laser incident on the undoped superlattice sample, ranging from 0.1 µW to 50 mW, is controlled by a variable attenuator. The laser beam is partially reflected by a pellicle beam splitter with a reflection ratio of 8% to control the optical power incident on the sample using a power meter. The incident optical beam is focused by a 25 cm focusing lens; the diameter of the optical beam focused onto the superlattice sample surface is of the same size with the diameter of the superlattice mesa. The laser is incident on the superlattice sample at normal incidence and is modulated by a mechanical chopper at 1.7 kHz. The photocurrent is detected with a lock-in amplifier in current mode. The power supply (Agilent E3647A) provides the dc electric field applied to the superlattice sample. For all experiments, the superlattice samples are mounted in a helium-flow cryostat and are cooled down at 10 K.

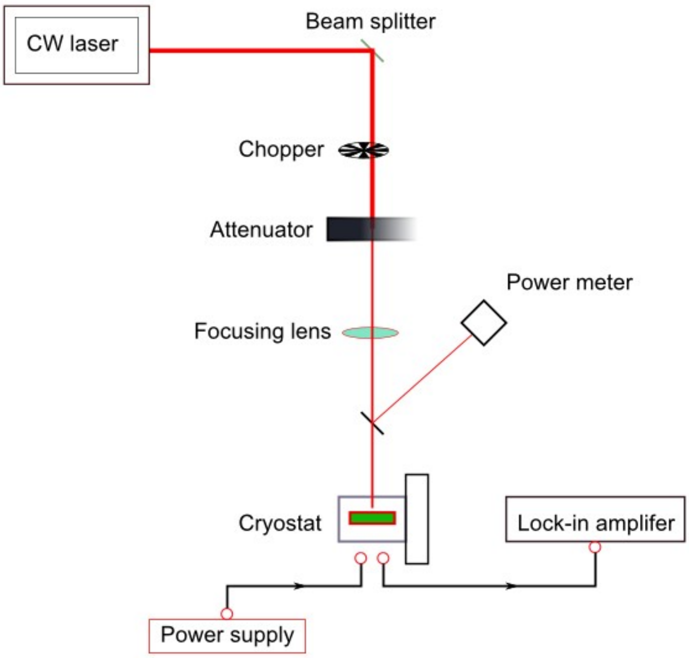

Figure 5.1: Schematic diagram of experimental configuration for photocurrent measurement

The Lock-in amplifier in current mode saturates at 1 µA, whereas the photocurrent in our experiment can reach higher values. To overcome the current saturation, a simple circuit as indicated in Figure 5.2 is used to proportionally reduce the photocurrent flowing in the lock-in. Two resistances of 50 Ω and 1.5 MΩ are connected in parallel, and then connected in series to the superlattice sample. The equivalent resistance values is about 50 Ω, far less than the resistance of the superlattice, which is typically more than 60MΩ without laser excitation and tens of kΩ with the laser excitation at cryogenic temperature. This guarantees that the applied voltage drops on the superlattice sample, with negligible distribution on the two parallel resistances. The current measured by the lock-in amplifier with this circuit is thus 3.3×10^{-6} times smaller than the current that flows through the superlattice sample, avoiding saturation of the lock-in amplifier.

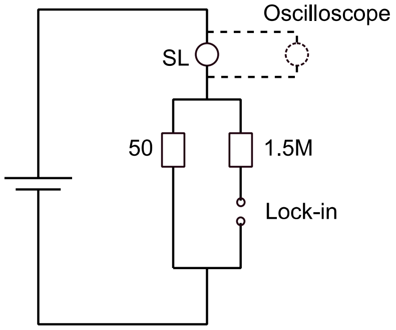

Figure 5.2: Electric loop for photocurrent measurement

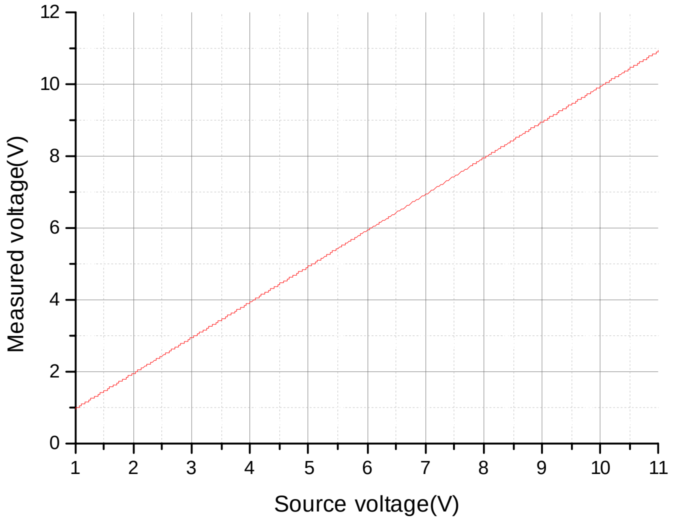

Figure 5.3: The voltage measured on the superlattice as function of applied source voltage

Before carrying on the photocurrent-voltage experiments, I verify that the voltage drops essentially to the superlattice samples. To clarify this, I measured the voltage applied on the superlattice samples through a current sensor (input resistance of 10MΩ) and the oscilloscope. The measured voltage as function of the voltage provided by the source is reported in Figure 5.3. Within only 0.01V difference, the measured voltage equals the voltage provided by the source.

To estimate the excitation power incident onto the active region of the superlattice samples, we measured the transmission coefficient of the cryostat window of 16%, and the transmission coefficient of the semitransparent layer of 40%. The laser beam is Gaussian beam, and the Gaussian beam waist was adjusted to be ~600μm. Taking into account these parameters, we calculated that 42.3% of the laser power is incident on the active region of the superlattice samples.

5.3 Results

5.3.1Change from symmetric to asymmetric line shapes as the optical power increase

Figure 5.4 reports the photocurrent-voltage characteristic measured at 6 μW with the photon energy of 1.554 eV. Above 2.3 V, the electron and hole minibands split into a series of discrete levels forming the Wannier Stark Ladder. Since the photon energy is below the energy of the vertical Interband transition, only diagonal interband transitions with negative index, i.e. from heavy-hole states to electron states centered in different quantum wells, are probed. As the applied voltage is increased, the energies of the diagonal interband transitions decrease as well as their strengths due to the localization of the hole and electron wave functions in their own GaAs quantum wells. Each voltage value for which the energy of one diagonal transition fits the photonenergy, a peak in photocurrent appears in the characteristic. For voltage ranging from 2 V to 8 V, up to four diagonal transition energies (hh_{-1}, hh_{-2}, hh_{-3}, hh_{-4}) fit with the incident photon energy. These photocurrent peaks correspond to a significant increase of the carrier density resulting from the strong absorption of photons when diagonal interband transitions are resonant with photon energy. The low voltage side of the photocurrent peaks reflects the progressive tuning of the diagonal excitonic transitions to the optical photon energy, resulting in the increase of the carrier density. In return, the high voltage side of the photocurrent peaks corresponds to a continuous detuning of the energy of the diagonal transition with photon energy, resulting in the decrease of the current density. The current density given by the latter process is decreased with voltage increasing. This NDC is directly caused by the field-dependent absorption of the diagonal Wannier-Stark transitions. The Lorentzian shapes of the photocurrent peaks are fully determined by the spectral distribution of the laser.

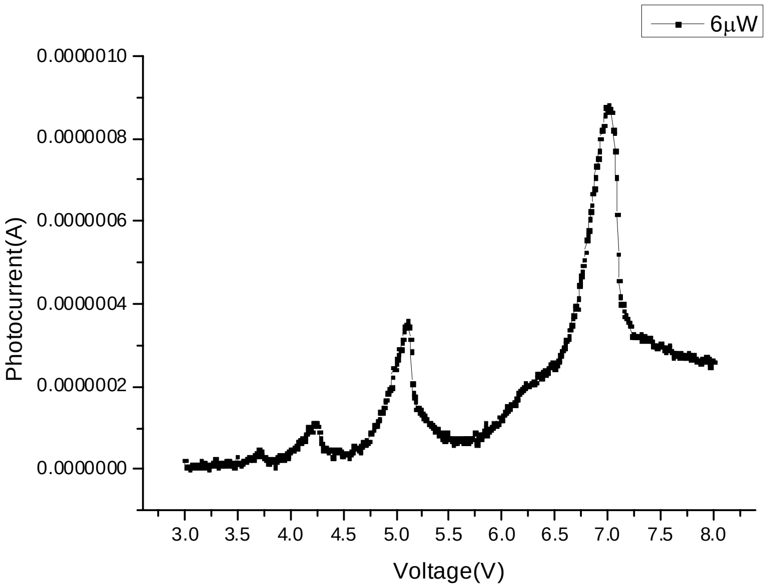

Figure 5.4: Photocurrent voltage characteristic measured with 6 μW optical power and 797 nm wavelength

Commonly, the NDC exploited in semiconductor superlattices is based on quantum tunneling process; its characteristics are determined by the material properties and the design and thus are no more adjustable after growth. In return, the characteristics of the NDC reported in this thesis are based on field-induced absorption which can actively be controlled by the laser. Indeed, the wavelength of the laser defines the voltage range where NDC regions occur and the spectral width of the laser, the voltage width of the NDC.

The power of the laser provides one other parameter which can be exploited to change the characteristics of the NDC based on field-induced absorption in semiconductor superlattices. Figure 5.5 illustrates the photocurrent-voltage characteristic measured at 90 μW with the photon energy of 1.554 eV. Comparing with 6 μW excitation power discussed previously, the higher power excitation benefits higher signal noise ratio and hence reveals more diagonal transition photocurrent peaks: more than 6 WSL transitions can be resolved. With the increase of the excitation power, the WSL photocurrent peaks shift to higher voltages and the photocurrent lineshapes are observed to become asymmetric. The detailed analysis on peak voltage shifts and lineshape changes are discussed in the following.

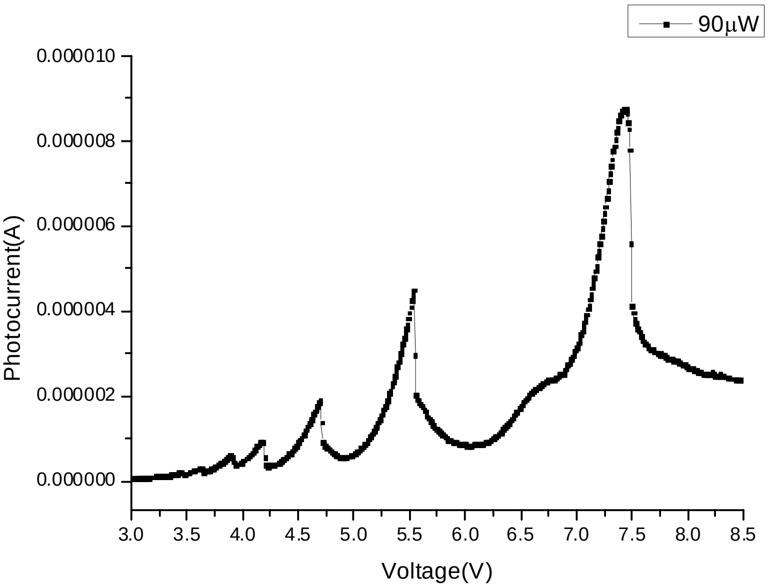

Figure 5.5: Photocurrent voltage characteristic measured with 90 µW optical power and 797 nm wavelength

Figure 5.6 a) and b) show the photocurrent-voltage characteristics of the semiconductor superlattice in the voltage range where the energies of hh$_{-1}$ and hh$_{-2}$ Wannier Stark transitions are resonant with the photon energy for optical powers of 10µW, 100µW and 1mW. As the power increases, the lineshapes become asymmetric deviating from the Lorentzian type: the shape broadens on the low voltage side and shows steeper slope on the high voltage side. This deviation of the Lorentzian lineshapes becomes more and more pronounced as the laser power increases. At about 1mW, lineshapes are strongly asymmetric with a width on the high voltage side of less than 0.02V, providing an extremely high NDC. The laser power is thus a convenient experimental control parameter to tune the NDC characteristics.

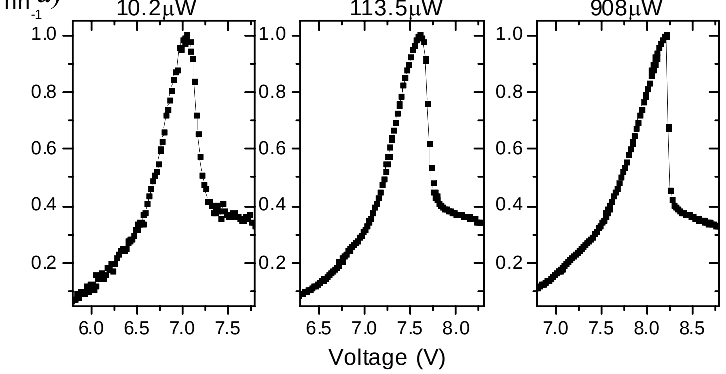

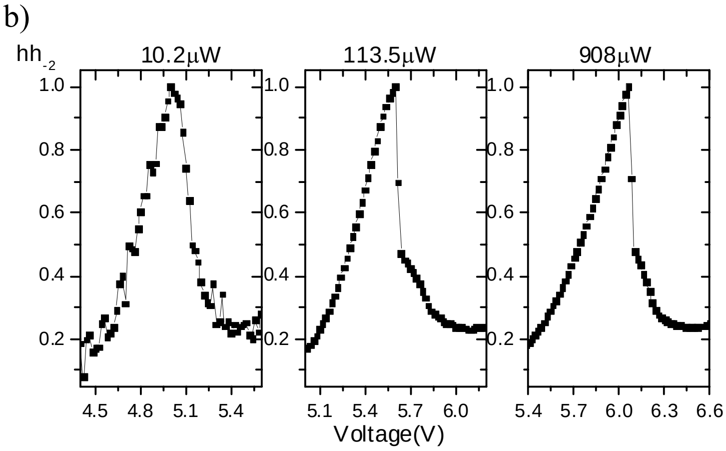

Figure 5.6: Photocurrent-voltage characteristics when the photon energies are in resonance with a) hh_{-1} and b) hh_{-2} WSL energies for different optical powers.

The dependence of the current-voltage characteristics on the optical power is the signature of a nonlinear regime. We attribute this nonlinear regime to a positive feedback mechanism due to the interplay between Wannier-Stark absorption, built-in field and accumulation of photocarriers in the buffer layers on the both ends of the superlattice. The electric field distribution and electron accumulate characteristic is schematically shown in Figure 5.7 Indeed, the carriers in the superlattice experience a local potential V_i corresponding to the applied voltage minus the potential drops V_e and V_h at the two buffer layers which depend on the density of accumulated photocarriers. Increasing the bias voltage improve the match between the diagonal interband transition energy and the laser energy increasing the absorption of photons. The density of photocarriers accumulated in the buffer layers is thus higher, leading to an increase of the potential drops V_e and V_h. As a result, the local potential V_i in the superlattice region is lowered, stretching the low voltage side of the peak. Once the energy of the diagonal interband transition becomes lower than the energy of the photons, the absorption falls, reducing the potential drops V_e and V_h. This initiates positive feedback where the reduction of potential drops at the buffer layers increases the local potential V_i, further increasing the diagonal transition energy away from the energy photon and further reducing the absorption of incident photon. This effect causes the sharp drop in the high voltage side of the peaks. This nonlinear effect becomes increasingly obvious for higher powers.

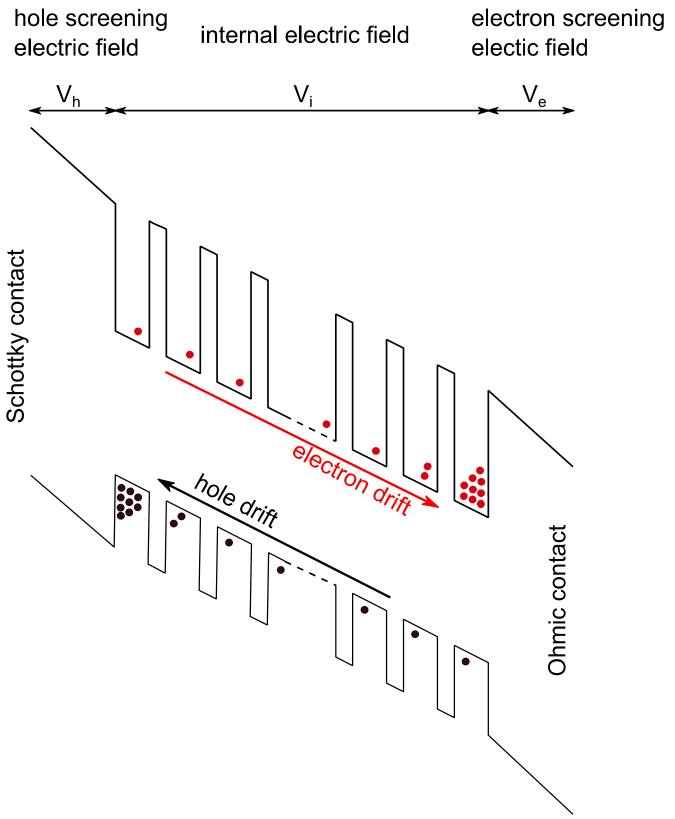

Figure 5.7: Schematic band edge diagram of the structure. The electrons and holes transport in the intrinsic region of superlattice and accumulate at the quantum well beside the buffer layers.

5.3.2 Peak photocurrent and peak voltage shift with optical power

In addition to the observed distortion of the lineshapes, peaks voltage shift and peak photocurrent increasing are observed when changing the optical power. Figure 5.8 a) and b) illustrate the peak photocurrent change and voltage shift with increasing optical power for electron transition hh_{-1}. The peak photocurrent increases linearly with the increase of the optical power for over four orders of magnitude. This tendency is expected since photocarrier’s density is proportional to the optical power in the linear regime. The voltage of the photocurrent peaks increases following a logarithmic law for optical power of less than 1 mW, and a deviation from the logarithmic law is observed with the increase of voltage at higher optical power.

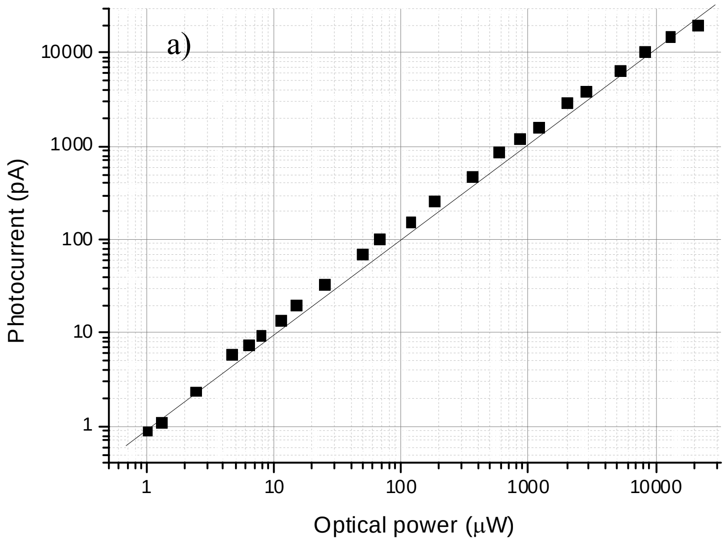

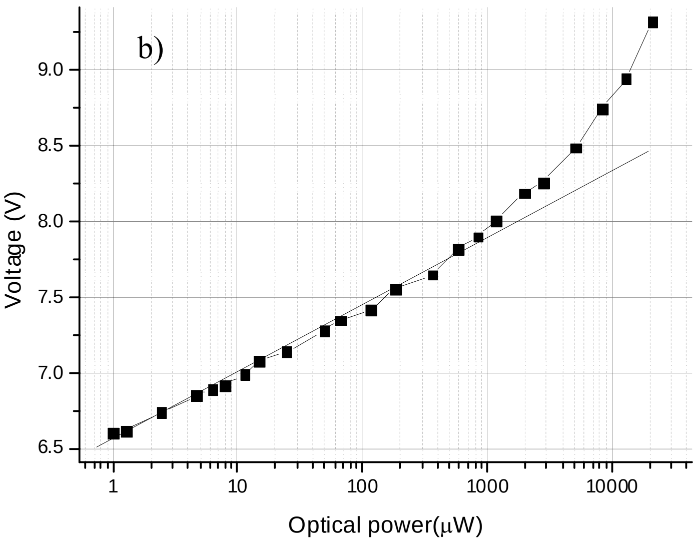

Figure 5.8: hh_{-1} transition peak photocurrent increase with optical power a) and the peak voltage shift with optical power b)

The peak photocurrent and peak voltage shift of higher order WSL transitions were also measured and the same dependences with the optical power are observed.

To further explore the photo generated carrier transport characteristic and the photocurrent dependence on the optical power, the photon energy was adjusted to higher the intrawell hh_0 transition energy, where the absorption coefficient is not sensitive to the applied voltage. The photocurrent as function of applied voltage was recorded.

Firstly, the optical wavelength was adjusted to 780 nm, 1.59 eV, slightly higher than the hh_0

transition energy. The photocurrent was measured with different optical powers. The results are illustrated in Figure 5.9. For three different optical powers, the photocurrent starts to increase above an offset voltage and then increases to reach a constant value above a certain threshold voltage. The small photocurrent variation indicated by the arrow in Figure 5.9 results from the light hole transition, which is not interested here.

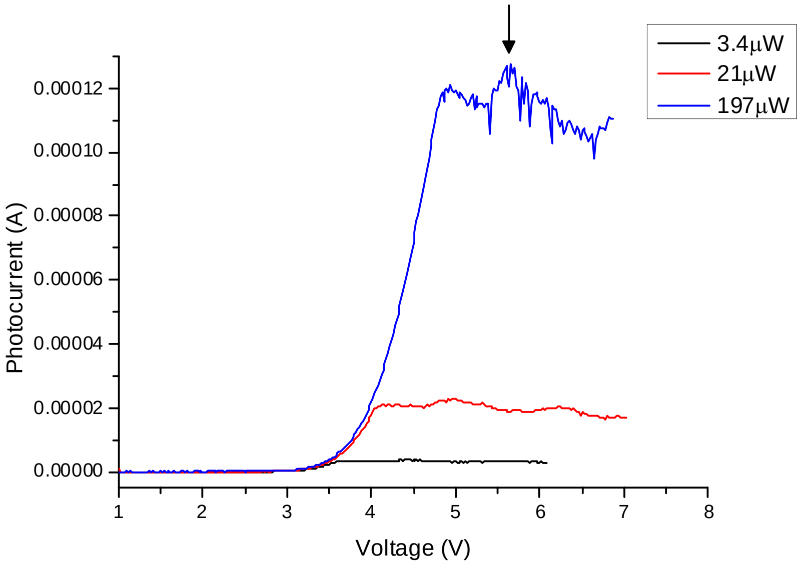

Figure 5.9: Photocurrent as function of applied voltage for three optical powers. the photo energy is 1.59 eV.

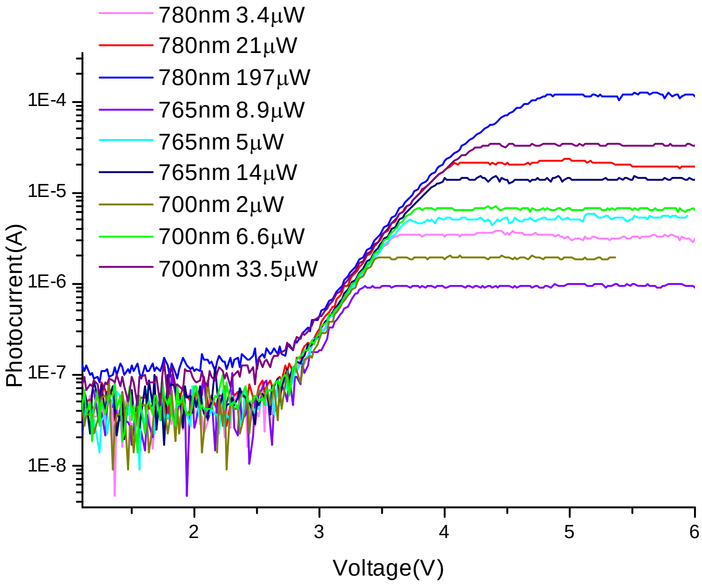

Figure 5.10: Photocurrent as function of applied voltage for different optical powers at 1.59 eV (780 nm), 1.621 eV (765nm) and 1.771 eV (700 nm).

Other photocurrents with laser wavelength of 765 nm (1.621eV) and of 700 nm (1.771eV) were also measured. The photocurrent-voltage characteristics for all the measurements are illustrated in Figure 5.10. Despite different photon energies, the photocurrent shows the same characteristic, where the photocurrents start to increase at the same voltage offset, and reach a constant value above different threshold voltages.

5.3.3 Voltage offset study

All the photocurrent-voltage characteristics show the photocurrent starting point above 2.7 V. This voltage offset may originate from the voltage drop at the Schottky barrier of the top contact and at series resistances. To further identify the origin of this voltage offset, two measurements were carried out.

The temperature dependence of this voltage offset is measured and reported in Figure 5.11. The voltage offset shows slightly increase from 2.3 V to 2.5 V up to 60 K, and then the voltage offset decreases to positive 0.9 V until 170 K. After 170 K, the offset then persists unchanged. Such offset voltage temperature dependence was also observed in the doped superlattice sample L358.

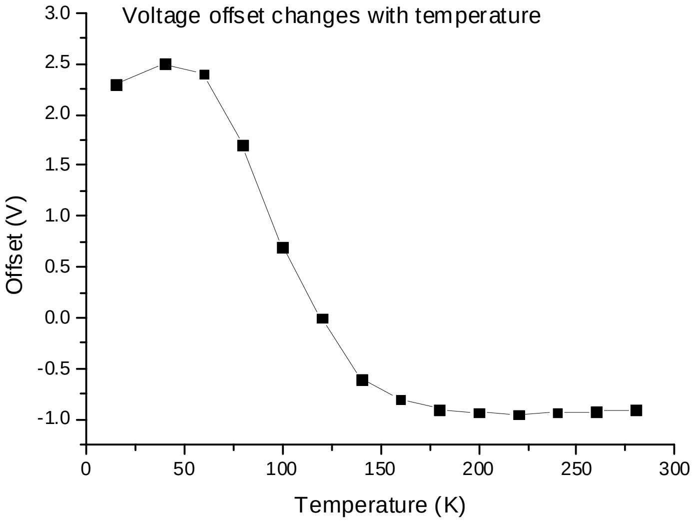

Figure 5.11: Offset voltage measured with different heat sink temperatures.

I applied positive and negative voltage on the sample and measured the photocurrent at 77 K. the measured results are shown in Figure 5.12. To have good comparison with other measurements, the positive photocurrent was recorded with negative value. As can be seen from the results, both positive and negative photocurrents begin to increase at about 1.3 V, which is in accordance with the previous temperature dependent measurement. Both positive and negative measurement gives well-resolved WSL, and for the same index of WSL photocurrent, the photocurrent peaks with the positive voltage is higher than with negative voltage, and hence the peak voltages shift to higher voltages. Since for the same index of the WSL, the same optical power and same absorption coefficient produce the same number of photo generated carriers, thus the difference in the photocurrent only stems from the carrier accumulation and tunneling difference at the both ends of the superlattice. Indeed, the buffer layers on the both side of the superlattice are difference in thickness (200 nm on the top and 300 nm below). Inversing the applied electric field induces that each of the two kinds of carriers accumulates at opposite buffer layers, which in return give different carrier accumulation and tunneling characteristic and hence different photocurrent.

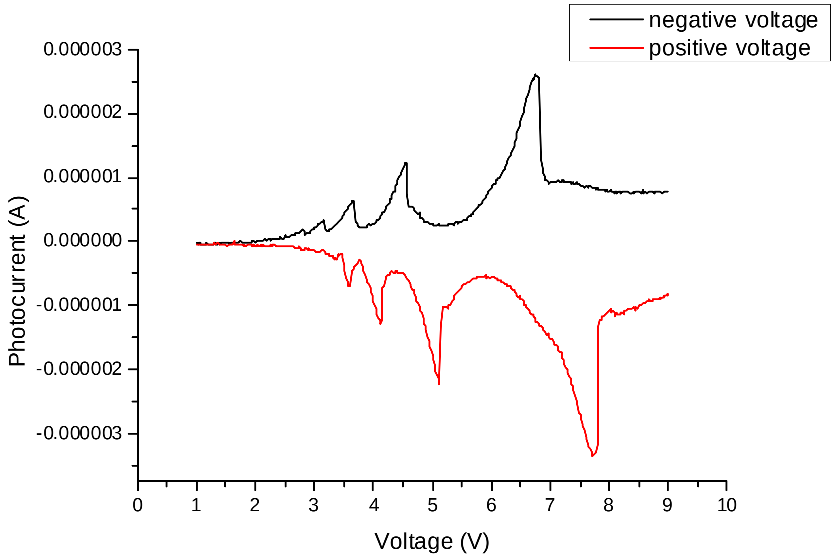

Figure 5.12: Photocurrent measured with both positive and negative applied voltage

5.3.4 Fan charts at different excitation optical powers

To provide advanced analysis of the observed photocurrent peak shift, we measured the photocurrent-voltage characteristics for optical wavelengths ranging from 790 nm to 806 nm in steps of 1 nm at 100 µW, 1mW and 10mW. These measurements provide fan charts in the Wannier Stark regime plotted in Figure 5.13 a-c. The wavelength axis was converted to an energy axis.

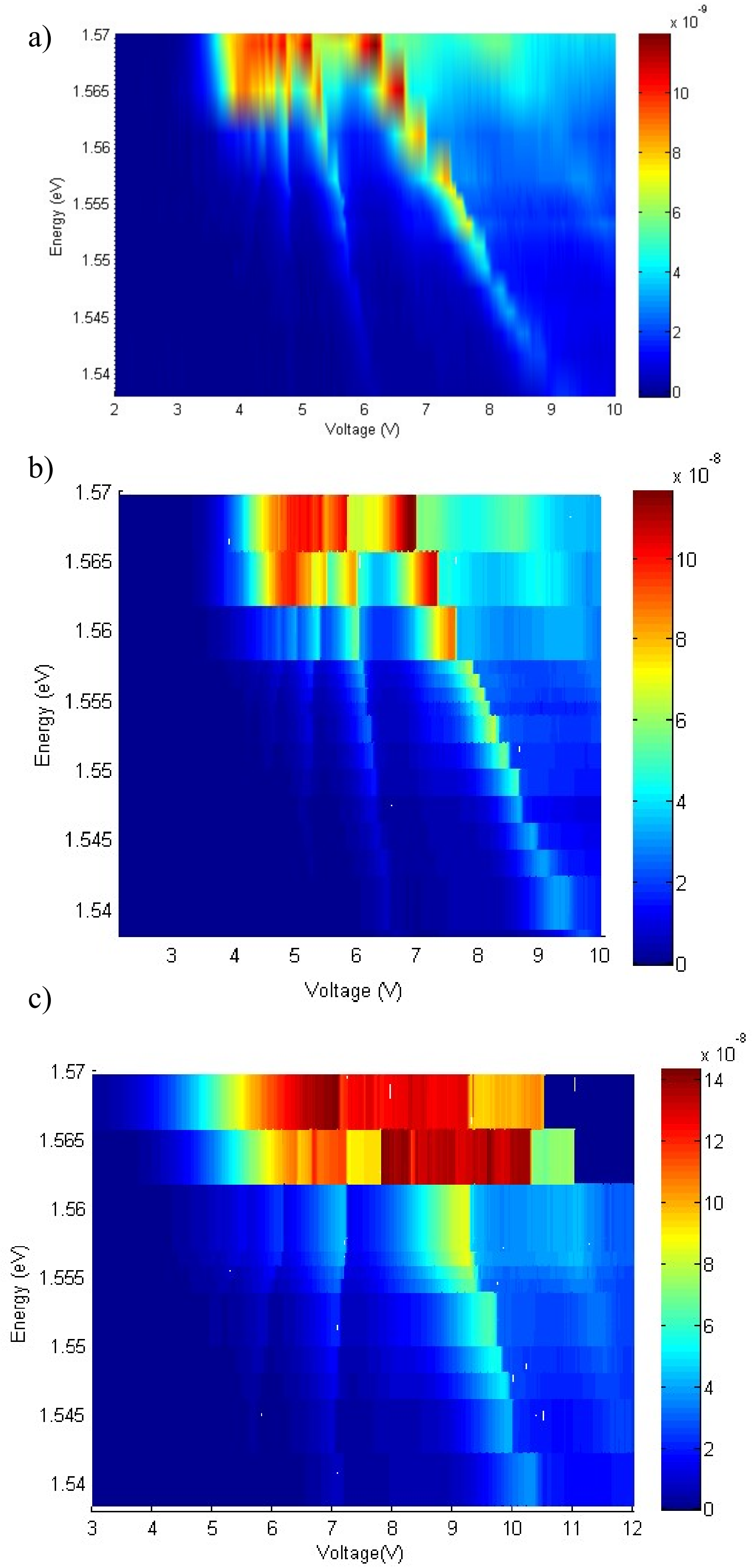

Figure 5.13: Photocurrent fan chart for 100 µW, 1mW and 10 mW optical power

At 100 µW, the spectral shift of the peak positions lightly deviates from the theoretical prediction considering the sample parameters and a linear relation between applied voltage and internal electric field. The negative slope of the peak positions is indeed 2 and 2.6 times lower for hh_{-1} branch andhh_{-2} branch respectively. We attribute this deviation to the beginning of the nonlinear regime. As the optical power increases, the red shift of the peak positions is more pronounced especially as the index of the transition is higher. Furthermore, peak positions do not follow anymore a constant shift with the voltage increasing over the voltage range under study. Besides, the slopes of hh_{-2} and hh_{-3} branch become surprisingly positive. These unusual behaviors of the peak positions with voltage increasing is a signature of the nonlinear regime resulting from the dependence of the local potential drop in the superlattice by the accumulation of photo generated carriers in the two buffer layers.

5.3.5 Bistability of the photocurrent

Within a certain range of laser powers, a hysteresis of the photocurrent voltage characteristic is observed in the NDC regions. Figure 5.14 a) and b) show the evolution of the current-voltage characteristics in the NDC region s associated to the hh-1 and hh-2 transitions respectively for different laser powers ranging from 10 µW to 1 mW. At 10 µW, the photocurrent is essentially independent of the direction of the voltage sweep, no hysteresis is observed. As the incident optical power is increased, hysteresis behaviors appear only in the DNC regions. More precisely, the limit voltages corresponding to the start and the end of the photocurrent decay are lower for reverse direction of the voltage sweep than for the forward direction. When pumping at power levels in the milliwatt range, the bistability effect is more pronounced. This bistability is the direct consequence of the modulation of the local potential drop in the superlattice by the potential drops in the two accumulation layers. The width of the bistability, defined by the difference in voltage of the current steps in the forward and the reverse directions, as a function of the incident optical power are reported Figure 5.15 for NDC regions associated to the hh_{-1} and hh_{-2}transitions. The width of the bistatiliby is increased with the increase of the incident optical power and reaches 0.03 V at 1mW. At higher optical power, the width of the bistability saturates and even lightly decreases. The increase of the bistability width with the optical power increasing is due to the increase of the photocarrier density located at the accumulation layers which causes the local potential inside the superlattice region to diverge further from the applied voltage.

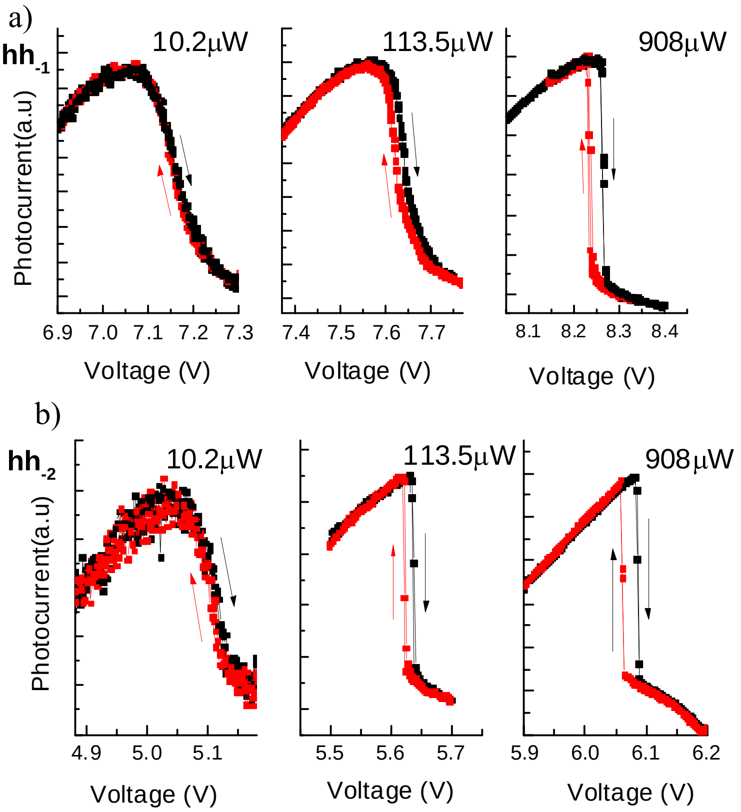

Figure 5.14: Photocurrent bistability measured of hh_{-1}transition a) and hh_{-2}transition b) with different optical power.

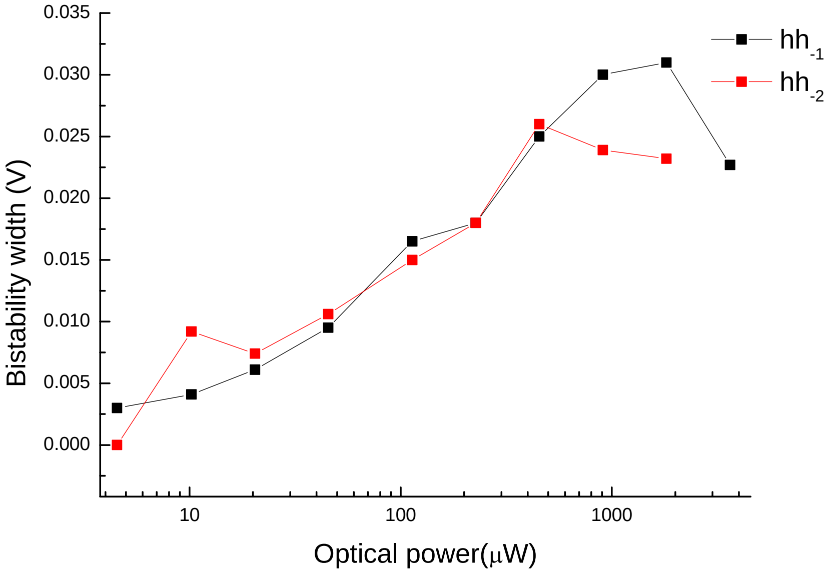

Figure 5.15: Photocurrent bistabliltiy width as function of optical power for hh_{-1} and hh_{-2} transitions

5.4 Conclusion

We have studied the photocurrent-voltage characteristics of undoped semiconductor superlattices excited by monochromatic laser. We showed laser-induced and -controlled of a differential negative resistance based on field-dependent absorption of negative index Wannier Stark transitions in semiconductor superlattices. The electric field ranges of the differential negative resistance regions are controlled by the wavelength of the laser light, and the magnitude of the differential negative resistances can be tuned by the optical power. Furthermore, when pumping at relatively high optical power, we found that the differential negative resistances become nonlinear and show bistable behaviors. We explain the existence of this nonlinear regime by a positive feedback mechanism due to the interplay between Wannier-Stark absorption, built-in field and accumulation of photo carriers at each end of the superlattice. Our results demonstrate the potential of exploiting the optical absorption of negative index Wannier Stark transitions in semiconductor superlattices, which depends on both photon energy and electric field, to provide laser-induced and -controlled differential negative resistances. By tuning the incident laser power, linear and nonlinear differential negative resistance are accessible. The possibility offers by the laser light to tune in real time the differential negative resistance properties should provide high flexibility and advanced functionalities for the implementation of devices based on differential negative resistance.

6 Conclusion

Doped semiconductor superlattices for development of THz emitter

To investigate the Bloch oscillations in doped semiconductor superlattice for the development of THz emitter. We have designed, fabricated as well as tested cascade super-superlattice structure devices based on AlGaAs/GaAs superlattice system. The cascade super-superlattice strucuture was designed based on resonance LO phonon injector scheme, where the thin elementary superlattices are imbedded with resonant LO phonon injector to simultaneously preserve the Bloch gain and suppress the electrical domain formation. The thin superlattice and resonant LO phonon injector module is duplicated to form 10 µm active region. The sample was processed into semi-insulating surface plasmon waveguide edge emitting device, semi-insulating subwavelength-grating surface emitting device, and double mental subwavelength-grating surface emitting device for electroluminescence measurement. The electroluminescence at around 10 meV (2.4 THz) was observed, however, the center frequency of the electroluminescence spectra is not sensitive to the applied voltage, which is not expected in theory. Further investigation of lateral current electromagnetic emission from n+doped bulk GaAs present the same electroluminescence spectra, indicating that what we have observed may originate from black body emission or impurity energy level transition. The sample was also processed into semi-insulating surface plasmon waveguide structure for absorption/gain measurement using THz TDS to explore the Bloch gain. The gain to loss crossover was obtained at around 3 THz for all the test devices, and the frequency where the gain to loss crossover occurs shifts to lower frequency with increasing electric field, which is opposite to the theory prediction. Considering the measurement results are not sensitive to the sample design, it is indicated that the electron transitions between resonant and localized impurity states and to the electron transitions involving the subband states contribute to the measured result.

To overcome this problem, we further plan to develop new Bloch devices operating at high frequency, in order that the Bloch frequency correspond to energies ranging from 12 meV (3THz) to 24 meV (6THz). In this frequency region, the Bloch gain is expected to be observed in higher frequency than the resonant transition between impurity states, such that the distortion from impurity can be excluded. Moreover, the frequency range is 12 meV lower than the LO phonon resonance in GaAs material, making sure that the LO phonon scattering will not take the main contribution for the electron transport and a large part of the electrons can still contribute to the Bloch gain.

Bloch emission time domain spectroscopy

Bloch oscillations in undoped superlattice was investigated through femto-second laser excitation. in this part, the undoped superlattice preserve the thickness of less than 1.5 µm, and the optical excitation provide small photocurrent, hence no electric domain is expected. I first measured the photocurrent spectroscopy using FTIR. The WSL was observing at both liquid Helium temperature and room temperature. the Bloch oscillations was detected by the time domain spectroscopy, where the Bloch frequency increase linearly with applied electric field. Since we can observe the WSL at room temperature in one of our samples, we plan in the future to develop a new THz TDS system based on 15-fs duration optical pulses and thin ZnTe or GaP crystal enabling coherent detection of THz radiation up to 30 THz and exploit it to measure and analyse the THz emission of Bloch oscillations at room temperature. Another future experiment we plan to perform is to study the Bloch gain associated with the Bloch oscillations in optically excited undoped superlattice sample by using an optical pump-THz probe experiment. Whereas the Bloch gain in optically excited undoped semiconductor superlattice has never been observed directly, this technique paves the way its observation opening the practical application of tunable THz sources based on Bloch oscillations.

Photocurrent study of Wannier Stark Ladder

We have studied the superlattice photocurrent as function of the applied voltage when the photo energy of pumping laser lies below the electron- heavy hole intrawell transition energy. Indeed, by fixing the excitation photon energy lower than the electron-heavy hole (hh_0) energy, the negative index WSL can be revealed through the photocurrent peaks as function of the applied electric field. Varying the excitation power, we observed that photocurrent-voltage characteristic shows unexpected behaviors: the WSL resonant transition peak photocurrent increases linearly with optical power, while the WSL resonant transition peaks voltage shifts to higher voltage, this can be interpreted that increasing otpical power increases the accumulation of photo generated carriers on the buffer layers, which in turn increases screening electric field. In addition, the photocurrent lineshapes evolves from symmetric Lorenzian shape to asymmetric shape. Moreover by varying the voltage in forward and inverse directions, we observed photocurrent bistability

Appendix

Processing procedure for semi-insulating surface plasmon structure

1. Cleave the wafer into sample of 1cm size.
2. Clean the surface of the sample.
    a) Clean the surface with Acetone and Isopropanol in sequence.
    b) Clean the surface with O_2 Plasma etching for 4min
    c) Clean the surface with BOE and HCL:H2O (1:3)
3. Lithography, the photoresist S1818 is used. Align and expose the device with MJB4 Mask Aligner, and develop in MF319 or MF350:H2O (1:4) developer
4. Etching the sample with the etchant H_2SO_4:H_2O_2:H_2O, with the ratio 1:8:20, and the etching speed is about 300nm/min. During the etching, the surface profiler DECTEK8 is used to control the etching thickness.
5. Clean the surface of the etched sample and remove the photoresist with Acetone and Isopropanol.
6. Lithography for bottom metal contact. Image reversal photoresist Ti 35ES is used. Align and expose the device with MJB4, and develop in AZ400K:H_2O (1:4) developer.
7. Clean the sample surface with O_2 Plasma etching for 4min. HCl: H_2O (1:3) etchant is used to remove oxidized layer on the sample surface.
8. Evaporate bottom contact with Ni/Ge/Au/Ni/Au(10nm/60nm/120nm/20nm/200nm)
9. Liftoff.
10. Annealing. Anneal the metal at 400^{o}C for 60s to diffuse the metal into the heavy doped GaAs forming ohmic contact.
11. Lithography for surface contact, the process is the same with step 6.
12. Clean the surface and remove the oxidize layer. The same with step 7.
13. Evaporate the top contact with Ti/Au(8nm/200nm).
14. Liftoff.
15. Polishing. Polish the back of the sample to 200um-250um thick.
16. Evaporate Ti/Au(10nm/200nm) on the back of the sample
17. Mounting and bonding

Processing procedure for double metal structure

1. Clean the sample wafer and a semi-insulating GaAs wafer of the same size.
2. Evaporate Ti/Au (10nm/500nm) on the two wafer surface
3. Wafer bonding.
4. Cleave the wafer into sample piece with 1cm size.
5. Remove the substrate.
   a) Mechanical polishing the substrate to about 100nm with sand paper.
   b) Selective etching the remaining substrate to etch stop layer. The selective etchant is citric acid monohydrate, hydrogen peroxide and DI water mixed with the ratio of $C_6H_8O_7$:H_2O_2:H_2O (3g:1mL:3mL)
6. Remove the etching stop layer ($Al_{0.5}Ga_{0.5}As$). Clean the surface with O_2 Plasma etching for 10min and etch the $Al_{0.5}Ga_{0.5}As$ with HF for 2min.
7. Reduce the thickness of the 600nm heavy doped GaAs layer to about 100nm. The etchant is H_2SO_4:H_2O_2:H_2O (1:8:120), the etching depth is monitored by surface profiler DECTEK8..
8. Clean the surface of sample and remove the photoresist with Acetone and Isopropanol.
9. Lithography for mesa. Use photoresist S1818, align and expose the device with MJB4 Mask Aligner, and develop in MF319 or MF350:H2O (1:4)
10. Etching the sample with the etchant H_2SO_4:H_2O_2:H_2O (1:8:10).
11. Remove the photoresist with Acetone and Isopropanol.
12. Lithography for top metal contact. Image reversal photoresist Ti 35ES is used. Align and expose the device with MJB4, and develop in AZ400K:H_2O (1:4).
13. Clean the sample surface with O_2 Plasma etching for 4min. And then HCl: H_2O (1:3) etchant is used to remove oxidized layer on the sample surface.
14. Evaporate top contact with Ti/Au (10nm/200nm)
15. Liftoff.
16. Polishing. Polish the back of the sample to 200um-250um thick.
17. Evaporate the Ti/Au(10nm/200nm) on back side of the sample
18. Mounting and bonding

Bibliography

1. Suzuki, S., et al., *Fundamental oscillation of resonant tunneling diodes above 1 THz at room temperature.* Applied Physics Letters, 2010. **97**(24): p. 242102-3.
2. Feiginov, M., et al., *Resonant-tunnelling-diode oscillators operating at frequencies above 1.1 THz.* Applied Physics Letters, 2011. **99**(23): p. 233506-3.
3. Kumar, S., Q. Hu, and J.L. Reno, *186 K operation of terahertz quantum-cascade lasers based on a diagonal design.* Applied Physics Letters, 2009. **94**(13): p. 131105-3.
4. Fathololoumi, S., et al., *Terahertz quantum cascade lasers operating up to 200 K with optimized oscillator strength and improved injection tunneling.* Opt. Express, 2012. **20**(4): p. 3866-3876.
5. Luo, G.P., et al., *Grating-tuned external-cavity quantum-cascade semiconductor lasers.* Applied Physics Letters, 2001. **78**(19): p. 2834-2836.
6. Sell, A., A. Leitenstorfer, and R. Huber, *Phase-locked generation and field-resolved detection of widely tunable terahertz pulses with amplitudes exceeding 100 MV/cm.* Opt. Lett., 2008. **33**(23): p. 2767-2769.
7. Rouvalis, E., et al., *Traveling-wave Uni-Traveling Carrier Photodiodes for continuous wave THz generation.* Opt. Express, 2010. **18**(11): p. 11105-11110.
8. Bloch.F, *uber die quantenmenchanik der elektronen in kristallgittern.* Z.Physik, 1928. **52**: p. 555.
9. Zener.C, *A theory of the electrical breakdown of solid dielectrics.* Proc.Roy.Soc.London, 1934. **Ser.A 145**: p. 523.
10. Betz, M., et al., *Ultrafast electron-phonon scattering in semiconductors studied by nondegenerate four-wave mixing.* Physical Review B, 1999. **60**(16): p. R11265-R11268.
11. Wannier, G.H., *Wave Functions and Effective Hamiltonian for Bloch Electrons in an Electric Field.* Physical Review, 1960. **117**(2): p. 432-439.
12. Mendez, E.E., F. Agulló-Rueda, and J.M. Hong, *Stark Localization in GaAs-GaAlAs Superlattices under an Electric Field.* Physical Review Letters, 1988. **60**(23): p. 2426-2429.
13. Esaki.L, T.R., *Superlattice and negative differential conductivity in semiconductors.* IBM J.Res.Dev., 1970. **4**: p. 61.
14. Ktitorov.A.S, S.S.G., Sindalovskii.Ya.V, *Bragg reflections and the high-frequency conductivity of an electronic solid-state plasma.* Soviet Physics-Solid State, 1972. **13**: p. 1872.
15. Willenberg, H., G.H. Döhler, and J. Faist, *Intersubband gain in a Bloch oscillator and quantum cascade laser.* Physical Review B, 2003. **67**(8): p. 085315.
16. Tarakanov, Y.A., et al., *Scattering-assisted terahertz gain in semiconductor superlattices in the Wannier-Stark-Ladder regime.* Physical Review B, 2006. **74**(12): p. 125321.
17. Yu.A.Romanov, L.k.O., V.P.Bovin, Sov. Phys.Semicond., 1978. **12**: p. 927.

18. H.Kroemer, *Large-amplitude oscillation dynamics and domain suppression in a superlattice Bloch oscillator.* arXiv: cond-mat, 2000. **0009311**
19. Ryndyk, D.A., et al., *Superlattice with hot electron injection: An approach to a Bloch oscillator.* Physical Review B, 2003. **67**(3): p. 033305.
20. Savvidis, P.G., et al., *Resonant Crossover of Terahertz Loss to the Gain of a Bloch Oscillating InAs/AlSb Superlattice.* Physical Review Letters, 2004. **92**(19): p. 196802.
21. Bouchard, A.M. and M. Luban, *Semiconductor superlattices as terahertz generators.* Physical Review B, 1993. **47**(11): p. 6815-6818.
22. Roskos, H.G., et al., *Coherent submillimeter-wave emission from charge oscillations in a double-well potential.* Physical Review Letters, 1992. **68**(14): p. 2216-2219.
23. Waschke, C., et al., *Coherent submillimeter-wave emission from Bloch oscillations in a semiconductor superlattice.* Physical Review Letters, 1993. **70**(21): p. 3319-3322.
24. Lyssenko, V.G., et al., *Direct Measurement of the Spatial Displacement of Bloch-Oscillating Electrons in Semiconductor Superlattices.* Physical Review Letters, 1997. **79**(2): p. 301-304.
25. Sudzius, M., et al., *Optical control of Bloch-oscillation amplitudes: From harmonic spatial motion to breathing modes.* Physical Review B, 1998. **57**(20): p. R12693-R12696.
26. Fanciulli, R., et al., *Coherent control of Bloch oscillations by means of optical pulse shaping.* Physical Review B, 2005. **71**(15): p. 153304.
27. Shimada, Y., et al., *Terahertz Conductivity and Possible Bloch Gain in Semiconductor Superlattices.* Physical Review Letters, 2003. **90**(4): p. 046806.
28. Sekine, N. and K. Hirakawa, *Dispersive Terahertz Gain of a Nonclassical Oscillator: Bloch Oscillation in Semiconductor Superlattices.* Physical Review Letters, 2005. **94**(5): p. 057408.
29. P.Drude, *Zur elektronentheorie der metalle.* Ann.Phys.Lpz, 1900. **1**.
30. N.W.Ashcroft, N.D.M., *Solid State Physics*. Saunder, Philadephia. 1981. P225.
31. Schultheis, L., et al., *Ultrafast Phase Relaxation of Excitons via Exciton-Exciton and Exciton-Electron Collisions.* Physical Review Letters, 1986. **57**(13): p. 1635-1638.
32. Dignam, M., J.E. Sipe, and J. Shah, *Coherent excitations in the Stark ladder: Excitonic Bloch oscillations.* Physical Review B, 1994. **49**(15): p. 10502-10513.
33. Rosam.B, *Intraband dynamics in the optically excited Wannier-Stark Ladder spectrum of semiconductor superlattice*, in *Fachrichtung Physik*. 2004, Technische Universitat Dresden: Dresden.
34. Bouchard, A.M. and M. Luban, *Bloch oscillations and other dynamical phenomena of electrons in semiconductor superlattices.* Physical Review B, 1995. **52**(7): p. 5105-5123.
35. Ignatov, A.A. and Y.A. Romanov, *Nonlinear Electromagnetic Properties of Semiconductors with a Superlattice.* physica status solidi (b), 1976. **73**(1): p. 327-333.
36. Brandl, S., et al., *Microwave generation by a self-sustained current oscillation in an InGaAs/InAlAs superlattice.* Superlattices and Microstructures, 1999. **25**(1–2): p. 29-31.
37. Grahn, H.T., *Current self-oscillations and chaos in semiconductor superlattices.* Superlattices and Microstructures, 1999. **25**(1–2): p. 7-11.

38. Brandl, S., et al., *Millimeter wave generation by a self-sustained current oscillation in an InGaAs/InAlAs superlattice.* Applied Physics Letters, 1998. **73**(21): p. 3117-3119.
39. Terazzi, R., et al., *Bloch gain in quantum cascade lasers.* Nat Phys, 2007. **3**(5): p. 329-333.
40. Revin, D.G., et al., *Dispersive gain and loss in midinfrared quantum cascade laser.* Applied Physics Letters, 2008. **92**(8): p. 081110-3.
41. Gresch, T., et al., *Bloch gain in quantum cascade lasers at high temperature.* Applied Physics Letters, 2009. **94**(3): p. 031102-3.
42. F. Klappenberger, K.N.A., K.F. Renk, R. Scheuerer, E. Schomburg, S.J. Allen, G.R. Ramian, and A.K. J.S.S. Scott, V. Ustinov, and A. Zhukov, *Ultrafast creation and annihilation of space-charge domains in a semiconductor superlattice observed by use of Terahertz fields.* Eur. Phys. J. B, 2004. **39**: p. 6.
43. Demarina, N.V., A. Lisauskas, and H.G. Roskos, *Electron ensemble coherence and terahertz radiation amplification in a cascade superlattice structure.* Microelectronics Journal, 2008. **39**(3–4): p. 624-627.
44. Adachi.S, *GaAs and Related Materials*. 1994, Singapore: World Scientific.
45. Sirtori, C., et al., *GaAs-AlGaAs quantum cascade lasers: physics, technology, and prospects.* Quantum Electronics, IEEE Journal of, 2002. **38**(6): p. 547-558.
46. R. Kohler, A.T., Fabio Beltram, Harvey E. Beere, Edmund H. Linfield, A. Giles Davies, David A. Ritchie, Rita C. Iotti, Fausto Rossi, *Terahertz semiconductor-heterostructure laser.* nature, 2002. **417**: p. 156-159.
47. Rochat, M., et al., *Low-threshold terahertz quantum-cascade lasers.* Applied Physics Letters, 2002. **81**(8): p. 1381-1383.
48. Williams, B.S., et al., *3.4-THz quantum cascade laser based on longitudinal-optical-phonon scattering for depopulation.* Applied Physics Letters, 2003. **82**(7): p. 1015-1017.
49. Scalari, G., et al., *Far-infrared 87 um bound-to-continuum quantum-cascade lasers operating up to 90 K.* Applied Physics Letters, 2003. **82**(19): p. 3165-3167.
50. Faist, J., *Quantum cascade laser.* Science, 1994. **264**: p. 553-556.
51. B.Xu, *Development of Intersubband Terahertz Lasers Using Multiple Quantum Well Structure*, in *Departement of Electrical Engineering and Computer Science*. 1998, Massachusetts Institute of Technology.
52. Xu, B., Q. Hu, and M.R. Melloch, *Electrically pumped tunable terahertz emitter based on intersubband transition.* Applied Physics Letters, 1997. **71**(4): p. 440-442.
53. Helm, M., et al., *Intersubband emission from semiconductor superlattices excited by sequential resonant tunneling.* Physical Review Letters, 1989. **63**(1): p. 74-77.
54. Tong, M., et al., *A comparative study of wet and dry selective etching processes for GaAs/AIGaAs/lnGaAs pseudomorphic MODFETs.* Journal of Electronic Materials, 1992. **21**(1): p. 9-15.
55. Yablonovitch, E., et al., *Extreme selectivity in the lift-off of epitaxial GaAs films.* Applied Physics Letters, 1987. **51**(26): p. 2222-2224.
56. Griffiths.P, H.J.A., *Fourier Transform Infrared Spectrometry*. 1986: Wiley-interscience.
57. Smith.B.C, *Fundamentals of Fourier Transform Infrared Spectroscopy*. 1995: CRC

press.

58. Lisauskas, A., et al., *Examining the terahertz signal from a photoexcited biased semiconductor superlattice for evidence of gain.* Applied Physics Letters, 2008. **93**(2): p. 021122-3.
59. Jukam, N., et al., *Gain Measurements of THz Quantum Cascade Lasers using THz Time-Domain Spectroscopy.* Selected Topics in Quantum Electronics, IEEE Journal of, 2008. **14**(2): p. 436-442.
60. Jukam, N., et al., *Terahertz amplifier based on gain switching in a quantum cascade laser.* Nat Photon, 2009. **3**(12): p. 715-719.
61. Brozak, G., et al., *Thermal saturation of band transport in a superlattice.* Physical Review Letters, 1990. **64**(26): p. 3163-3166.
62. Sibille, A., et al., *Limits of semiclassical transport in narrow miniband GaAs/AlAs superlattices.* Superlattices and Microstructures, 1993. **13**(2): p. 247.
63. Göksu, T., et al., *Barrier height temperature coefficient in ideal Ti/n-GaAs Schottky contacts.* Microelectronic Engineering, 2010. **87**(9): p. 1781-1784.
64. Smet.J.H, *Intrawell and interwell intersubband transitions in single and multiple quantum well heterostructures*, in *Department of Electronical Engineering and Computer Science*. 1994, Massachusetts Institute of Technology.
65. Firsov, D.A., et al., *Absorption and emission of terahertz radiation in doped GaAs/AlGaAs quantum wells.* Bulletin of the Russian Academy of Sciences: Physics, 2008. **72**(2): p. 246-248.
66. Dignam, M.M. and J.E. Sipe, *Exciton Stark ladder in GaAs/Ga_{1-x}Al_{x}As superlattices.* Physical Review Letters, 1990. **64**(15): p. 1797-1800.
67. Dignam, M.M. and J.E. Sipe, *Exciton states in type-I and type-II GaAs/Ga_{1-x}Al_{x}As superlattices.* Physical Review B, 1990. **41**(5): p. 2865-2878.
68. Whittaker, D.M., *Saddle-Points and Stark Ladders: High-Resolution Calculations of Exciton Spectra in Superlattices* Europhys. Lett., 1995. **31**: p. 55.
69. Holfeld, C.P., et al., *Fano Resonances in Semiconductor Superlattices.* Physical Review Letters, 1998. **81**(4): p. 874-877.
70. Yang, L., et al., *Intraband polarization and terahertz emission in biased semiconductor superlattices with full excitonic basis.* Physical Review B, 2004. **69**(16): p. 165310.
71. Zak, J., *Stark Ladder in Solids?* Physical Review Letters, 1968. **20**(26): p. 1477-1481.
72. Voisin, P., et al., *Observation of the Wannier-Stark Quantization in a Semiconductor Superlattice.* Physical Review Letters, 1988. **61**(14): p. 1639-1642.
73. Leisching, P., et al., *Bloch oscillations of excitonic wave packets in semiconductor superlattices.* Physical Review B, 1994. **50**(19): p. 14389-14404.
74. Victor, K., H.G. Roskos, and C. Waschke, *Efficiency of submillimeter-wave generation and amplification by coherent wave-packet oscillations in semiconductor structures.* J. Opt. Soc. Am. B, 1994. **11**(12): p. 2470-2479.
75. D.Mittleman, ed. *Sensing with Terahertz Radiation*. 2003, Springer.
76. Leitenstorfer, A., et al., *Detectors and sources for ultrabroadband electro-optic sampling: Experiment and theory.* Applied Physics Letters, 1999. **74**(11): p.

1516-1518.
77. New, G., *Introduction to Nonlinear Optics*. 2011: Cambridge University Press.
78. Wu, Q. and X.C. Zhang, *Free-space electro-optic sampling of terahertz beams.* Applied Physics Letters, 1995. **67**(24): p. 3523-3525.
79. Wu, Q. and X.C. Zhang, *Ultrafast electro-optic field sensors.* Applied Physics Letters, 1996. **68**(12): p. 1604-1606.
80. Wu, Q. and X.C. Zhang, *7 terahertz broadband GaP electro-optic sensor.* Applied Physics Letters, 1997. **70**(14): p. 1784-1786.
81. E.D.Palik, *Handbook of Optical Constants of Solids II*. 1991, Boston: Academic Press.
82. Dekorsy, T., et al., *Bloch oscillations at room temperature.* Physical Review B, 1995. **51**(23): p. 17275-17278.
83. Gunn, J.B., *Instabilities of Current in III-V Semiconductors.* IBM Journal of Research and Development, 1964. **8**(2): p. 141-159.
84. Pratt, R.G. and B.K. Ridley, *The capture of thermal electrons by gold centres in N-type germanium at 20°K.* Journal of Physics and Chemistry of Solids, 1965. **26**(1): p. 11-20.